

https://dspace.org/

Hard, wear resistant Fe-B-C composites produced using spark plasma sintering

Rokebrand, Patrick Pierce

2017

https://hdl.handle.net/10539/24240

Rokebrand, Patrick Pierce (2017) Hard, wear resistant Fe-B-C composites produced using spark plasma sintering, University of the Witwatersrand, <https://hdl.handle.net/10539/24240>

Downloaded from a DSpace repository. https://dspace.org/



Hard, Wear Resistant Fe-B-C Composites Produced Using Spark Plasma Sintering

PATRICK PIERCE ROKEBRAND

'A thesis submitted to the Faculty of Engineering and the Built Environment, University of the Witwatersrand, Johannesburg, in fulfillment of the requirements for the degree of Doctor of Philosophy.'

Johannesburg, August 2017

DECLARATION

I, Patrick Pierce Rokebrand, declare that this thesis is my own unaided work. It is being submitted for the Degree of Doctor of Philosophy to the University of the Witwatersrand, Johannesburg. It is has not been submitted before for any degree or examination to any other university.

……

Signature

……day of……. Year…….

Abstract

Fe-B-C composites were produced, from boron carbide and iron powders, using spark plasma sintering. This provided information on the effects of rapid sintering on densification, composition and the microstructure of the materials produced. The composition range included a selection high Fe contents (69.3, 78 and 80.9 vol. % Fe-B_4C) and high B_4C concentrations (1, 3, 5 vol. % Fe-B_4C). The properties of the materials were investigated to determine the potential for using relatively cheap Fe and B_4C powders to produce hard, wear resistant materials.

High Fe-B_4C composites were sintered at 900, 1000 and 1100°C at 60 MPa. Densification increased with increasing temperature and at 1100° each composition achieved ≥ 97 % densification. The materials reacted during sintering with the main phases observed being Fe_2B and $Fe_3(B,C)$ whilst additional phases formed were FeB, C and $Fe_{23}(B,C)_6$.Comparing the phases that were produced to Fe-B-C phase diagrams showed deviations from expected compositions, indicating the non-equilibrium nature of producing the composites using SPS. Although the composites were not at equilibrium, all the B_4C reacted and could not be maintained, even with fast heating and cooling rates.

The properties of the materials were dependent on both densification and the phases that were present after sintering. Materials containing higher amounts of the Fe_2B phase showed higher hardness and fracture toughness results, up to 13.7 GPa and 3.5 $MPa.m^{0.5}$ respectively for the 69.3 vol. % Fe-B_4C. The materials were sensitive to grain and pore growth which negatively affected properties at 1100°C. The transverse rupture strength of 388.3 MPa for 80.9 vol. % Fe-B_4C composite was the greatest, and showed evidence of both intergranular and transgranular fracture. The strength was affected by a fine dispersion of porosity at the grain boundaries, throughout the material, and free carbon in the structure was detrimental to the strength of the 69.3 % Fe-B_4C. The wear rates were lower using Si_3N_4 wear balls compared to stainless steel balls, where 69.3 vol. % Fe-B_4C showed the best wear rates, 8.9×10^{-6} mm^3/Nm (stainless steel ball) and 1.77×10^{-6} mm^3/Nm (Si_3N_4 ball), due to the higher Fe_2B composition and free carbon acting as a lubricant during sliding.

1, 3 and 5 vol. % Fe-B_4C composites were sintered to densities above 97 % of theoretical at 2000°C and 30 MPa. The formation of a transient FeB liquid phase assisted densification. 1 % Fe-B_4C attained hardness and fracture toughness up to 33.1 GPa and 5.3 MPa.$m^{0.5}$ with a strength of 370.5 MPa. Thermal mismatch between the FeB phase and B_4C caused high residual stresses at the interface which led to cracking and pull-out of the FeB phase. Residual carbon at the grain boundary interface exacerbated the pull-out effect. Increasing Fe and the subsequent FeB phase had an embrittling effect. The materials suffered severe wear of up to 36.92×10^{-6} mm^3/Nm as a result of the pull-out with the remaining porosity acting as a stress raiser.

20 vol. % of the Fe in each system was substituted with Ti to reduce the presence of residual carbon. Although in some case the properties of the respective compositions improved, residual carbon was still present in the composites.

I would like to dedicate this thesis to my wife.

Thank you for always being a shining light.

I love you.

Acknowledgements

I would like to acknowledge and thank the following people and organizations for their valuable contribution to this project and which facilitated the completion of this work.

- Prof. I. Sigalas for his supervision, advice and guidance.
- Dr. Mathias Herrmann for his advice, guidance, time and input which was greatly appreciated.
- DST-NRF Centre of Excellence in strong materials for their financial assistance.
- University of the Witwatersrand for the use of their facilities.
- My friends and family for their love, support and patience.

Contents

DECLARATION i

Abstract ii

Acknowledgements v

List of Figures x

List of Tables xv

List of Abbreviations xvii

1. Introduction and Motivation 1

2. Literature Survey 3

2.1. Ceramics 3

2.2. Ceramic Processing 6

2.2.1. Powder 6

2.2.2. Sintering 7

2.3. Materials 15

2.3.1. Boron Carbide 15

2.3.2. Fe-B-C Composites 21

2.4. Mechanical Properties 25

2.4.1. Hardness 25

2.4.2. Fracture Toughness 27

2.4.3. Transverse Rupture Strength 30

2.4.4. Wear Resistance 31

2.5. Scope ..... **Error! Bookmark not defined.**

3. Experimental Procedure 35

3.1. Powder Processing 35

3.1.1. Particle Size Analysis 35

3.1.2. X-Ray Diffraction on Powders and Composites 36

3.1.3. Scanning Electron Microscopy on Powders and Composites 36

3.1.4. Washing of B_4C 37

3.1.5. Mixing of powders 37

3.1.6. Drying and Sieving 39

3.1.7. Sintering 39

3.2. Characterisation 40

3.2.1. Density 40

3.2.2. Cutting 41

3.2.3. Grinding and Polishing 41

3.2.4. Hardness and Fracture Toughness 43

3.2.5. Transverse Rupture Strength 44

3.2.6. Sliding Wear 46

4. Results 48

4.1. Powder Processing 48

4.1.1. Particle Size Analysis and Powder Morphology 48

4.1.2. X-Ray Diffraction 50

4.1.3. Composition changes during mixing 50

4.2. Sintering and Characterisation of Iron Dominant Composites 52

4.2.1. Density, Hardness and Fracture Toughness 52

4.2.2. Microstructure and Phase analysis 53

4.3. Sintering and Characterisation of B_4C Dominant Composites 64

4.3.1. Density, Hardness and Fracture Toughness 64

4.3.2. Microstructure and Phase analysis 66

4.4. Transverse Rupture Strength 73

4.4.1. Analysis of Fracture 74

4.5. Wear 77

4.5.1. Wear Resistance of Balls and Composites 77

4.5.1. Analysis of Wear Scars 80

5. Discussion 94

5.1. Powder Processing 94

5.2. Sintering behavior and properties of sintered composites 95

5.2.1. Theoretical density and composition analysis 101

5.2.2. Temperature and composition effects on densification 113

5.2.3. Comparison of hardness and fracture toughness results 116

5.3. Transverse Rupture Strength 125

5.3.1. Weibull modulus and Characteristic Strength 125

5.3.2. Relating strength to fracture toughness 128

5.4. Wear 130

5.4.1. Friction co-efficient and wear track analysis 130

5.4.2. Effect of mechanical properties on wear 134

6. Conclusions and future work 136

7. References 141

List of Figures

Figure 1: Comparison of the processing of advanced and traditional ceramics. (Adapted from Carter, pp.6)[1,14] 5

Figure 2: Representation of sintering process with refernce to changes in interfacial energy.[21] .. 8

Figure 3: Schematic of sintering mechanisms between two particles.[13] 9

Figure 4: Schematic of a typical SPS furnace.[33] 14

Figure 5: B – C Phase diagram showing B_4C composition range according to Schwetz et al.[46] 16

Figure 6: Crystal structure of B_4C as shown by Norimatsu et al.[45] 16

Figure 7: Effect of grain size on the flexural strength and fracture toughness of B_4C-TiC and B_4C doped with amorphous carbon as reported by Sigl et al.[58] 20

Figure 8: Optical micrograph of Fe+3 wt. % B_4C powder mixture sintered at 900°C for 10 (a) and 120 (b) min. From Bagliuk et al. [9] 22

Figure 10: Optical image of B_4C–FeB composite sintered at 2000°C as shown by Frage et al. [69] 23

Figure 11: Isothermal sections of the Fe-B-C phase diagram at (a) 1473K, (b) 1723K and (c) 1923K as calculated by Aizenshtein et al.[91] 24

Figure 12: Hall–Petch plot of hardness of nanocrystalline ZrN coatings against the inverse square-root of grain size.[103] 27

Figure 13: Schematic showing side and top views of a) median and b) Palmqvist cracks produced using Vickers indentations and the effect of polishing in the determination of the type of crack. (adapted from Barsoum) [15] 29

Figure 14: Schematic showing geometry of Vicker's hardness indenter. (Callister, pp 224)[18] .. 43

Figure 15: Particle size distribution for the B_4C, Fe and Ti powders. 48

Figure 16: SE-SEM micrographs of as received A) B_4C powder, B) Fe powder and C) Ti powder..... 49

Figure 17: XRD analysis of the B_4C, Fe and Ti powders. 50

Figure 18: XRD analysis comparing the 80.9 vol. % Fe-B_4C composites sintered at 900, 1000 and 1100°C. 54

Figure 19: BS-SEM micrographs comparing microstructures of the 80.9 vol. % Fe-B_4C composites sintered at 900, 1000 and 1100°C. 55

Figure 20: EDX analysis of the 80.9 vol. % Fe-B_4C composites sintered at 1000°C. 56

Figure 21: XRD analysis comparing the 78 vol. % Fe-B_4C composites sintered at 900, 1000 and 1100°C. 57

Figure 22: BS-SEM micrographs showing microstructures of the 78 vol. % Fe-B_4C composites sintered at 1000 and 1100°C. 58

Figure 23: XRD analysis comparing the 69.3 vol. % Fe-B_4C composites sintered at 900, 1000 and 1100°C. 59

Figure 24: BS-SEM micrographs of the 69.3 vol. % Fe-B_4C composites sintered at 900, 1000 and 1100°C. 60

Figure 25: EDX analysis with focus on dark grey phase dispersed through carbon rich areas and bright WC phase in 69.3 vol. % Fe-B_4C composite sintered at 1000°C and 60 MPa. 60

Figure 26: XRD analysis comparing the 69.3 vol. %, 78 vol. % and 80.9 vol. % (0.8 Fe+0.2Ti)-B_4C composites sintered at 1000°C and 60 MPa. 61

Figure 27: BS-SEM micrographs showing the microstructures of a) 69.3, b) 78 and c) 80.9 vol. % (0.8Fe+0.2Ti)-B_4C composites sintered at 1000°C and 60MPa..... 63

Figure 28: EDX mapping of Ti rich phase in the microstructure of the 69.3 vol. % (0.8Fe+0.2Ti)-B_4C composite sintered at 1100°C and 60MPa. 64

Figure 29: XRD analysis comparing the 5 vol% Fe-B_4C, 3 vol% Fe-B_4C and 1 vol% Fe-B_4C composites sintered at 2000°C and 30MPa. 67

Figure 30: BS-SEM micrographs showing the microstructures of the a) 1 vol% Fe-B_4C, b) 3 vol% Fe-B_4C and c) 5 vol% Fe-B_4C composites sintered at 2000°C and 30MPa..... 68

Figure 31: BS-SEM micrograph showing inclusions within FeB phase in 1 vol% Fe-B_4C sintered at 2000°C and 30MPa, identified using EDX analysis. 1 vol% Fe-B_4C 68

Figure 32: XRD analysis of the 1, 3 and 5 vol% (0.8Fe+0.2Ti)-B_4C composites sintered at 2000°C and 30MPa. 69

Figure 33: BS-SEM micrographs depicting the microstructures of the A) 1 vol%, B) 3 and C) 5 vol% (0.8Fe+0.2Ti)-B4C composites sintered at 2000°C and 30MPa. 70

Figure 34: XRD analysis of the 5 vol% Ti-B_4C composites prepared using WC milling balls and Fe milling balls produced at 2000°C and 30MPa. 72

Figure 35: BS-SEM micrographs comparing the 5 vol% Ti-B_4C composites prepared using A) WC milling balls and B) Fe milling balls and produced at 2000°C and 30MPa. 72

Figure 36: Typical mode of fracture observed showing initiation at the center of the samples. .. 74

Figure 37: SE-SEM micrographs showing the microstructure of the A) 69.3 vol%, B) 78 vol% and C) 80.9 vol% Fe-B_4C B3B fractured composites sintered at 1100°C and 60 MPa. 76

Figure 38: SE-SEM micrographs of the microstructure observed for A) 1% Fe-B_4C and B) 1% (0.8Fe+0.2Ti)-B_4C TRS fractured composites sintered at 2000°C and 30 MPa (Transgranular fracture marked O and intergranular marked X)..... 77

Figure 39: Wear scars observed on stainless steel (SS) and silicon nitride (SN) wear balls under an optical microscope. 81

Figure 40: SE-SEM micrographs of the wear scar and its appearance therein for A) 69.3% Fe-B_4C, B) 78% Fe- B_4C, C) 80.9% Fe-B_4C and D) 69.3% (0.8Fe+0.2Ti)-B_4C sintered at 1100°C and 60 MPa with ball direction indicated. 83

Figure 41: EDX analysis showing wear debris on the A) 69.3% Fe-B_4C, B) 78% Fe-B_4C, C) 80.9% Fe-B_4C and D) 69.3% (0.8Fe+0.2Ti)-B_4C to contain an oxide phase. 84

Figure 42: SEM micrographs of the wear scar of the 80.9 vol% Fe-B_4C showing cracks and debris in a) secondary electron mode with ball direction indicated and b) backscatter mode with crack type indicated. (white arrows – transgaranular, black arrows intergranular fracture) 86

Figure 43: SE-SEM micrographs of the wear scar and its appearance therein for A) 1% Fe-B_4C, B) 1% (0.8Fe+0.2Ti)-B_4C and C) 5% Fe-B_4C when using stainless steel balls with ball direction indicated. 88

Figure 44: EDX analysis of the wear track for A) 1% Fe-B_4C, B) 1% (0.8Fe+0.2Ti)-B_4C and C) 5% Fe-B_4C. 89

Figure 45: SE-SEM micrographs of the wear scar for A) 1% Fe-B_4C, B) 78% Fe-B_4C and C) 80.9% Fe-B_4C when using silicon nitride balls with ball direction indicated. 91

Figure 46: EDX analysis on wear debris for A) 1% Fe-B_4C, B) 78% Fe-B_4C and C) 80.9% Fe-B_4C when using Si_3N_4 balls. 92

Figure 47: SEM micrographs (SE-mode) (A) and (BS-mode) (B) of the wear track microstructure in the 80.9% Fe-B_4C composite tested with Si_3N_4 balls with the ball sliding direction indicated. 93

Figure 48: Densification curves for 69.3, 78 and 80.9 vol. % Fe-B_4C composites sintered at a) 900°C, b) 1000°C and c) 1100°C. 97

Figure 49: Densification curve for 78 vol. % Fe-B_4C sintered at 1100°C and 60 MPa, with densification rate and applied current during sintering. 98

Figure 50: Comparison of densification points of interest (T_1, T_2 and T_3) when sintering at a) 900°C, b) 1000°C and c) 1100°C. 99

Figure 51: a) Densification curves for 1, 3 and 5 vol. % Fe-B_4C composites sintered at 2000°C and 30 MPa, with b) densification rate of 5 vol. % Fe-B_4C. 100

Figure 52: Estimation of reaction free energy from Fe_2B-$Fe_3(B,C)$ compositions..... 108

Figure 53: Free energy of formation of Fe_xB_y and $Fe_a(B,C)_b$ phases at 900, 1000 and 1100°C. 109

Figure 54: Reaction free energy at 900, 1000 and 1100°C for reactions 3, 4 and 5. 110

Figure 55: a) Effect of sintering temperature on densification in 69.3, 78 and 80.9% Fe-B_4C composites sintered at 60 MPa. 113

Figure 56: Effect of increasing Fe content from 1 to 5 vol. % in the starting powder on densification and open porosity when sintering at 1910°C and 2000°C. 115

Figure 57: Relationship between temperature and hardness for high Fe additions to B_4C produced using SPS. 117

Figure 58: Sintering temperature effects on fracture toughness in composites with high Fe additions to B_4C. 119

Figure 59: BS-SEM analysis of Vickers (5 kg) indentation cracks showing evidence of a) intergranular cracks in 78 vol. % Fe-B_4C sintered at 1000°C and b) transgranular crack propagation in 80.9 vol. % Fe-B_4C sintered at 1100°C. 120

Figure 60: Comparison of hardness at 1910°C and 2000°C for low Fe containing composites, with relative density observed. 122

Figure 61: Fracture toughness with 1 – 5 vol. % Fe additions to B_4C sintered at 1910°C and 2000°C. 124

Figure 62: Probability of failure with Weibull modulus for additions ≥ 69.3 % to B_4C with a) as measured strength data and b) data considering effective volume of the test piece as per Table 10..... 126

Figure 63: Determination of Weibull modulus and characteristic strength from a) B3B test data for 1 % Fe and FeTi additions to B_4C and b) accounting for the effective volume of the composites as shown in Table 10..... 127

Figure 64: Comparison of fracture toughness with characteristic strength of select Fe-B-C composites..... 128

Figure 65: Relationship between sample and ball wear rate and friction coefficient for a) ≥ 69.3 % additions to B_4C with stainless steel balls, b) ≥ 69.3 % additions to B_4C with Si_3N_4 balls and c) additions ≤ 5 vol. %. 131

Figure 66: Comparison of average cross-sectional area of wear tracks for 1% additions to B_4C. 133

Figure 67: Relationship between sample wear rate and a) hardness and b) fracture toughness of sliding wear tested composites..... 135

List of Tables

Table 1: Summary of sintering parameters, densification and properties of boron carbide produced using FAST/SPS from various sources.[53-57,68,69] 19

Table 2: Comparison of indentation hardness testing techniques.[18,20] 25

Table 3: Suppliers of all powders used in this project. 35

Table 4: Compositions and relevant mixing and sintering requirements 38

Table 5: Grinding/Polishing procedure..... 42

Table 6: Particle size of the starting powders. 49

Table 7: Mass losses form the milling balls and the respective adjustments to composition for mixed powders. 51

Table 8: Density, hardness and fracture toughness for low B_4C containing composites. 53

Table 9: Density, hardness and fracture toughness for composites with a high B_4C content..... 65

Table 10: B3B strength and Weibull modulus (m) calculated using the ball on three ball test.... 73

Table 11: Sliding wear resistance (load = 10 N, speed = 0.21 m/s, sliding distance = 300 m, environment – air, no lubricant, humidity 55 to 65%)..... 78

Table 12: Effect of milling ball contamination on the powder composition for sintering. 95

Table 13: Comparison of theoretical density of pre-mixed and mixed powder components to the sintered composites with high vol. % additions to B_4C. 103

Table 14: Theoretical density of pre-mixed and mixed powder components for 1-5 vol. % additions to B_4C. 104

Table 15: Phases present in sintered Fe-B_4C composites (X = observed, E = expected from phase diagrams[81,90,91,151]). 105

Table 16: Microstructure analysis of the amounts of Fe_2B and $Fe_3(B,C)$ in the matrix and relative to each other. 107

Table 17: High Fe-B_4C mixed powder molar composition. 108

Table 18: Comparison of low Fe-B_4C phase compositions and corresponding theoretical densites calculated using reaction 6 and analysis of the cross-section. 111

List of Abbreviations

Al – aluminium

Al_2O_3 – alumina

B – boron

B_XC_Y – boron carbide

BCl_3 – boron chloride

B_XO_Y – boron oxide

C – carbon

CH_4 – methane

CO_2 – carbon dioxide

Cr – chromium

Cu – copper

Fe – iron

Fe_YB_X – iron boride

H_2 – hydrogen

h-BN – hexagonal boron nitride

HCl – hydrogen chloride

Mg – magnesium

Mn – manganese

Si – silicon

SiC – silicon carbide

Ti – titanium

Ti_XB_Y – titanium boride

TiC – titanium carbide

WC – tungsten carbide

B3B – ball on three balls TRS test

CVD – chemical vapor deposition

EDX – Energy-dispersive X-ray spectroscopy

FAST – field assisted sintering technology

HIP – hot isostatic pressing

PECS – pulsed electric current sintering

PEG – polyethylene glycol

PSA – particle size analysis

SEM – scanning electron microscopy

SENB – single edge notched bend

SEVNB – single edge V-nothched bend

SPS – spark plasma sintering

TRS – transverse rupture strength

XRD – X-ray diffraction

1. Introduction and Motivation

Since the mid twentieth century, the development and improvement of advanced ceramics has seen significant increase in demand for the use of ceramic components in industrial applications.[1] Ceramics are used regularly in applications where wear resistance is paramount. The density of ceramics is generally lower than that of steel and, as a result, their use in armour has shown significant improvements in light armour applications.

Boron carbide is a ceramic of particular interest; its combination of properties has seen it used in a number of applications. These mostly involve wear based applications as a result of its abrasive resistance, but it is used in many other applications including light armour and as a neutron absorber in nuclear reactors.[2-4] However, B_4C is inherently very difficult to sinter to full density, requiring high temperature typically above 2000°C. As a result, a number of sintering aids have been used to promote densification at lower temperatures.[2,5,6]

Fe-B-C composites have been produced over a range of compositions. Small amounts of boron and carbon are often added to steel alloys where the amounts of each material added dictate the properties of the alloy.[7.8] The popularity of the Fe-B-C system was a result of the ease of manipulating properties and microstructure by varying B and C compositions. The formation of hard iron boride and iron carbide phases increases the hardness and wear resistance of the materials. Sintered Fe-B-C composites have properties similar to 100Cr6 steel with a high wear resistance as a result of the heterophase structure.[9,10]

The nature of spark plasma sintering (SPS) allows for rapid sintering of composites which has the potential to improve properties with a major benefit being the restriction of grain growth at higher temperatures. The high heating rates of the materials with the addition of pressure potentially enables the full densification of materials using shorter sintering times and lower temperatures.[11,12,13]

This project aimed to investigate the preparation of a range of Fe-B-C compositions using boron carbide and iron powders sintered using the spark plasma sintering (SPS) technique, in an attempt to improve on the properties of Fe-B-C compounds. This provided information on the effects of rapid sintering on densification, composition and the microstructure of the materials produced. Ti additions were made to the system with the aim of eliminating/reducing residual carbon in the sintered composites and potentially improving the properties.

The hardness, fracture toughness, transverse rupture strength and abrasive wear resistance, in relation to the composition and respective structure, of the sintered samples were reported and analysed. The properties of the materials produced were compared to those of Fe-B-C and B_4C materials typically used in wear, cutting tool and armour applications in order to assess their potential for use.

Chapter 2 gives a detailed literature review of ceramics with emphasis placed on B_4C and Fe-B-C compounds and their relative processing and characterization techniques.

Chapter 3 describes the materials, equipment and the corresponding experimental procedures that were used in this work.

Chapter 4 gives the results of the material characterization, mechanical properties and wear of selected composites.

Chapter 5 provides a detailed discussion of the results presented.

Chapter 6 contains the conclusions of this work and the recommendations for future work.

2. Literature Survey

This section of the work aimed at providing a background to ceramic materials, with a focus on the processing and characterization techniques commonly applied. The techniques discussed here have been limited to those most relevant to the objectives of this project and those commonly applied to the materials being used and produced. Following this, the materials relevant to this body of work (B_4C, Fe and Fe-B-C) are discussed in greater detail.

2.1. Ceramics

Ceramics are most commonly divided into two groups; traditional and advanced ceramics. Traditional ceramics are comprised mostly of silicates, and the majority of their uses were in porcelains and pottery.[14] As technology progresses, demands on the performance criteria of parts increase. This, in turn, has prompted the development and use of materials better suited to meet the needs of these applications. Advanced ceramics are often referred to as technical, engineering or fine ceramics. They are used for a number of structural, electrical, optical, electronic and magnetic applications.[14-16]

The properties most commonly associated with ceramics are high hardness, good thermal stability and they are prone to brittle fracture.[14-17] These properties are a result of the materials containing strong covalent bonds which also results in the high melting point associated with ceramics.[16] The brittle nature of ceramics means they are better suited to applications exploiting their compressive strength as opposed to tensile strength and the differences in ductility is the biggest difference between them and metals.

Another group of materials, referred to as cermets, combines the ductility and toughness of a metallic matrix with the strength and hardness of ceramic particles.[16,18] The most common cermets are cemented carbides using tungsten carbide or titanium carbide particles with a cobalt matrix.[16,18] In order to benefit from the favorable properties of the ceramic and metal components, it is important that metal chosen is able to wet the ceramic during sintering. This ensures that there is a strong bond between the ceramic and metal matrix.[16]

Due to the nature of ceramics, their processing differs from other materials as they require high temperature furnaces, are not suited to common metallurgical practices and their hardness and susceptibility to brittle failure make them difficult to machine.[14,19] As a result they are typically produced in shapes close to those required, also any machining is expensive as hard diamond and carbide cutting tools are required[17-19]. The comparison of advanced and traditional ceramics in Figure 1 highlights the differences in the processing requirements between traditional and advanced ceramics.

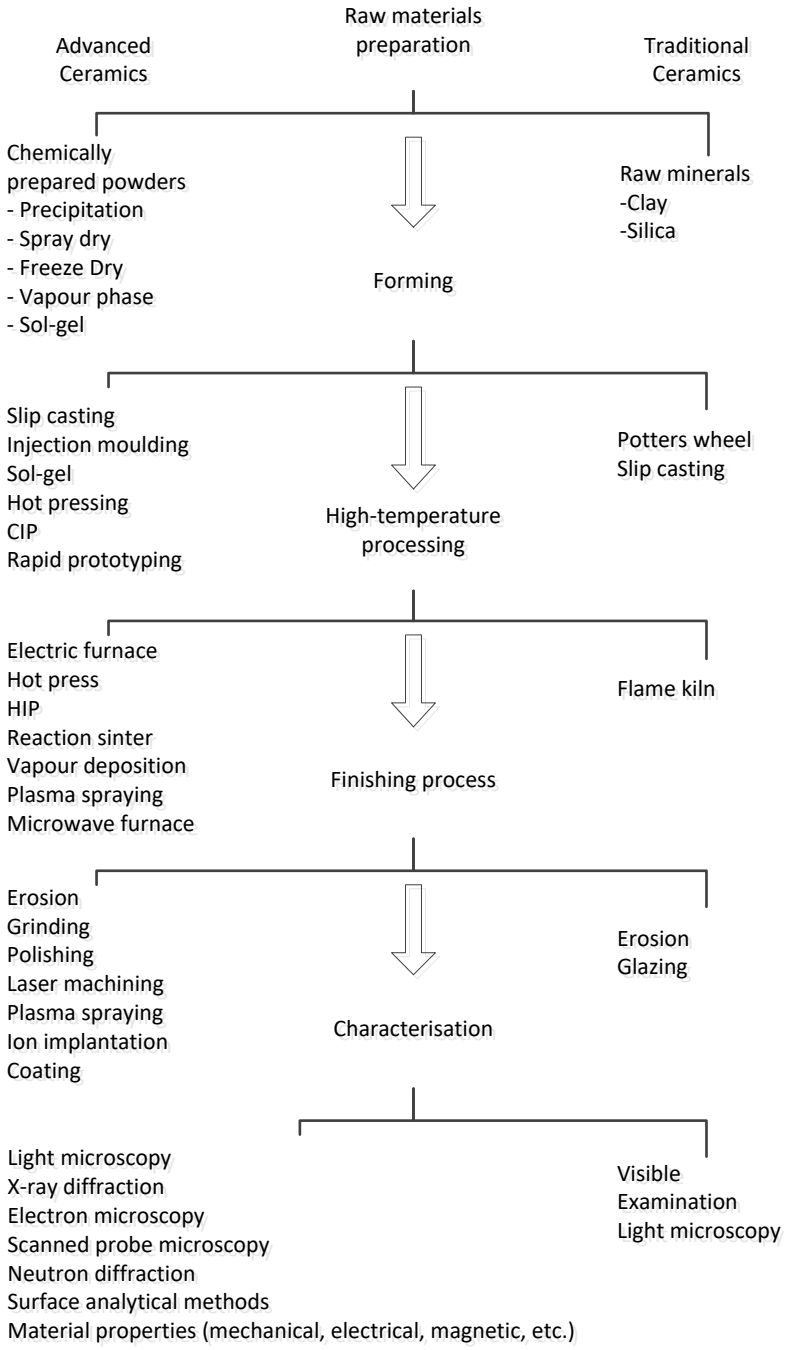


Figure 1: Comparison of the processing of advanced and traditional ceramics. (Adapted from Carter, pp.6)[1,14]

2.2. Ceramic Processing

The processing of advanced ceramics is of particular importance as, from the beginning, each step/procedure that is used to produce a final product influences its final characteristics and properties.[19]

2.2.1. Powder

The first stage in the processing of ceramics begins with the powder.[14] A number of the powder characteristics affect the mechanical properties of the final ceramic product. These include the size and morphology of the particles and also the purity of the powder. It is known that materials with a finer grain size show improved properties from those with coarser grains.[14,15,19] Due to the effects of grain growth during the sintering process, the most common way to obtain a fine microstructure is to use a powder with an even finer particle size.[14,15,19] There has been a significant drive towards the use of nanopowder however, due to increased difficulties in the production and handling of these powders, their cost is significantly higher than coarser ones. Various techniques have been used in the powder preparation process including comminution and chemical processes such as; spray drying, freeze drying and precipitation.[14,19] As expressed in Figure 1, powders for advanced ceramics are typically prepared through chemical processes as finer powders can be more feasibly achieved with less chance of contamination.

Impurities in the powder have the potential to be detrimental to the properties of the final product. Although some may be harmless or even beneficial, unless this is known/expected of a given impurity, they are avoided as much as possible. They have the potential to act as a flaw or stress raiser, introduce porosity and even cause failure during the sintering process if there is an evolution of gases within a closed die set.[14,19]

2.2.2. Sintering

2.2.2.1. Sintering Process

Ceramic powders are typically densified using a heat treatment process referred to as sintering or firing where, powders are initially pressed to form a green body with the required shape which is sintered to produce a dense solid.[13,14,15,19,20] During sintering, powder particles coalesce resulting in shrinkage and a reduction in porosity, which correlates to an improvement in the mechanical integrity of the piece.[13-15,18-21]

Sintering is a diffusion driven process which serves to minimise the free energy of the system. Atoms diffuse through the points of contact, bonding particles together and promoting pore shrinkage in order to minimise the surface energy of the particles.[20] This change has been expressed using the interfacial energy (γ) and corresponding interface area (A) between the particles as per equation 1; where (γA) is the total interfacial energy between the particles.[21]

$$\Delta(\gamma A) = \Delta\gamma A + \gamma\Delta A \qquad \text{Equation 1}$$

The change in interfacial energy occurs as the solid/vapour interface (γ_{SV}) becomes a solid/solid interface (γ_{SS}) promoting the shrinkage of pores and therefore densification to take place as $\gamma_{SV} > \gamma_{SS}$.[3] The change in area is a result of coarsening of the particles/grains since finer particles have a significantly greater surface area and as a result, a higher interfacial energy.[3,4] Figure 2 shows both the individual and combined effect of these terms on sintering. Coarsening and densification take place at the same time however, it is important that coarsening be subdued whilst the majority of densification occurs in order to achieve near theoretical density.[4-6]

Three stages are commonly used to describe the solid state sintering process; there is concave neck formation between the particles as the atoms diffuse to the point on contact and the particles begin to bond together and is responsible for an initial linear shrinkage of roughly 5 %.[13,15,19] This is followed by an intermediate stage where the concave necks begin to broaden forming a structure of contiguous particles with pore channels as densification approaches 90 %.[13,19] In the final stage, the pore channels begin to close as porosity is removed and discreet round pores are

formed at grain boundary corners.[14,18,19,21] During this stage grain growth may be significant and if it is severe the removal of the remaining porosity is very difficult.[13]

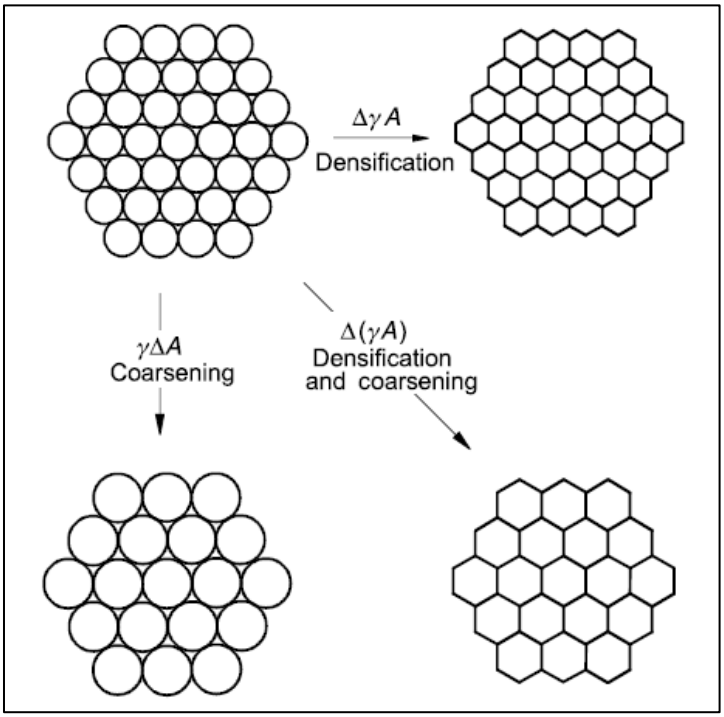


Figure 2: Representation of sintering process with refernce to changes in interfacial energy.[21]

The minimisation of the surface energy is considered the main driving force for sintering. There are six transport mechanisms that allow for sintering to ocurr as shown in Figure 3.[13,14,19] These mechanisms are divided into non-densifying and densifying mechanisms based on there contribution to shrinkage. Mechanisms 1-3 shown in Figure 3 (surface diffusion, lattice diffusion from the surface and vapor transport) are considered non-densifying mechanisms which promote neck growth.[13,14,19] Mechanisms 4 and 5 (grain boundary diffusion and lattice diffusion from a grain boundary to a pore are the main densifying mechanisms in ceramics, promoting both neck growth and shrinkage.[13,14,19] Mechanism 6 (plastic flow) also promotes both neck growth and shrinkage however, it is more applicable to materials with a greater susceptibility to deformation, such as metals, rather than ceramics.[13,19]

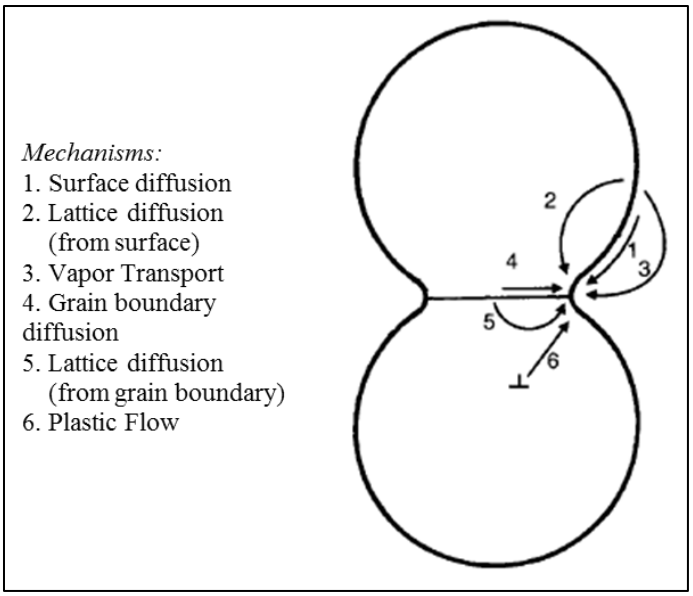


Figure 3: Schematic of sintering mechanisms between two particles.[13]

It is important to consider the effect of grain boundaries on the system as a reduction in grain boundary area is associated with a free energy reduction of the system.[15,19] This is the driving force for coarsening/grain growth during sintering.[21] When taking into account both the specific surface energy (γ_{SV}) and the specific grain boundary energy (γ_{GB}) with respect to the change in their relative free surface areas (ΔA) equation 2 is obtained.[19]

$$\Delta E = \gamma_{SV}\Delta A_{SV} + \gamma_{GB}\Delta A_{GB} \qquad \text{Equation 2}$$

In order to minimize the free energy, the system will tend toward an equilibrium point where $|\gamma_{SV}\Delta A_{SV}| = |\gamma_{GB}\Delta A_{GB}|$, however, if $|\gamma_{SV}\Delta A_{SV}| < |\gamma_{GB}\Delta A_{GB}|$ coarsening would be favoured over densification.[19] This emphasizes the importance of controlling the grain size during sintering, not only for the improved properties associated with a finer microstructure but also in ensuring successful densification during sintering.[14] Factors that reduce the effect of grain growth include the homogeneous dispersion of starting powder, fast heating profiles and the addition of secondary phases.[14,15,19,21] Structural non-uniformities in solids such as grain boundaries, dislocations or inclusions also influence accelerated densification and grain growth retardation[19,22,23]

Sintering is most commonly a solid-state process where there is no liquid phase and atomic diffusion is responsible for densification. In order for this to occur, the temperature used are typically 50-90 % of the melting point of the material being processed.[13] This is not always the case as the compositions being sintered are often tailored to produce different phases or to improve densification at lower temperatures.[13,14] As a result, liquid phase sintering and reaction sintering are two techniques which are also employed.

Liquid Phase Sintering

The presence of a liquid phase which is able to wet the solid phase during sintering, typically serves to improve densification, although they have also been used to accelerate grain growth and achieve certain grain boundary properties.[13] A small amount of an additive with a lower melting point than the bulk material is added forming a liquid phase during sintering.[13,14,15] This promotes an accelerated rearrangement of the solid particles as capillary forces assist the liquid phase transport through the bulk, removing voids.[15] Depending on the liquid phase additive chosen with the matrix, it is possible for some of the solid bulk to dissolve resulting in the reprecipitation of solid solution phases.[14,15] This is typically followed by some solid-state sintering to remove the last of the porosity.[14] Although the addition of a liquid phase aids densification, it is often at the expense of high temperature properties such as creep and fatigue resistance.[13]

Reaction Sintering

Reaction sintering refers to a process through which new phases are formed during the heat treatment stage.[13,19] Reactions occur and typically producing a greater change in free energy of the system than sintering. As a result it is possible that the occurrence of reactions may hinder the densification as free energy is minimized, it is also difficult to control the final microstructure.[13,19] Although many ceramic systems have some reactions occurring/promoted such as additives for removal of surface layer oxides, they are not termed reaction sintering processes.[13] This is reserved for systems where the major phase(s) is synthesized as a result of the reaction of a minimum of two starting powders with different compositions.[13]

2.2.2.2. Sintering Variables

A number of factors contribute to the behavior of a material during sintering. As touched on previously, the powder itself is the starting point and its properties have a significant effect on the materials sinterability.[14,19] These properties include the particle size, distribution, shape and agglomeration.[15,21] Powder homogeneity is important particularly for compositions consisting of two or more powders. The parameters associated with sintering- the sintering temperature, heating and cooling rates and isothermal hold time all affect sintering as diffusion is thermally activated and based on attaining an equilibrium state which takes time.[15,21] Higher temperatures and longer times are responsible for increased and possibly excessive grain growth.[13,15,21] Due to the sensitivity of materials to different atmospheres, either through reactions or influences to properties such as diffusion rates, the sintering atmosphere also has the potential to influence the sintering kinetics.[15] The advantage of applying pressure during sintering is that samples can be sintered at a lower temperature, which decreases the rate at which grain growth occurs, allowing dense, finer grained composites to be produced.[19]

2.2.2.3. Sintering Techniques

A number of sintering techniques are used to densify ceramics. The techniques that have previously been used to sinter materials relevant to this project are discussed briefly. Emphasis is placed on spark plasma sintering as the method relevant to sintering studies performed in this work.

Conventional Sintering

Conventional/pressureless sintering involves the heat treatment of a green body without the application of pressure.[19] The technique has been used widely, however, very high sintering temperatures and long dwell times are often required with ceramic materials. As a result, while it is possible to sinter pure ceramics to full density, the potential for grain growth is greater compared to sintering techniques where lower temperatures may be implemented.[2,15,19] In order

to improve the sinterability of ceramics subjected to conventional sintering, additives are used, allowing for liquid phase sintering and improved densification at lower temperatures.[2,19,21]

Hot Pressing

The hot pressing technique allows for the sintering of samples whilst applying both temperature and a uniaxial pressure to a green compact and is regularly used to produce dense ceramic materials.[15] Operating conditions have seen temperatures in excess of 2000°C and pressures between 10 and 75 MPa being applied.[19] In order to produce dense materials, the process is limited to simple shapes (blocks, cylinders, flat plates, etc.) as complex shapes are restricted and require different sintering techniques.[14] Another disadvantage to this method is its cost and it is a batch operation as a result of the inert atmosphere required.[15]

Hot Isostatic Pressing

Like hot pressing, hot isostatic pressing (HIP) makes use of the simultaneous application of temperature and pressure with the difference being the manner in which pressure is applied.[15] The HIP process uses an isostatic gas pressure which is applied to the sample in all directions. Temperatures can be up to 2000°C and isostatic pressures of 30‑300 MPa are typically applied.[2,14] This process is beneficial as the pressures that can be applied are significantly greater than those used in hot pressing; the process also lends itself to the sintering of complex shapes as the pressure is applied over the entire sample.[13,14,19] The high temperatures and pressures that are achievable see the technique readily applied to a wide range of ceramics components.[14]

Microwave sintering

Microwave sintering has been successfully used as a method for producing dense ceramic bodies.[24-27] Significant developments have been made in the sintering of non-oxides such as carbides, borides and nitrides.[24,25] Sintering is most commonly performed using 915 MHz and 2.45 GHz although higher frequencies (up to 60 GHz) have been applied.[24,25,27]

The main advantage of using microwaves in the sintering process is that heating occurs as a result of the interaction of the microwaves with the atoms of the material; allowing for rapid heating from within the material leading to shorter processing times.[25] In an effort to minimize the occurrence of temperature gradients, a two-step hybrid heating process is often applied.[24-29]

Laser sintering

The laser sintering process was applied as a manufacturing method in the 1980's; it was initially used in the development of prototypes and is now used for fast manufacturing of components in industry.[30,31] The main advantage associated with laser sintering is its ability to produce complex shapes in a single operation. The sintering process makes use of a high energy laser which heats the powder and sinters it in successive layers.[31] Ceramics require the use of high energy lasers as a result of their high melting points. The most common lasers used for sintering ceramics are continuous wave CO_2 and Nd:YAG fiber lasers.[30-32]

Spark Plasma Sintering

Spark plasma sintering (SPS) also makes use of the simultaneous application of temperature and pressure.[13,33] The process is of interest as a result of the high heating rates (600°C/min) that can be achieved, allowing for rapid densification of powder at relatively lower temperatures compared to conventional methods.[12,13] The rapid heating rates are attained through the application of a pulsed DC current which is passed through a powder compact in a die (typically graphite).[33] This allows for both the die and the sample to be heated during sintering again influencing the heating rates and also the temperature distribution through the sample. The applied pressure is generally in the range of 30-50 MPa however, higher pressures have been used.[13,34-36] The short processing time is the main reason this process is of interest; this provides the potential to produce a fully dense material with a grain size similar to that of the starting powders.[33] As a result, the SPS technique has gained popularity in the sintering of nano powders in an attempt to maintain a nano grain structure.[11,13] It has been applied to a wide range of materials including metals, alloys, functional graded materials and ceramics.[37] The high heating rates and the ability to reach temperatures in excess of 2000°C makes it particularly useful for ceramic sintering.[13] A schematic of the SPS furnace is depicted in Figure 4.

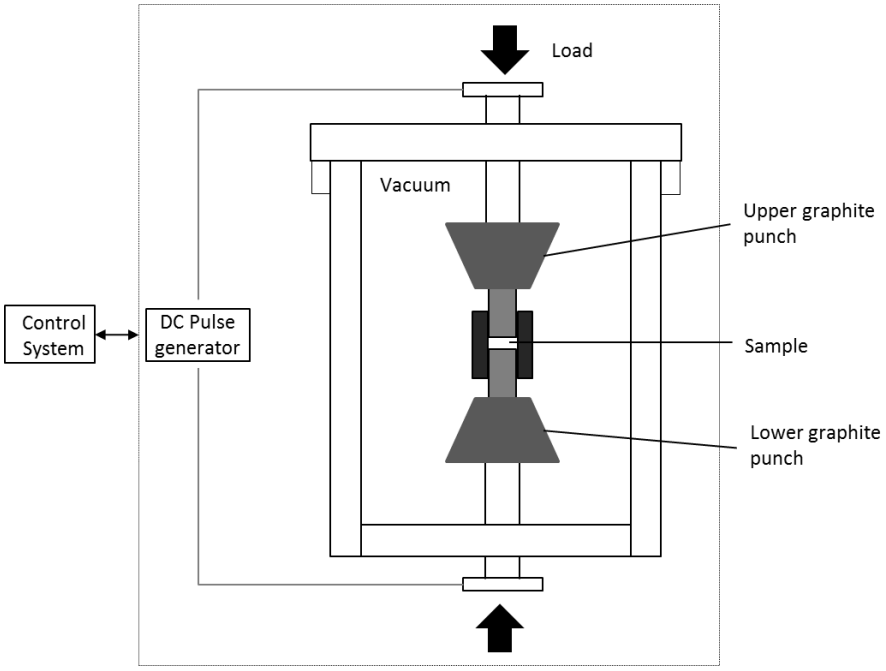


Figure 4: Schematic of a typical SPS furnace.[33]

The technique is popularly referred to as spark plasma sintering as it was originally thought the pulsed current allowed for the generation of sparks and also plasma discharges between particles, providing enhanced diffusion.[11,38] This however, has not yet been proved and the process is often referred to by other names including field assisted sintering technology (FAST) and pulsed electric current sintering (PECS).[39] Groza et al. observed the formation of grain boundaries without oxidation between particles and suggested that the pulsed current had a cleaning effect on the particle surface.[40] Tiwari et al. suggested that the cleaning of the powder surface is a result of the Joule heating effect at the particle surfaces (localised high temperature) resulting in temperatures reaching boiling point allowing for vaporization.[41] The ability of the current to flow through the sample during heating is dependent on its electrical conductivity. Although this suggests that a conducting material would heat more efficiently, Zhang et al. produced a finite element model that suggests the Joule heat generated at the punch ends is responsible for the majority of the heating regardless of the sample electrical conductivity.[42] However, Räthel et al. observed that an electrically non-conductive sample results in a higher temperature on the

outside of the die when compared to a conducting one.[43] The design of the die (shape, size, etc.) also affects the temperature distribution within the die and sample.[43]

The temperature is monitored using an optical pyrometer. Räthel et al. showed the position at which the pyrometer measures the temperature on the die has an effect on the temperatures that are reported.[43] The position of the pyrometer varies between different furnace manufacturers; therefore, care must be taken to observe both the type of furnace being used as well as the sintering parameters when observing SPS/FAST data.

2.3. Materials

2.3.1. Boron Carbide

Boron carbide (B_4C) is an advanced technical ceramic with unique properties. It has a high hardness, good wear and chemical resistance, low density ($2.52 g/cm^3$) and high elastic modulus.[2,5,44] However; it is brittle, has low impact strength, low fracture toughness, is prone to thermal shock and is expensive to produce where high purity B_4C is required. As a result of this, boron carbide is not widely used in engineering.

Although the suggested stoichiometric composition of boron carbide is B_4C, in reality it has a wide phase homogeneity ranging from B_4C to $B_{10.4}C$.[5] Although referred to as B_4C, it does not reach this composition as shown in the phase diagram in Figure 5.[5] It has a rhombohedral crystal structure, as shown in Figure 6, belonging to the $R\bar{3}m$ space group.[45] The unit cell contains 15 atoms corresponding to $B_{12}C_3$.[2,45]

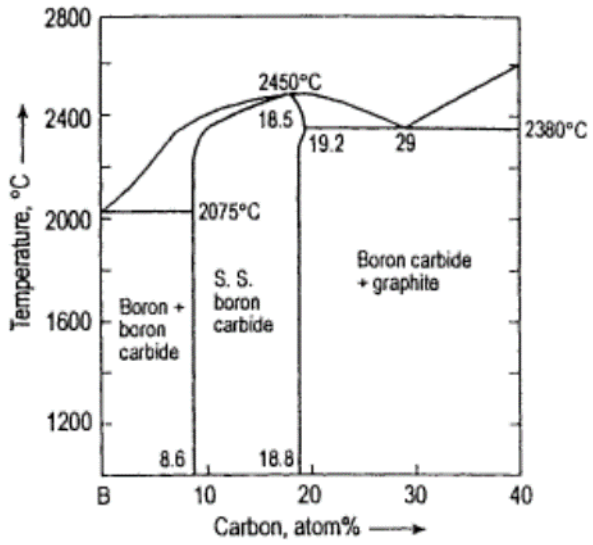


Figure 5: B – C Phase diagram showing B_4C composition range according to Schwetz et al.[46]

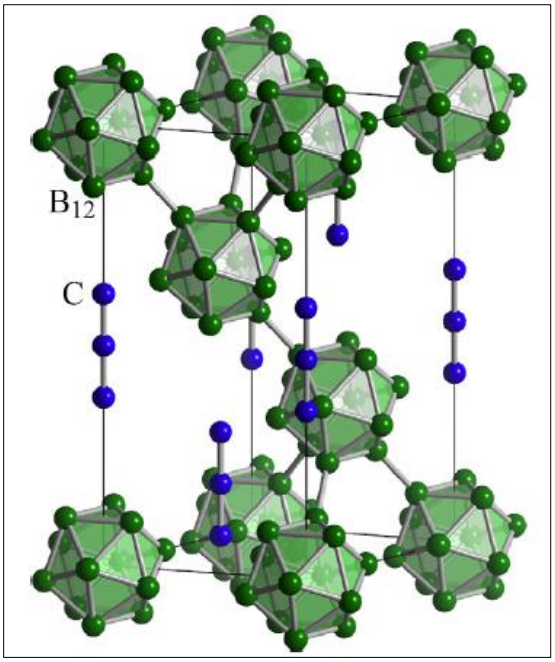


Figure 6: Crystal structure of B_4C as shown by Norimatsu et al.[45]

The method chosen for the preparation of boron carbide is generally governed by the application and the purity of the B_4C needed. Boron carbide is produced on both an industrial and laboratory scale. The industrial scale typically involve the reduction of boron oxide or boric acid using carbon or a combination of carbon and magnesium.[2,5,47,48] This provides comparatively cheap

powder which is used for grinding grit and boronization processes.[2,49,50,51] For applications where a high purity powder is required (ceramic components) B_4C is produced using laboratory scale techniques including chemical vapor deposition, direct reaction of boron and carbon and through pyrolysis of boron trihalides with methane or carbon tetraiodide as carbon carriers.[2,5,52] Reaction 1 shows the CVD process for boron production from boron trichloride.[2,5,52]

$$4BCl_3 + 4H_2 + CH_4 \rightarrow B_4C + 12HCl \qquad \text{Reaction 1}$$

A number of techniques have been reported for sintering boron carbide powders. The main techniques that have been used are pressureless sintering, hot pressing, hot isostatic pressing and more recently spark plasma sintering has gained popularity; whilst laser, microwave and explosion techniques have also been applied.[2,5,53-57] There are a number of inherent difficulties associated with sintering boron carbide; strong covalent bonds, low plasticity and a high resistance to grain boundary sliding.[5,58,59] Boron carbide is also sensitive to oxygen and as a result, typically has a B_2O_3 layer at the surface. At temperatures above 1500°C vapour phase reactions take place (eg. reaction 2); this is responsible for evaporation/reprecipitation during sintering which introduces porosity into the sample as there is significant grain growth but no shrinkage.[5,6,60]

$$5B_2O_{3\,(g)} + B_4C_{(s)} = 14BO_{(g)} + CO_{(g)} \qquad \text{Reaction 2}$$

Pressureless sintering has been performed under an inert atmosphere with and without additives, but in both cases there is a need for high temperatures.[2,5,61] Without additives, temperatures close to the melting point of boron carbide (2200-2350°C), as well as a fine grain size (< 3µm) are required, as it has been seen that powders with a size > 8µm cannot be successfully sintered.[5] Amorphous carbon and a number of inorganic and metallic additions (Al, Si, Mg, Al_2O_3, TiB_2, SiC) have been used as additives when pressureless sintering in an attempt to improve densification and also lower the required sintering temperature.[2,5,6,62] Even with the additions, temperatures ranging from 1800 to 2200°C are still required and the improvement in densification is generally at the expense of the mechanical properties.[2,5,6,61]

The use of hot pressing to consolidate boron carbide powders allows for the application of pressure during the sintering process, which in turn allows for increased densification as compared to pressureless sintering of pure B_4C. Sintering of pure B_4C still requires high temperatures 2100 - 2200°C which once again leaves the materials susceptible to excessive grain growth.[2,5,59] The temperature requirements for the hot pressing process, have also been decreased (1750 - 1900°C) with the addition of sintering aids.[2,5,59] Although the combination of the lower sintering temperature and the additional phases restrict grain growth, some of the benefits of using pure B_4C are lost. It was shown by Champagne et al.[63] that there is significant diffusion of carbon from the die into the sample during hot pressing, particularly for those with higher boron contents (B_xC, $x > 4$). It was also seen that there was no diffusion of the boron towards the die wall, only the carbon into the sample.[5]

Hot isostatic pressing of pure boron carbide has been successful using glass capsules.[5] Boron oxide glass capsules have been used in an attempt to limit chemical interactions between the capsule and the boron carbide powder as this could have a negative impact on the integrity of the capsule during the sintering process.[2,19] Lower sintering temperatures are implemented for the production of samples with high relative densities as a result of the high pressures. Fully dense boron carbide has been produced using the HIP process at temperatures of 1700°C, a gas pressure of 200 MPa and a soak time of 60min.[2,64] HIP has also been used as a post sintering treatment to improve densification of samples that were initially subjected to pressureless sintering or hot pressing. Theoretical densities > 99% can be obtained with the use of a HIP treatment on pre-sintered boron carbide samples which are 93-97% dense with temperatures of 2000°C and isostatic gas pressures of 200MPa. These materials are typically doped as discussed previously and are again prone to excessive grain growth with temperatures in excess of 2000°C.[2,5,65-67]

More recently, attempts to sinter boron carbide using spark plasma sintering (SPS) have shown some success with relative densities greater than 99% being obtained as summarized in Table 1.[53-57,68] A wide range of sintering temperatures (1600-2200°C) have been observed in the production of dense B_4C materials using SPS, but the process still required high temperatures, up to 2200°C, for densification.[59] As with the previously discussed sintering techniques, at these

temperatures, boron carbide is susceptible to excessive grain growth. Hayun et al.[56] investigated the effect of various heating rates, temperatures, pressures and holding times on the densification and grain growth of pure boron carbide. This showed abnormal grain growth in the materials with lower heating rates (50°C/min) above 2050°C. The grain growth was suppressed when using a heating rate of 600°C/min with no hold time at 2200°C.

Table 1: Summary of sintering parameters, densification and properties of boron carbide produced using FAST/SPS from various sources.[53-57,68,69]

Sintering Temperature (°C)	FAST Sintering Parameters	Relative Density (%)	Hardness (GPa)	Fracture Toughness (MPa.m$^{0.5}$)	Bending Strength (MPa)	Source
1650	25 - 50°C/min, 32 MPa, 5 min	82.6	-	-	-	Klotz et al.[53]
1700	100 °C/min, 20 MPa, 5- 10 min	94	-	-	-	Nadaraia et al.[68]
1800 - 2000	50°C/min, 32 MPa, 2 min	96	-	-	-	Frage et al.[69]
1750	88 MPa, 2 -30 min	92.5 - 99.2	18.2 - 27.5	2.81 - 3.61	-	Ghosh et al.[54]
1600 - 1800	100 °C/min, 75 MPa, 0 -10 min	90.3 - 100	22.8 - 36.4	1.88 - 4.81	-	Moshtaghiou et al.[57]
1800 - 2200	50 - 600°C/min, 32 - 51 MPa, 0 - 10 min	70-100	32±2	3.9 - 4.9	200 - 400	Hayun et al.[55,56]

Sigl et al. investigated the effect of grain size on the fracture toughness and flexural strength of B_4C-TiC and B_4C doped with amorphous carbon as seen in Figure 7.[58] These results showed the flexural strength of the materials to decrease with increasing grain size whilst the fracture toughness of the materials was seen to peak between 10-15µm. The peak in fracture toughness was a result of a transition from intra to intergranular crack propagation.[58]

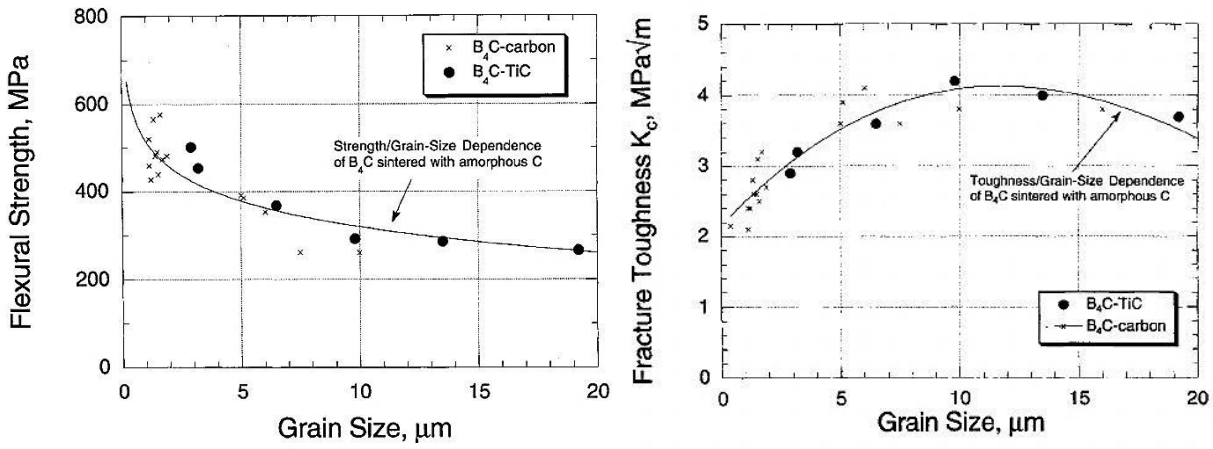


Figure 7: Effect of grain size on the flexural strength and fracture toughness of B_4C-TiC and B_4C doped with amorphous carbon as reported by Sigl et al.[58]

Titanium added to B_4C materials has previously been seen to react, forming TiB_2, TiB and TiC_X.[70,71] Most commonly these materials are prepared through the sintering of various TiB_2-B_4C combinations. TiB_2 additions between 20-40 vol.% to B_4C have been shown to improve the fracture toughness of the materials. A number of mechanisms have been suggested for the increase, including crack deflection as a result of the presence of the secondary phase and also microcracking around the TiB_2 phase in the presence of excess carbon. This is a result of the generation of thin carbon interlayers at the grain boundary interfaces resulting in a weak fracture path between the B_4C and TiB_2.[72-74]

Boron carbide is known to have good wear resistance in a number of environments. As a result of the high hardness and strength of B_4C, only diamond has a superior abrasive resistance.[2,75] The major industrial application of boron carbide is as an abrasive media in polishing and grinding applications, however its hardness and wear properties have also seen its use expanded to ceramic nozzles and lightweight armour plates (also a result of the low density and high Hugoniot elastic limit).[3,4]

2.3.2. Fe-B-C Composites

Typically, the Fe-B-C alloy is a high boron cast alloy in which the Fe_2B formed acts as a strengthening phase.[7,8,76] Since these materials are produced from cast irons, they generally contain other elements such as Cr, Mn, Ti, Cu, Si.[7,8,76,77] Materials such as tungsten and chromium have also been added to improve the fracture toughness of the Fe_2B phase that is formed.[78]

Boron activates sintering of iron and steels due to the formation of a liquid iron boride phase. This combined with the fact that boron has an affinity to oxygen allows for the production of sintered steels with improved mechanical properties- an excellent combination of hardness and ductility can be obtained.[9]

Turov et al.[79] showed that there is active interaction between Fe and B_4C powders at temperatures of 850 – 900°C and the formation of Fe_2B and FeB phases at temperatures between 1050 and 1150°C. It was observed that gas-transport processes in the Fe-C-B system at temperatures ≤1000°C result in the B_4C breaking down, which allows for the formation of a layer of iron borides on the internal pore surfaces.[9] Temperatures ≤1000°C do not however guarantee full densification of the iron matrix; this reduces the composites strength characteristics. Increasing the temperatures into a range of 1000 – 1200°C in the Fe-B-C system allows for the formation of an iron boride liquid phase which assists the densification process.[79-81]

Boron sintered steels have been seen to have properties similar to those of 100Cr6 bearing rolled steel, even though there is a presence of residual porosity. When sintering Fe-B_4C powder mixtures, there is a formation of porosity as a result of the dissolution of boron carbide particles in contact with the iron matrix.[9] This can be seen in Figure 8 showing samples with additions of 3 wt. % to B_4C, sintered at 900°C.

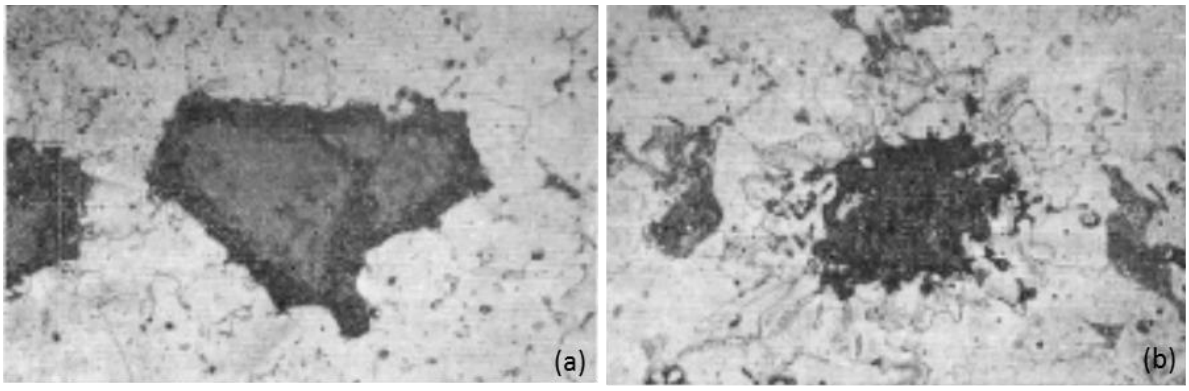


Figure 8: Optical micrograph of Fe+3 wt. % B_4C powder mixture sintered at 900°C for 10 (a) and 120 (b) min. From Bagliuk et al. [9]

An advantage of the boron sintered steels is that they have a high wear resistance which can meet the requirements of modern technological processes.[9,10] This is a result of the heterophase structure and the presence of hard eutectic components; the amount of these components increases with an increase in boron and carbon composition in the starting powder mixture.[9] Phase diagrams of the Fe-B-C system for temperatures relative to this project are shown in ASM Alloy Phase Diagram Center - Diagram No's: 2000010, 2000009, 2000362.[90]**Error! Reference source not found.** Fe-B-C materials in these areas of the phase diagram have been produced using a number of techniques; melt-quench, casting, boriding and sintering. The materials produced have shown a wide range of hardness values (7 – 22 GPa) and fracture toughness values between 2.01 and 4.65 $MPa.m^{0.5}$ have been reported.[10,78,82-89]

In contrast, when a small amount of Fe is added to B_4C powder, they react to form hard iron boride phases within the B_4C matrix. Aizenshtein et al.[91] showed 5.5 vol. % Fe reacting with B_4C to have an interaction zone consisting of a mix of FeB and graphite. In their work, phase diagrams for the Fe-B-C system were also produced for temperatures in the range of 1200-1650°C (Figure 10). These suggest that at low Fe additions to B_4C material, FeB will form and not Fe_2B. It is also evident that at temperatures above 1650°C B_4C will be in contact with a liquid phase containing all the iron. Further work on these materials was performed by Frage et al.[69] who observed the effects of the iron on the densification of the materials using SPS.

Although the composites in this case were fully densified, it was seen that there was pull-out of the FeB phase from the B_4C matrix, as shown in Figure 9. This was caused by interfacial, thermal residual stresses that build up during the cooling process. This is a result of the large difference between the thermal coefficients of the FeB and B_4C.[69] ($\alpha_{B_4C} = 4.5 \times 10^{-6}K^{-1}$ and $\alpha_{FeB} = 12 \times 10^{-6}K^{-1}$)

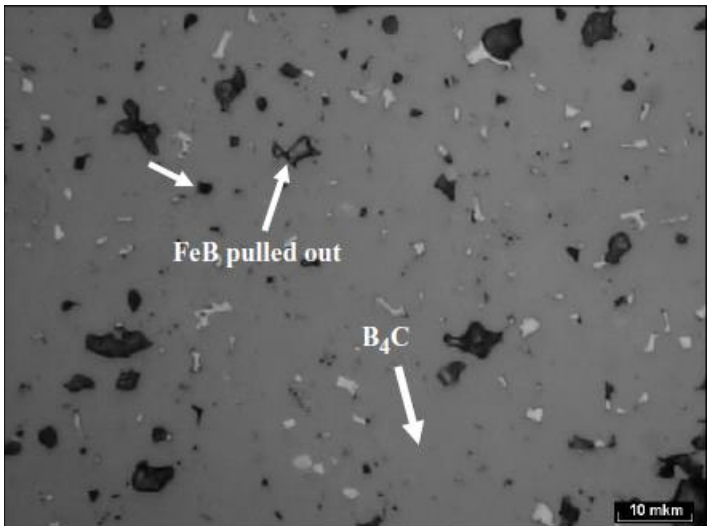


Figure 9: Optical image of B_4C–FeB composite sintered at 2000°C as shown by Frage et al. [69]

Mizrahi et al.[92] and Frage et al.[69] sintered B_4C with 3.5 and 5.5 vol. % Fe additions using pressureless and spark plasma sintering respectively. At 2000°C, Frage et al. achieved up to 96% densification, while the pressureless sintered samples produced by Mizrahi at 2100°C had a hardness of ≈ 26.5 GPa.[69,92]

Components made from steels that are prone to wear (machine parts, cutting tools, etc.) use a range of materials, although hardened steels are used, surface hardened materials are common through carburizing and boronizing techniques.[93-95] These involve the diffusion of carbon and boron into the surface of the steel at elevated temperatures in order to produce an iron carbide or iron boride layer respectively. The carbide/boride layer formed is harder than the steel and improves the wear resistance of the components.[93-35]

In Fe-B-C cast alloys, Fe_2B also acts as a strengthening phase in providing a wear resistant material.[8] The Fe_2B phase is a brittle phase which leaves it prone to cracking and abrasion wear even at low stresses. [96] Huang et al. showed small additions of tungsten to form a $(Fe,W)_2B$ solid solution with the Fe_2B phase significantly improved the fracture toughness of the phase with a reported increase from 3.8 to 6.9 $MPa.m^{0.5}$. [78]

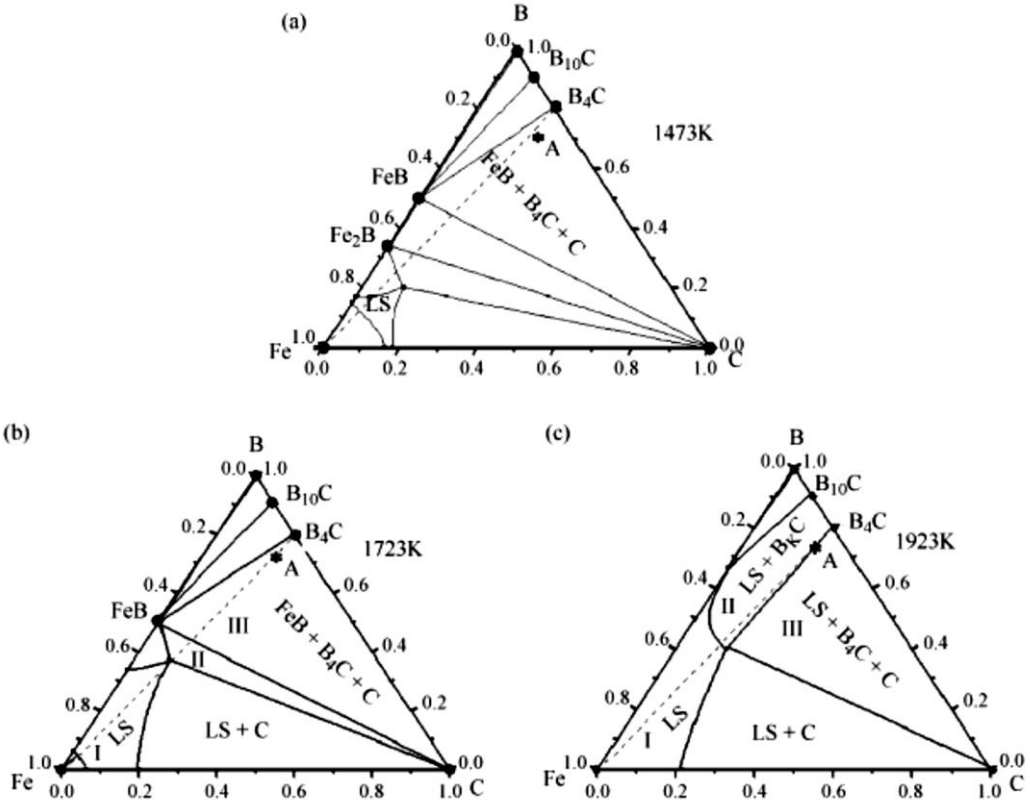


Figure 10: Isothermal sections of the Fe-B-C phase diagram at (a) 1473K, (b) 1723K and (c) 1923K as calculated by Aizenshtein et al.[91]

2.4. Mechanical Properties

2.4.1. Hardness

The hardness of a material is defined as its resistance to deformation by abrasion or surface indentation.[16,18,20] Abrasion tests involve the direct comparison of the material being tested to another material, the harder material is able to scratch the softer material.[97]

Indentation tests involve indenting a flat, polished surface of the material being investigated. The indentation and conditions under which it was produced are analysed and used to determine the hardness of the material. Although a number of techniques have been developed, involving different types, sizes and shapes of indenter, they are all based upon the same principles as per equation 3.[18,97,98]

$$H = \frac{P}{A_i} \qquad \text{Equation 3}$$

Where; H = hardness, P = load (kg) and A_i = area of indentation (mm^2)

Table 2 shows formulae for different testing techniques based on equation 3.

Table 2: Comparison of indentation hardness testing techniques.[18,20]

Test	Indenter Type	Hardness	Applications
Rockwell	Diamond cone, steel balls		Steels and metals with a machined surface finish.
Brinell	10mm steel or tungsten carbide balls	$HB = \frac{2P}{\pi D\left(D - \sqrt{D^2 - d^2}\right)}$	Forged, rolled, cast ferrous and non-ferrous alloys.
Vickers microhardness	Diamond pyramid	$HV = \frac{1.854P}{D^2}$	Metal alloys and ceramics.
Knoop microhardness	Diamond pyramid	$HK = \frac{14.2P}{l^2}$	Metal alloys and ceramics.

The Vickers and Knoop indentation testing techniques are used with ceramic materials, with the Vickers method being most commonly applied.[97,98] Although both tests make use of a diamond

pyramid indenter, the shapes of these differ with an elongated pyramid used for Knoop tests and a square pyramid with an apex angle of 136° associated with the Vickers technique.[14,18]

A number of factors influence the hardness of materials; these include the manner in which the hardness test is performed as well as the characteristics of the materials being investigated. Vickers microhardness indentations on ceramic materials are performed at low loads of 0.05-5 N. This results in small indentations which if smaller than the grain size of the sample have the advantage of determining the hardness of individual grains, but also the disadvantage of not reflecting a representative hardness of the material.[97,98] Higher loads increase the indentation size and the chances of producing more representative hardness in polycrystalline samples. Higher loads are also associated with the introduction of microcracks from the edges of the indentation which are used in the measurement of indentation fracture toughness but also influence the plastic flow within the material and hence the determination of the hardness as there is an increased chance of plastic recovery occurring.[98]

The hardness of ceramic materials themselves is affected by the grain size of a material.[99,100] The materials obey the Hall-Petch relationship which shows that decreasing the grain size of the material results in an increase in the hardness. In ceramics this is valid down to a certain critical grain size below which there is a decrease in hardness.[101] It has been suggested that this is a result of a move from dislocation slip to grain boundary slip having the greater influence over plastic deformation.[102] An example of this effect was observed by Qi et al. where ZrN had a critical grain size of approximately 16 nm, as shown in Figure 11.[103] This is specific to ZrN, however the same occurs in other materials with the difference being a shift in the critical grain size value. Porosity also influences the hardness of ceramics with higher porosities relating to substantial decreases in hardness.[104,105]

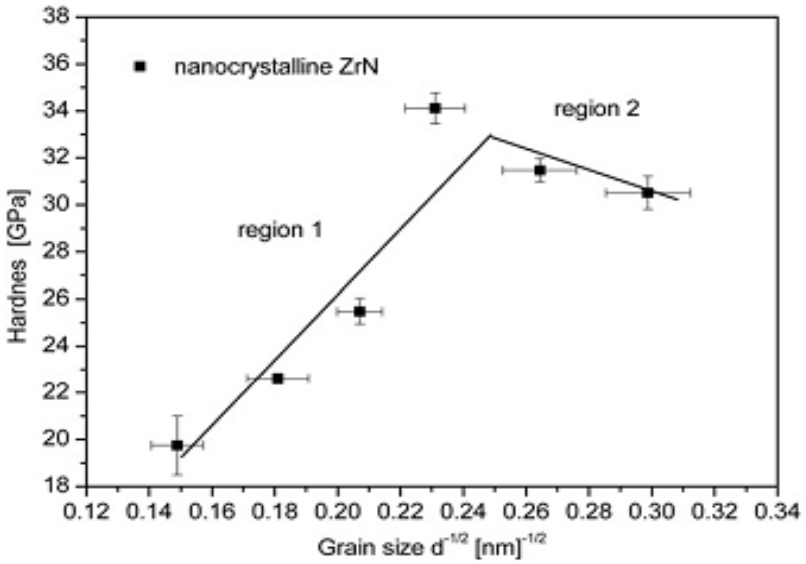


Figure 11: Hall–Petch plot of hardness of nanocrystalline ZrN coatings against the inverse square-root of grain size.[103]

2.4.2. Fracture Toughness

Fracture toughness refers to the critical value of the stress intensity factor for which crack propagation occurs and can be expressed as per equation 4.[14,15]

$$K_{1C} = f\sigma\sqrt{a\pi} \qquad \text{Equation 4}$$

Where; K_{1c}= fracture toughness, f = shape factor, σ = applied stress (MPa), a = flaw size (m).

Several factors have been shown to affect the fracture toughness of a material.[20,100] Flaws act as stress raisers within a material and larger flaws decrease the stress required for crack propagation lowering the fracture toughness. Ductile materials, such as metals, that plastically deform have a significantly higher fracture toughness than their brittle ceramic counterparts. Plastic deformation allows for the tip of a crack to become blunt which hinders the propagation of the crack leading to increased fracture toughness.[18] The grain size of the material also plays a role in the fracture toughness of a material, with smaller grain sizes typically resulting in higher

fracture toughness.[100] The fracture toughness values for a given material have been shown to be significantly influenced by both the technique used to measure it and also the preparation of the sample.[15,100]

i. Single edge notched (SENB) and V-notched bend (SEVNB) tests

The bend test methods used to determine the fracture toughness make use of a bar prepared to set dimensions. The notch is then introduced to the sample and the test performed. The purpose of the notch is to introduce a flaw of known size (ideally atomically sharp), from which cracks will propagate under an applied stress, leading to failure.[14,15,106] The various test methods used are very similar although the main difference that is observed is the shape of the notch used to introduce the flaw. It must be noted, that these test results can vary significantly between samples as a result of small dimensional differences and difficulties with introducing an atomically sharp flaw.[15,106,107] A flaw that is not atomically sharp results in an overestimation of the fracture toughness. The SEVNB test is more difficult to prepare compared to the SENB test but it allows for more stable crack growth and, as the crack extends, there is a chance of introducing an atomically sharp flaw. [14,15] The SENVB test is a standard method used for determining fracture toughness often applied to ceramic materials as shown in ASTM C 1421-09. [108,109]

ii. Indentation fracture method

A common technique used to determine the fracture toughness of ceramics is by indentation fracture toughness. This involves measuring the length of the cracks produced at the corners of a Vickers indentation during loading.[97,110] Two types of cracks can be produced using this method, median (half-penny) or Palmqvist cracks. [15,97,110] The type of cracks present determines the manner in which the fracture toughness is calculated; as a result, a number of methods have been developed. [97,100,111-114] The crack mechanism

present should be determined by lightly polishing the surface post indentation and observing the appearance of the cracks. Post polishing, median cracks will still appear to propagate from the corner of the indentation whilst with Palmqvist cracks there will be a smooth polished surface between the corner of the indentation and the apparent start of the crack as shown in Figure 12. [15]

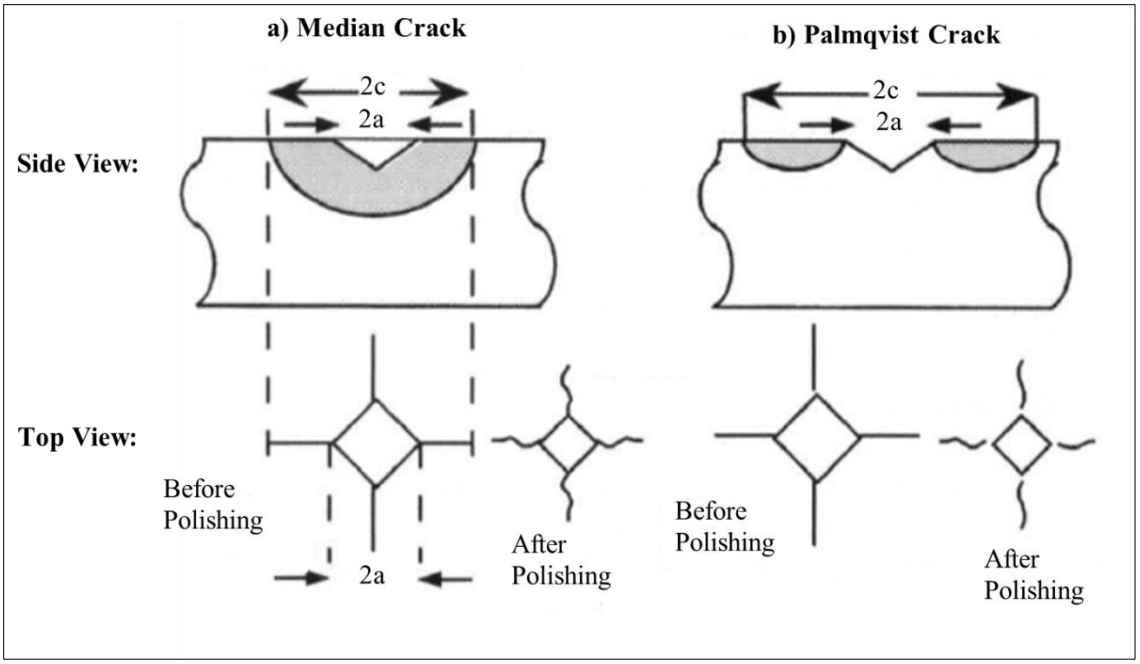


Figure 12: Schematic showing side and top views of a) median and b) Palmqvist cracks produced using Vickers indentations and the effect of polishing in the determination of the type of crack. (adapted from Barsoum) [15]

The indentation method is much simpler to perform as the sample preparation requirements are significantly less, needing a flat polished surface only, and also the sample is not destroyed allowing repeat tests to be carried out on the same samples if it is required. Although this is advantageous, it must be considered that the indentation method is usually not as accurate as the results from the bend tests.[110,115] Quinn et al. has shown that indentation fracture toughness can be used as a relative comparison of a specific material, but not as a representation of the actual fracture toughness of the material.[116]

2.4.3. Transverse Rupture Strength

The tensile strength is typically considered more important than compressive strength when assessing the strength of ceramics in relation to their probability of failure. [117,118] This is a result of the high compressive strengths associated with ceramics and their susceptibility to failure under tensile conditions. The strength measurement of ceramics is generally subject to significant variability as a result of the dependence of the strength on the size and distribution of flaws within the material.[15,117,119] Consequently, there is a considerable variation in strength from specimen to specimen under identical testing conditions. In order to accommodate this variability, statistical analysis is applied over a sample set to determine the characteristic strength of a material. [117] Several probability models have been developed for the analysis of strength data including Weibull, normal and log-normal. [120,121] The Weibull distribution model characterises the strength of brittle materials and is thus suited for use with ceramics.

The generalized equation for the probability of failure of a sample is expressed in equation 5[122]

$$P_s = 1 - P_f = \exp\left[-\mathrm{kV}\left(\frac{\sigma}{\sigma_0}\right)^m\right] \qquad \text{Equation 5}$$

Where; P_f = probability of failure, σ = stress (MPa), P_s = probability of survival, σ_0 = Characteristic Strength (MPa), m is the Weibull modulus, k is a dimensionless function of m and characteristic of the test method and specimen geometry. kV is referred to as the effective volume of the of the test specimen.

The Weibull modulus is an indication of flaw distribution within the test samples. A greater Weibull modulus value is favoured as it suggests that there is a more uniform flaw distribution.[120,121] The parameters m and σ_0 can be determined using a maximum likelihood method as per BS EN 843-5.[123]

Transverse rupture strength (TRS) or modulus of rupture is often used to describe the bending strength of ceramics and takes into account a shear, compressive and tensile strength component.[15,124] The TRS of a material refers to a maximum stress at the point of failure during loading. A number of testing methods have been developed to measure the strength of ceramics.

These include various uniaxial and biaxial testing techniques. [125] As an example, the 3-point and 4-point bend tests make use of a uniaxial load whilst for the ball on three balls (B3B) technique it is biaxial. A number of limitations associated with the use of a uniaxial load have previously been reported. These include; strict geometry requirements which are difficult to ascertain, the tendency of ceramics to fracture when they are gripped and alignment of the test pieces in the apparatus is crucial in avoiding the presence of bending stresses. [19,117] These are limitations as ceramics tend to fail at strains of ≈0.1 % and as a result, the experimental setup is particularly important in producing reliable results. Biaxial strength tests have the advantage of being able to be applied to specimens of various shapes and sizes. Apart from the simpler sample preparation requirements, biaxial tests avoid tensile loading at the samples edge and are considered to expose defects more readily than uniaxial techniques.[125]

Common biaxial strength testing techniques that have been developed include; ring on ring, punch on ring, ring on ball and four balls on ring tests.[126,127] The main advantage of the ball on three balls test when compared to other biaxial testing methods is that it can tolerate small geometrical inaccuracies of the specimen or test assembly, a low influence of friction, and edge defects are not relevant; tests may also be carried out on discs with no surface finish (as sintered).[127]

2.4.4. Wear Resistance

The majority of mechanical applications at room temperature (cutting tools, armour, nozzles, etc) that make use of ceramics, do so to take advantage of their hardness, wear and corrosion resistance properties.[15] Wear has been defined as “the progressive loss of material due to the tribological interactions at contacting interfaces under relative motion”.[128] Wear is often detrimental in engineering applications and can lead to failure of components. Thus the wear resistance of these materials has become more important, particularly as the physical demand on components increases as technology advances. Wear occurs through a number of mechanisms which can which can be present in isolation or multiple mechanisms can act simultaneously. The main wear mechanisms are abrasive, adhesive and tribochemical wear.[128] Although the

hardness of ceramics typically gives the good wear resistance, their brittle nature leaves them susceptible to abrasive wear.[20] Grain pull-out due to weak grain boundaries and cracking through abrasion are responsible for wear loss in ceramics.[14]

2.4.4.1. Abrasive Wear

Abrasive wear involves the removal of material from the surface of one body through the cutting action of another. [129] A harder body will cut into a softer one, forming a groove on the surface of the weaker material resulting in its removal.[128-130] In ductile materials long ribbon shaped wear particles are formed due to the cutting action of the abrasive body whilst in brittle materials (ceramics) the wear particles are formed through crack propagation due to their resistance to plastic deformation.[131] If the abrasive contact is great enough, the cracks can penetrate below the surface and form small multi-directional localized cracks resulting in high wear rates.[128] In ductile materials, it is possible for worn material on the mating surface to form hard asperities, which can break-off and increase the aggressiveness with which wear occurs. This may be a result of phase transformations, new phases forming due to interaction with the mating surface or due to work hardening of the wear debris.[128-130] Thus, abrasive wear may occur as two-body abrasion mechanism or a three-body mechanism when an abrasive particle is present between the two original bodies. In this case both bodies are prone to being worn by the third body.[132,133] This wear is common in grinding and polishing operations. Materials with a high hardness, hot strength and good toughness are most resistant to abrasive wear. [20]

2.4.4.2. Adhesive Wear

Adhesive wear occurs when there is localized bonding at the surface, followed by fracture as two bodies move in contact with each other (usually under high load) resulting in the removal of material from the surface, while the counterbody gains material.[128-130] This material is referred to as the transfer film.[128] When the adhesive bond strength is strong enough to resist the sliding between two bodies, there is plastic deformation in the contact area. This is caused by dislocation

movement at the contact surface which is subjected to shear and compression forces allowing slip to occur along the slip planes.[130] The deformation results in the initiation of a crack which propagates to the contact surface allowing for the removal of the material. [130] During this process there is often a back and forth transfer of material between the two bodies producing wear particles consisting of two surfaces made up of the interacting bodies.[129,134]

Wear results in the formation of irregular holes or pits on one material and projections on the other which can break free from the contact surface and may act as small abrasive particles causing further wear.[128,130,135,136] Metals are most notably prone to adhesive wear due to their susceptibility to plastic deformation, especially those with weak contaminant layers (oxides) or those that do not form oxides.[128]

2.4.4.3. Tribochemical Wear

Tribochemical wear occurs when there is removal of material formed as a result of reactions between the surface and the environment or between two materials in contact with each other.[20,128] As material diffuses from a surface there is a wear loss. The solubility of the materials in contact with each other affects wear rate as well.[20] New phases formed may be prone to other types of wear resulting in an increased wear rate. Due to the nature of tribochemical wear, in some cases it has been seen to be beneficial to the overall wear rate as a protective layer can form reducing the friction between two bodies moving in contact with each other.[128]

2.5. Approach to Study

The use of low cost boron carbide and iron powders has the potential to produce cost effective Fe-B-C composites with attractive properties. This project will provide information on the hardness, fracture toughness, transverse rupture strength and abrasive wear resistance of selected compositions sintered using spark plasma sintering.

The composition ranges selected for investigation in this project are those with a high iron content (≥ 69.3 vol. %) and those with low Fe additions (≤ 5 vol. %). The amount of iron present in the low Fe compositions was limited to 5 vol. % to prevent the loss of liquid phase during sintering and was investigated to observe the effects of Fe as a sintering aid in producing B_4C composites with high hardness values (> 25 GPa). The high Fe compositions were selected based on the potential reactions 3 and 4, and are investigated as the potentially cheap to produce compositions associated with the high Fe content.

$$11Fe + B_4C = 4Fe_2B + Fe_3C \qquad \text{Reaction 3}$$

$$7Fe + B_4C = 4FeB + Fe_3C \qquad \text{Reaction 4}$$

The 69.3 and 78 vol. % Fe-B_4C compositions relate to mole ratios of 7 Fe:1 B_4C and 11 Fe:1 B_4C respectively. 80.9 vol. % Fe-B_4C corresponds to a mole ratio of 13.1 Fe:1 B_4C and was investigated to observe the effects where iron was in excess with regards to reaction 3.

The use of spark plasma sintering has the potential to produce a range of Fe-B-C compositions with improved properties. The high heating rates and the addition of pressure allow for full densification of materials using shorter sintering times and lower temperatures.[11,12,13] The faster sintering times with lower temperatures may allow for the reactions to be incomplete and as a result, unreacted iron and B_4C may still be present giving improved toughness and hardness respectively.

3. Experimental Procedure

In this section, the experiments used to achieve the objectives of this project will be discussed. It includes the materials, equipment and the methods used to perform the relevant experiments. The procedure was broken down into the processing of the powders, the sintering of these powders and the characterization of the sintered samples.

Table 3 shows the relevant materials used in this project as well as the supplier from which it was obtained.

Table 3: Suppliers of all powders used in this project.

Material	Product Code	Particle size	Purity (%)	Supplier
B_4C	43002	< 10 µm	≥ 99	Alfa Aesar, GmbH & Co KG.
Fe	44890	1-10 µm	≥ 99.5	Sigma-Aldrich (Pty) Ltd.
Ti	42624	< 44 µm	99.5	Alfa Aesar, GmbH & Co KG.
Ethanol		N/A	≥ 99	School of Chemistry, University of the Witwatersrand

3.1. Powder Processing

3.1.1. Particle Size Analysis

Particle size analysis (PSA) was carried out using a Malvern Mastersizer 2000 to determine the size distribution of the powders. The d_{10}, d_{50} and d_{90} values (diameter of particles with cumulative fractions below 10, 50 and 90 % respectively) were used to characterize the powders. The Malvern software analyzes the scatter patterns produced using the Fraunhofer model in order to calculate the size of the particles.

Powders were each dispersed in an ultrasonic bath in order to remove agglomeration and provide an accurate size analysis. A small amount of powder was added to a beaker with enough ethanol to form a paste with a solids loading of 60 vol. %. A small amount (1 wt. % with respect to the powder) of PEG 400 was used as a dispersant to assist the removal of agglomerates. The beaker

with the paste was placed in the ultrasonic bath until a well dispersed, unimodal size distribution was obtained. During this time ethanol lost through evaporation was replenished to maintain the consistency of the paste. PSA tests were performed every 10 minutes by adding the required amount of material from the dispersed paste, to the Malvern equipment, for an adequate obscuration range for testing. Unimodal size distributions were obtained within 30 minutes of ultrasonication, for each of the powders being investigated, with little to no change in distribution with longer exposure times.

3.1.2. X-Ray Diffraction on Powders and Composites

X-Ray diffraction (XRD) analysis was performed using a Bruker D2 instrument to determine the phases and any impurities present in the starting powders. Sintered composites were prepared for XRD (as per section 3.2.3) for determination of the phases present and the effect of the starting composition on the evolution of said phases. Both the powders and sintered composite materials were subjected to the same scan parameters. Co Kα radiation was generated at 10 mA and 30 kV to produce diffractograms over a range of 10 to 120° with a step size of 0.026 °2θ and a scan step time of 3.8 s. These were analysed using EVA© software (Bruker) in conjunction with the International Centre for Diffraction Data (ICDD) database (2015).

3.1.3. Scanning Electron Microscopy on Powders and Composites

A Carl Zeiss Sigma field emission gun scanning electron microscope (FEG-SEM) was used in the characterization of the powders and the sintered composites.

A small amount of powder was placed on a stub using graphite tape. The stub was blown using compressed air to remove any powder that was not adhered to the tape before being placed in the SEM. Secondary electron images of the powders were captured allowing for the morphology and size of the various powders to be observed and compared to the PSA results and the sizes quoted by the supplier.

Sintered composites were prepared for SEM analysis as per section 3.2.3 to evaluate and compare their microstructures. Samples produced were conductive and no further treatment was required for SEM analysis. As the composites were conductive, they were observed by positioning the piece being investigated directly on a stub using graphite tape. As the resin used for the samples subjected to wear tests was non-conducting, silver tape was used to supply a continuous connection from the sample to the stub which was sufficient for SEM analysis.

Energy dispersive X-Ray analysis (EDX) was used in conjunction with SEM and XRD analysis to identify the phases observed.

3.1.4. Washing of B_4C

B_4C powders were washed in ethanol to remove the B_2O_3 oxide layer at the surface. This was done by mixing 100g of B_4C in ethanol using an ultrasonic bath for 5 min. The mixture was placed in the rotary evaporator, initially without vacuum, at a temperature of 80°C which allowed for the ethanol to be boiled off. Once half (approximately) of the ethanol had been evaporated, the temperature was lowered to 50°C where the vacuum was turned on, to dry the powders at a lower temperature and minimize the chance of re-oxidation during drying. Dried powder was placed in an argon filled glove box, sieved to 150µm, vacuum sealed and stored until needed.

3.1.5. Mixing of powders

Powders were mixed using a Fritsch Pulverisette 6 planetary mono mill which is able to operate at speeds of 100 rpm to 650 rpm and perform both wet and dry milling. In the applications for this project, the mill was used to obtain homogeneous mixtures of the materials through wet mixing.

Samples were mixed in a 250 ml stainless steel milling bowl with a tungsten carbide lining with 2 mm steel grinding balls. Powders were milled in 150 ml of ethanol for four hours at a speed of

150 rpm. The powder and the balls used for the milling were carefully weighed using a mass balance with three decimal places to give 11.3 cm^3 of powder in each instance. Table 4 shows the compositions that were mixed along with the relevant powder to milling ball mass ratios that were used.

Table 4: Compositions and relevant mixing and sintering requirements

Sample (Vol. %)	Composition (Wt. %)			Total Mass (g)	Milling Ball:Powder (Mass Ratio)	Mass/sample for sintering (g)	
	B_4C	Fe	Ti			4 mm Height	3 mm Height
1% Fe-B_4C	96.93	3.07	-	28.993	8:1	3.221	2.416
3% Fe-B_4C	91.17	8.83	-	30.203	8:1	3.356	2.517
5% Fe-B_4C	85.85	14.15	-	31.413	8:1	3.49	2.618
69.3% Fe-B_4C	12.39	87.61	-	70.319	5:1	7.813	5.86
78% Fe-B_4C	8.26	91.74	-	75.583	5:1	8.398	6.299
80.9% Fe-B_4C	7.01	92.99	-	77.338	5:1	8.593	6.445
1% (0.8Fe+0.2Ti)-B_4C	97.19	2.46	0.35	28.917	8:1	3.213	2.41
3% (0.8Fe+0.2Ti)-B_4C	91.86	7.12	1.02	29.975	8:1	3.331	2.498
5% (0.8Fe+0.2Ti)-B_4C	86.90	11.46	1.64	31.033	8:1	3.448	2.586
69.3% (0.8Fe+0.2Ti)-B_4C	13.40	75.76	10.84	65.052	5:1	7.228	5.421
78% (0.8Fe+0.2Ti)-B_4C	8.97	79.64	11.40	69.655	5:1	7.739	5.805
80.9% (0.8Fe+0.2Ti)-B_4C	7.62	80.82	11.57	71.189	5:1	7.91	5.932
1% Ti-B_4C	98.22	-	1.78	28.612	8:1	3.179	2.384
3% Ti-B_4C	94.75	-	5.25	29.063	8:1	3.229	2.422
5% Ti-B_4C	91.38	-	8.62	29.513	8:1	3.279	2.459
8% Ti-B_4C	86.51	-	13.49	30.188	8:1	3.354	2.516

The 5 vol. % Ti-B_4C composite was also mixed using tungsten carbide milling balls to observe the effect of the Fe contamination on the properties of the composites produced. Contamination was taken into account by observing wear on the milling balls during mixing. The balls were

weighed before and after mixing for the difference to be accounted for in the relevant samples and the composition adjusted accordingly.

3.1.6. Drying and Sieving

Powders were dried using a Heidolph Laborata 4010 digital rotary evaporator at 58°C using a rotation of 70 rpm. The evaporated liquid was appropriately disposed of and the dried powder was removed for further processing.

The dried powders were sieved consecutively through 400 µm and 150 µm Retsch® sieves with a 20 cm diameter. This ensured the removal of the milling media and that the powder was suitable for sintering. The sieved powder was measured out as required (Table 4) into glass vials, sealed, vacuum packed and stored in a vacuum desiccator. This process was carried out in a glove box under an argon atmosphere to limit the exposure of the powders to oxygen. The samples were stored in a vacuum desiccator prior to sintering.

3.1.7. Sintering

Prepared powders were sintered using a FCT HP-D5 spark plasma sintering furnace. Sintering was performed under vacuum with an absolute gas pressure of 1 hPa. The heating stages of the process used a pulse time of 10 ms with a pause of 5 ms.

Table 4 (section 3.1.5) shows each of the compositions that were sintered as well as the powder requirements to produce composites with a 20 mm diameter and a height of both 3 mm and 4 mm as necessary. Samples were sintered in a graphite die set lined with graphite foil to protect the die. The 20 mm diameter graphite foil disks placed at the bottom and the top of the sample were coated with h-BN in to minimise carbon diffusion into the composites. The as sintered composites were prepared for further analysis by sandblasting the materials to remove any h-BN and excess graphite foil remaining on the surface.

3.2. Characterisation

3.2.1. Density

Ethanol was used to wipe the surface of the composites to ensure there was no remaining dirt from the sandblasting process. The density of the composites produced was measured using Archimedes' principle. Density measurements involved the calculation of the dry weight (W_1), followed by the wet weight (W_2) and suspended weight (W_3) of each material. For the wet weight to be calculated, samples were boiled in distilled water for three hours. The density calculations were performed using a Sartorius balance, with a supplied density kit adaption, which allowed for the suspension of the composites in distilled water and subsequent suspended weight calculation.

The bulk density and open porosity of the samples were determined using equations 6 through 9 (ASTM C373-88 2006)[137] where ρ_w is the density of water at ambient temperatures.

$$True\ Volume\ of\ Sample = \frac{W_1 - W_3}{\rho_w} \quad \text{Equation 6}$$

$$True\ Density\ of\ Sample = \frac{W_1 \times \rho_w}{W_1 - W_3} \quad \text{Equation 7}$$

$$Bulk\ Density = \frac{W_1 \times \rho_w}{W_2 - W_3} \quad \text{Equation 8}$$

$$Percent\ Open\ Porosity = \frac{W_2 - W_1}{W_2 - W_3} \times 100 \quad \text{Equation 9}$$

A standard error was determined for the density calculations; density was calculated once per week on three different samples over the course of three weeks. A standard error of 0.02 g/cm^3 was determined through these tests.

As the B_4C and Fe powders react, the density of the phases present did not correspond with a theoretical density calculated from the starting powder composition. Thus, to quantify the porosity and relative density of the sintered composites image analysis of the cross sections was implemented. Porosity and the subsequent relative density were calculated from three SEM

micrographs (from three different areas) at 2500× magnification, which were analyzed using image processing software (ImageJ).[138]

3.2.2. Cutting

A Struers Secotom-10 precision cut-off machine was used to cut the composites in half to allow for examination of the cross-section. Composites were cut using a 127 mm dia. x 0.4 mm x 12.7 mm dia. diamond cut-off wheel (Struers, M0D13) at a speed of 3500 rpm with a sample feed rate of 0.01 mm/s. The low feed rate ensured that the load was minimized on the cutting wheel.

3.2.3. Grinding and Polishing

Three different techniques were used to prepare the composites for the subsequent characterization tests.

i. Hardness, Fracture Toughness and SEM

One half of the cut composites were mounted for examination of the cross-section. The samples were mounted using a Struers CitoPress – 10 mounting press with Struers PolyFast resin. PolyFast resin makes use of Bakelite with carbon filler which allows for SEM to be performed on the mounted samples. The samples were mounted at 180°C and 250 bar for 3 minutes before being water cooled for one and a half minutes.

The mounted samples were ground and polished using a Leco Spectrum System 2000 automatic polishing machine which allows for the simultaneous polishing of up to six samples. Table 5 gives the breakdown of the procedure followed to produce finely polished composites with a scratch free, mirror finish suitable for Vickers indentation and SEM analysis.

Table 5: Grinding/Polishing procedure

Step No.	Disc Used	Grit Size (μm)	Time (min)	Water Used	Suspension used	Diamond Extender Used
1	MD-Piano	220	15	Yes	No	No
2	MD-Piano	1200	40	Yes	No	No
3	MD-Largo	-	30	No	Yes (9 μm diamond)	Yes
4	MD-Dac	-	15	No	Yes (3 μm diamond)	Yes
5	MD-Nap	-	6	No	Yes (1 μm diamond)	Yes
6	MD-Chem	-	2	No	Yes (OPS 0.01 μm silica)	No

*Grinding/polishing discs, diamond slurry and diamond extender obtained from Struers.

ii. X-Ray Diffraction

The remaining half of the cut composites were used for XRD analysis. The samples were ground by hand using the Struers MD-Piano 220 grit size grinding disc to produce a flat surface, free from impurities, suitable for XRD analysis.

iii. Transverse Rupture Strength

20mm samples were ground by hand using the Struers MD-Piano 220 grit grinding disc until the samples were completely flat on both sides. Once there were no visible defects on the surface the samples were ground at 1200 until all deep scratches from the 220 grit step were removed. The samples were polished using the MD-Largo with 9μm diamond slurry to ensure a scratch free surface for the TRS tests. A surface finish of 9μm was shown by Harrer et al. to be sufficient for the ball on three ball TRS testing technique.[139]

iv. Sliding Wear

Composites were cold mounted using a polyester resin with a catalyst (100 g resin with 20 drops catalyst) which was left to set for 24 hours. Samples were mounted flat for the wear tests to be carried out on the 20mm diameter surface. Like the composites for

hardness and fracture toughness, the wear samples were ground and polished as per the method laid out in Table 5.

3.2.4. Hardness and Fracture Toughness

Hardness

Hardness of the sintered composites was measured using a FV-800 Future-Tech macro Vickers hardness tester using a diamond indenter with a load of 5 kg (HV_5) for 10s used to produce the indentations as represented in Figure 13.

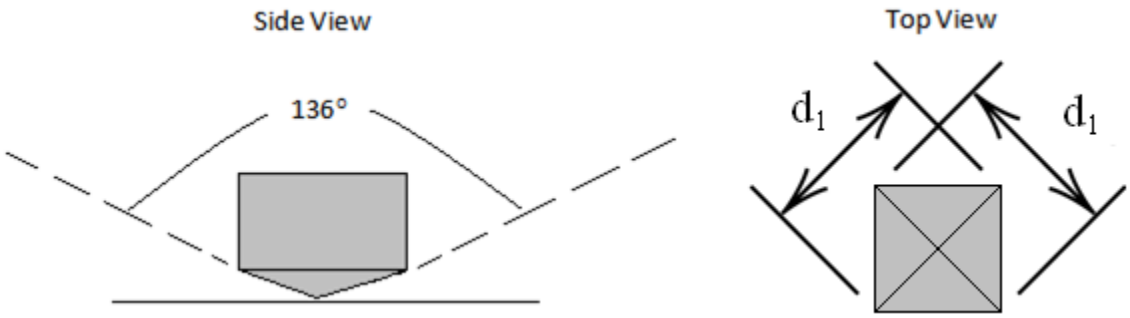


Figure 13: Schematic showing geometry of Vicker's hardness indenter. (Callister, pp 224)[18]

Five indentations were made along the polished cross section of each composite to determine a representative mean. The Vicker's hardness formula shown in Table 2 (chapter 2.4.1) was used to calculate the hardness values[18] It was then possible to convert the hardness into GPa using the relationship in equation 10.

$$H(GPa) = 0.009807 \times HV \qquad \text{Equation 10}$$

Fracture Toughness

Indentation fracture toughness was measured using the same indentations produced for the Vickers hardness tests. The composites produced were found to have Palmqvist cracks which was determined by polishing the samples after an indentation was made and observing the crack under an optical microscope. This was in agreement with those observed by Hayun et al.[55] and Huang et al.[78] working on similar materials. The equations suggested for use on Palmqvist cracks by Shetty et al. were used to determine the fracture toughness (equations 11 - 13). The samples were found to meet the required criteria of $0.25 \leq l/a \leq 2.5$.[112, 140]

$$K_{Ic} = \beta(HW)^{1/2} \quad \text{Equation 11}$$

$$\beta = \frac{1}{3(1-\upsilon^2)(2^{1/2}\pi tan\varphi)^{1/3}} \quad \text{Equation 12}$$

$$W = \frac{P}{4\bar{l}} \quad \text{Equation 13}$$

H = Hardness

υ = Poisson's Ratio

φ = Indenter geometry (standard Vickers indenter: 2φ =136°)

P = Applied Load

$\bar{l}$ = Mean radial crack length

3.2.5. Transverse Rupture Strength

Transverse rupture strength was determined using the ball on three ball method (B3B) as presented by Börger et al.[126] An applet, based on this method, developed by the Institute of Structural and Functional Ceramics, Montan University, Leoben was used to calculate the TRS values based on equations 14 to 16. [126,141]

$$\sigma_{max} = f \times \frac{F}{t^2} \quad \text{Equation 14}$$

Where

F = force (N)

t = thickness of disc

$$f = \frac{3(1+\upsilon)}{4} \times \left[1 + 2 \times ln\frac{R_a}{b} + \frac{(1-\upsilon)}{(1+\upsilon)} \times \left(1 - \frac{b^2}{2 \times R_a^2}\right) \times \frac{R_a^2}{R^2}\right] \quad \text{Equation 15}$$

Where

$$R_a = \frac{2 \times R_b}{\sqrt{3}} \quad \text{Equation 16}$$

R_a = support radius

R_b = radius of the ball

υ = Poison's ratio

Ten TRS measurements per selected composition were carried out on the polished (section 3.2.3) 20 mm discs. The thicknesses of the disks were in the range 1.6 to 1.9 mm, though the tolerance for each specific composition was 0.02 mm to limit volume variations within the samples set. The samples were placed in the B3B jig (University of the Witwatersrand, South Africa) and a pre-load of 10 N was applied to ensure the sample was stable and in position between the balls. The load was applied using a Tinius Olsen H50KT press by setting the rate at which the pistons moved to 0.025 mm/s, which ensured the samples failed in ± 30 s. The maximum force observed before failure was used to determine the TRS values.

3.2.6. Sliding Wear

Sliding wear tests were carried out on selected composites using a CSM pin-on-disk tribometer (Anton Paar GmbH, Germany) to observe the wear resistance of the composites. Tests were carried out using the ball on disk configuration allowing for a load to be applied to a 6mm ball in contact with the flat polished surface of the sample. The wear balls used were INOX 420 stainless steel and silicon nitride allowing for a comparison of the wear properties under different abrasive conditions. Each test was performed using a load of 10 N with a speed of 0.21 m/s over a sliding distance of 300 m in air, without any lubricant and humidity values ranging between 55 and 65 %. The coefficient of friction was monitored using the InstrumX Tribox© software. Each composite was tested three times for an average wear rate to be established.

The wear track was measured using a TR220 portable roughness tester (Beijing TIME High Technology Ltd., China) to determine the cross-sectional area of the wear track and further analyzed using SEM and EDX to observe its appearance and provide information on the phases present. Two wear tests were performed on each composite and the error observed.

The worn volume of the samples (equation 17) was calculated per the Japanese industrial standard (JIS R1613), as used by Jones et al.[142]

$$\Delta V_{Sample} = \frac{\pi \times R \times (S_1 + S_2 + S_3 + S_4)}{2} \qquad \text{Equation 17}$$

ΔV_{Sample} = wear volume (mm^3)

R = sliding radius (mm)

S = cross sectional area of wear track (mm^2).

The wear of the balls was observed using a Carl Zeiss Axiovision optical microscope to determine the diameter of the wear scar on the ball. This allows for the ball volume loss (ΔV_{Ball}) to be determined using equations 18 and 19 (ASTM G133-95 2002)[143]

$$h = \sqrt{r^2 - \frac{d^2}{4}} \qquad \text{Equation 18}$$

$$\Delta V_{Ball} = \frac{\pi \times h}{6} \times \left(\frac{3}{4} \times d^2 + h^2\right)$$ Equation 19

h = height of ball volume lost (mm)

d = diameter of wear scar on ball (mm)

r = radius of wear ball (mm)

The wear rate (k) of the sample and the ball can be calculated using the equation 20.[144]

$$k_X = \frac{\Delta V_X}{F \times s}$$ Equation 20

k_X = wear rate (mm^3/Nm), where X = sample/ball

F = load (N)

s = sliding distance (m)

4. Results

4.1. Powder Processing

4.1.1. Particle Size Analysis and Powder Morphology

The particle size distribution (PSD) of each powder was determined and shown in Figure 14. Unimodal distributions were observed once the powders had been dispersed using ultrasonication, suggesting this was sufficient for removing agglomerates present in the starting powder. The PSD tests allowed for the determination of the d_{10}, d_{50} and d_{90} as summarised in Table 6. The iron powder had the narrowest distribution whilst titanium had the largest with a d_{90} of 53.30 µm.

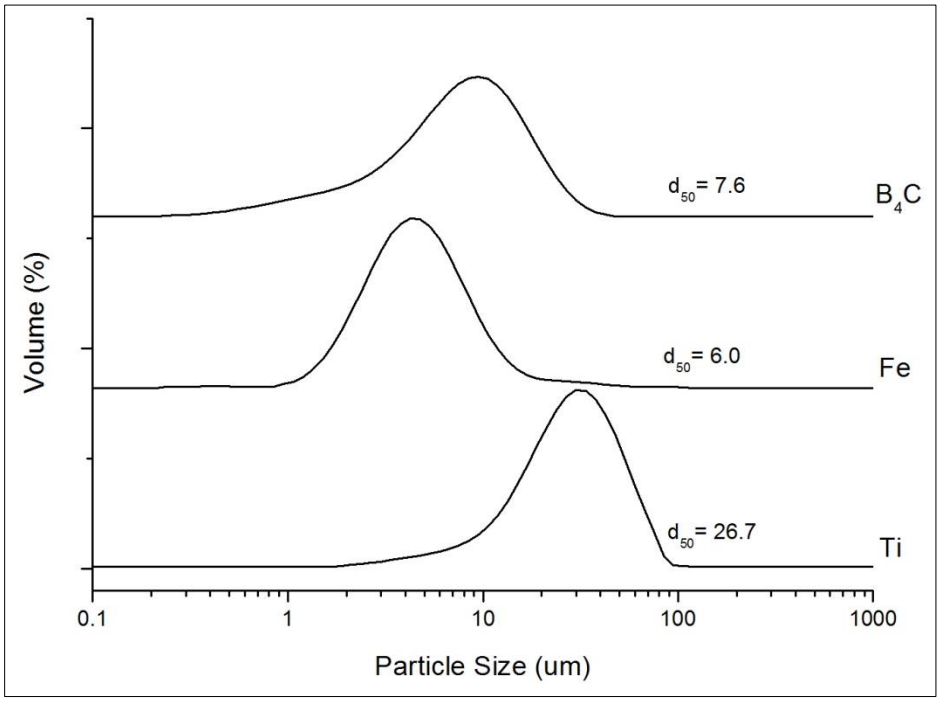


Figure 14: Particle size distribution for the B_4C, Fe and Ti powders.

Table 6: Particle size of the starting powders.

Cumulative Passing Volume (%)	Size (µm)		
	B_4C	Fe	Ti
d_{10}	2.0	2.8	10.6
d_{50}	7.6	6.0	26.7
d_{90}	17.1	13.4	53.3

SEM was used to observe the morphology of the powders and to corroborate the particle size analysis results. Figure 15 shows the secondary electron mode SEM micrographs of the as received powders. The B_4C and Ti powders had a multi-faceted angular morphology and the iron was spherical. Each powder was seen to have agglomerates of large particles decorated with finer ones. It was clear from the SEM results that these and the PSA results agreed with each other.

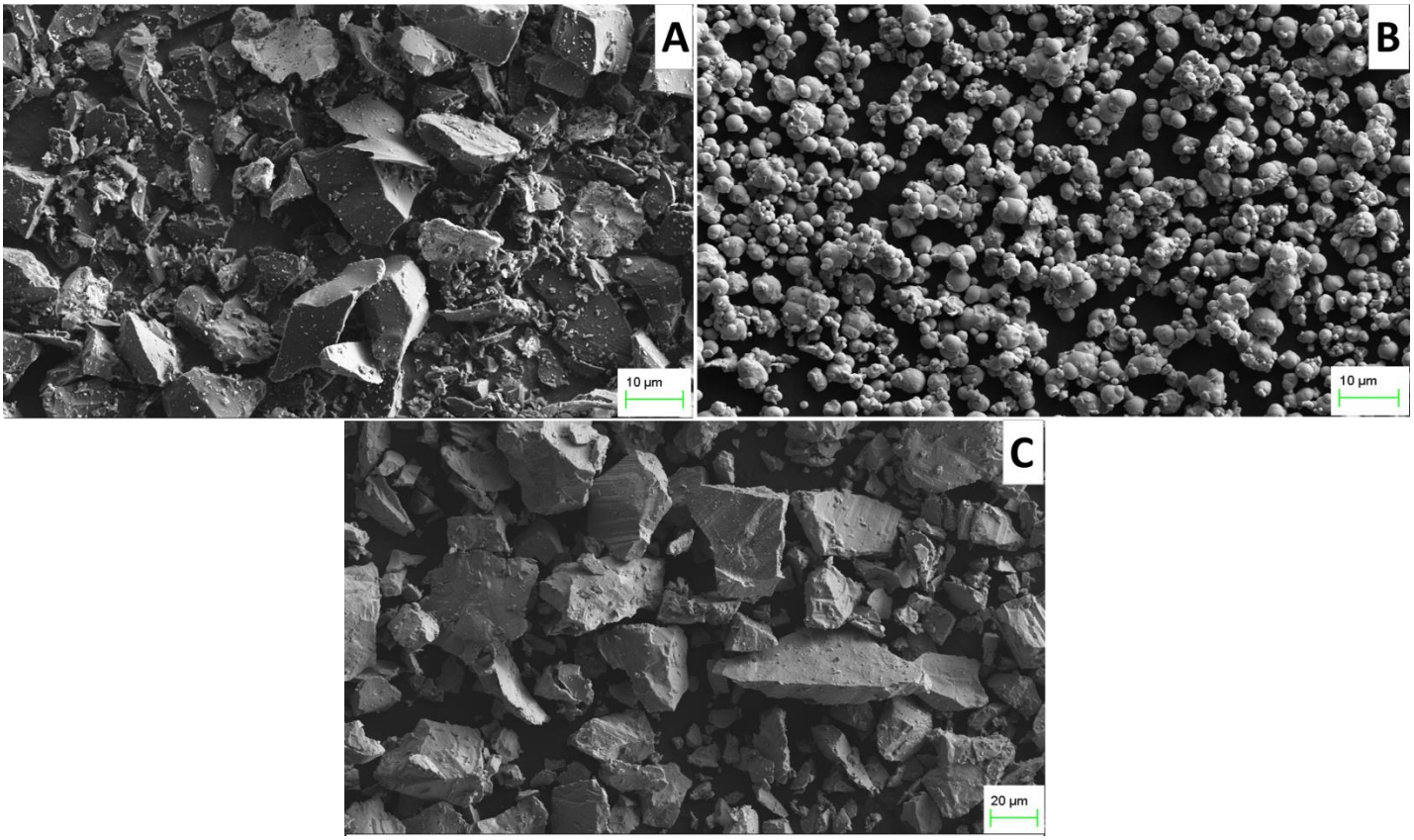


Figure 15: SE-SEM micrographs of as received A) B_4C powder, B) Fe powder and C) Ti powder.

4.1.2. X-Ray Diffraction

The phases present in the starting powders and their corresponding crystal structure were determined using XRD analysis. The X-ray diffraction patterns (Figure 16) of the starting powders showed the presence of α-Ti (HCP) (ICPF: 00-044-11294), α-Fe (BCC) (ICPF: 01-087-0721) and B_4C (rhombohedral) (ICPF: 00-035-0798) in the respective powders being used.

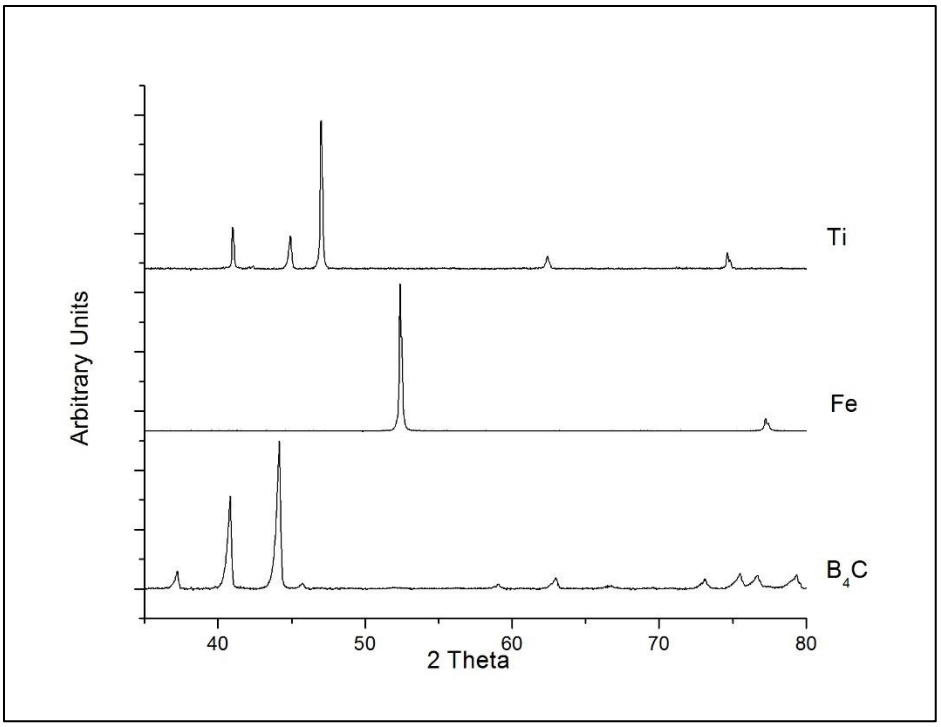


Figure 16: XRD analysis of the B_4C, Fe and Ti powders.

4.1.3. Composition changes during mixing

As per the experimental procedure, mass losses from the milling balls were recorded. The initial composition (Table 4) was adjusted accordingly and the mass and volume compositions are shown in Table 7. The mass losses from the steel milling balls, for compositions with additions ≥ 69.3 %, were in the range of 1.52 to 1.81 g.

Mixing B_4C with additives ≤ 8 vol. %, showed losses up to 3.13 g from the steel balls and 3.88 g from tungsten carbide balls, as shown in Table 7. Material losses from the milling balls decreased with increasing the starting additive composition to B_4C from 1 to 5 %. Additions of

Fe with Ti, and pure Ti saw smaller losses than their comparable Fe-B_4C compositions. WC milling balls were used with the pure Ti, for a comparison where no additional Fe was added to the system. The WC balls showed the biggest mass loss, however, the volume loss was comparable to Fe balls but still greater for like additions of 5 % to B_4C.

Thus, additions to B_4C of 5 vol. % or less, showed the Fe composition increased while the decrease in losses, from milling media, with increasing composition meant that the compositional differences of the mixed powders were reduced.

Table 7: Mass losses form the milling balls and the respective adjustments to composition for mixed powders.

Sample (Vol. %)	Mass Loss from milling balls (g)	Adjusted Composition (Wt. %)				Volume Loss from milling balls (cm^3)	Adjusted Composition (Vol. %)			
		B_4C	Fe	Ti	WC		B_4C	Fe	Ti	WC
1 % Fe-B_4C	3.13	87.49	12.51	-	-	0.41	95.49	4.51	-	-
3 % Fe-B_4C	1.95	85.63	14.37	-	-	0.26	94.76	5.24	-	-
5 % Fe-B_4C	0.61	84.20	15.80	-	-	0.08	94.17	5.83	-	-
69.3 % Fe-B_4C	1.64	12.11	87.89	-	-	0.21	30.14	69.86	-	-
78 % Fe-B_4C	1.76	8.07	91.93	-	-	0.23	21.57	78.43	-	-
80.9 % Fe-B_4C	1.81	6.85	93.15	-	-	0.24	18.72	81.28	-	-
1 % (0.8Fe+0.2Ti)-B_4C	2.50	89.44	10.23	0.32	-	0.33	96.18	3.63	0.20	-
3 % (0.8Fe+0.2Ti)-B_4C	1.56	87.31	11.72	0.97	-	0.20	95.20	4.21	0.59	-
5 % (0.8Fe+0.2Ti)-B_4C	0.49	85.54	12.84	1.61	-	0.06	94.33	4.67	1.00	-
69.3 % (0.8Fe+0.2Ti)-B_4C	1.52	13.09	76.31	10.60	-	0.20	30.18	56.19	13.63	-
78 % (0.8Fe+0.2Ti)-B_4C	1.63	8.76	80.10	11.14	-	0.21	21.60	63.08	15.32	-
80.9 % (0.8Fe+0.2Ti)-B_4C	1.66	7.44	81.25	11.30	-	0.22	18.75	65.37	15.88	-
1 % Ti-B_4C	2.38	90.68	7.68	1.64	-	0.31	96.33	2.69	0.98	-
3 % Ti-B_4C	1.48	90.14	4.86	5.00	-	0.19	95.34	1.70	2.96	-
5 % Ti-B_4C	0.47	89.95	1.56	8.49	-	0.06	94.47	0.54	4.99	-
5 % Ti-B_4C	3.88	80.75	-	7.62	11.62	0.25	92.93	-	4.91	2.16
8 % Ti-B_4C	3.62	77.24	-	12.04	10.71	0.23	90.12	-	7.87	2.02

4.2. Sintering and Characterisation of Iron Dominant Composites

4.2.1. Density, Hardness and Fracture Toughness

Composites with a high iron content, considered in this section, are those with compositions ≥ 69.3 vol. % Fe / (0.8Fe+0.2Ti) as shown in Table 4. The 69.3 and 78 vol. % Fe-B_4C compositions relate to mole ratios of 7 Fe:1 B_4C and 11 Fe:1 B_4C respectively. The selection of the compositions was guided by the potential reactions 3 and 4, while 80.9 vol. % Fe-B_4C corresponds to a mole ratio of 13.1 Fe:1 B_4C and was investigated to observe the effects where iron was in excess with regards to reaction 3.

$$11Fe + B_4C = 4Fe_2B + Fe_3C$$ Reaction 3

$$7Fe + B_4C = 4FeB + Fe_3C$$ Reaction 4

The results expressed in Table 8 include the density, fracture toughness and hardness results for the high Fe/low B_4C composition investigated. Sintering was carried out between 900 and 1100°C using heating rates of 50°C/min and cooling rates of 100°C/min in the SPS at 60 MPa pressure.

The density of each composite was determined using the Archimedes principle, however relative densities could not be determined using a theoretical density calculated from those of pure iron and boron carbide as the materials react during sintering. Densification was obtained through image analysis of the cross-section as per the experimental procedure (chapter 3.2.1).

The hardness and fracture values were obtained using the Vicker's indentation method on a polished surface as per the experimental procedure. Hardness values ranged from 6.4 to 14.4 GPa and fracture toughness values up to 5.9 $MPa.m^{0.5}$.

Table 8: Density, hardness and fracture toughness for low B_4C containing composites.

Sample	Temperature (°C)	Time (min)	Sintering Pressure (MPa)	Absolute Density (g/cm^3)	Relative Density (%)	Open Porosity (Vol. %)	Hardness – HV_5 (GPa)	Fracture Toughness ($MPa.m^{0.5}$)
80.9%Fe-B_4C	900	15	60	7.26	96.1±0.1	0.04	9.8±1.1	3.2±0.3
80.9%Fe-B_4C	1000	15	60	7.27	97.0±0.1	0.08	10.9±0.2	2.9±0.1
80.9%Fe-B_4C	1100	15	60	7.29	97.9±0.2	0.05	10.8±0.3	2.8±0.1
78%Fe-B_4C	900	15	60	7.23	96.0±0.7	0.05	12.9±0.2	3.1±0.1
78%Fe-B_4C	1000	15	60	7.25	96.3±0.5	0.05	13.2±0.1	3.2±0.1
78%Fe-B_4C	1100	15	60	7.27	97.1±0.2	0.04	11.9±0.1	2.9±0.4
69.3%Fe-B_4C	900	15	60	6.51	87.8±0.9	0.33	10.7±0.1	3.3±0.2
69.3%Fe-B_4C	1000	15	60	6.76	95.1±0.2	0.03	13.4±0.2	3.3±0.1
69.3%Fe-B_4C	1100	15	60	6.80	97.1±0.1	0.03	13.7±0.2	3.4±0.1
69.3%Fe-B_4C	1000	2	60	6.73	92.5±0.7	0.09	12.5±0.1	3.5±0.1
69.3%Fe-B_4C	1000	5	60	6.74	93.8±0.3	0.12	12.7±0.3	3.2±0.1
80.9%(0.8Fe+0.2Ti)-B_4C	900	15	60	6.70	95.9±0.2	0.21	8.1±0.1	5.9±0.1
80.9%(0.8Fe+0.2Ti)-B_4C	1000	15	60	6.87	97.5±0.1	0.09	7.8±0.2	3.6±0.1
80.9%(0.8Fe+0.2Ti)-B_4C	1100	15	60	6.90	98.3±0.4	0.09	6.4±0.1	4.9±0.4
78%(0.8Fe+0.2Ti)-B_4C	900	15	60	6.55	94.6±0.6	0.25	10.6±0.2	3.9±0.2
78%(0.8Fe+0.2Ti)-B_4C	1000	15	60	6.82	97.6±0.1	0.06	11.2±0.3	4.2±0.2
78%(0.8Fe+0.2Ti)-B_4C	1100	15	60	6.90	98.6±0.1	0.13	11.6±0.4	4.2±0.5
69.3%(0.8Fe+0.2Ti)-B_4C	900	15	60	5.81	92.7±0.6	1.89	8.9±0.2	3.8±0.3
69.3%(0.8Fe+0.2Ti)-B_4C	1000	15	60	6.04	96.1±0.5	1.12	9.8±0.6	3.6±0.1
69.3%(0.8Fe+0.2Ti)-B_4C	1100	15	60	6.20	97.2±0.2	0.14	14.4±0.5	4.0±0.1

4.2.2. Microstructure and Phase analysis

XRD and SEM analysis were used to observe the phases present and the microstructures of the composites produced. EDX analysis was used in conjunction with the SEM to identify the phases observed through XRD analysis within the respective SEM micrograph. Fe_2B, $Fe_3(B,C)$ and $Fe_{23}(B,C)$ were the main phases observed in the sintered composites.

4.2.2.1. 80.9 Vol. % Fe-B_4C

Figure 17 and Figure 18, respectively show the XRD and SEM results for the 80.9% Fe-B_4C composites produced at 900, 1000 and 1100°C. Fe_2B and $Fe_3(B,C)$ were identified in each composite through XRD analysis. Iron and $Fe_{23}(B,C)_6$ was present in composites sintered below 1100°C but not at 1100°C. The relative intensity of the Fe peak decreased with increasing temperature while the $Fe_3(B,C)$ increased.

The micrographs in Figure 18 show the evolution of the microstructure when sintering at 900, 1000 and 1100°C. Significant differences were observed with increasing temperature. Most notable was the presence of carbon and a fine dispersion of porosity at 900°C, the significant precipitation of $Fe_{23}(B,C)$ with a much finer dispersion of porosity whilst maintaining a fine grained structure at 1000°C and at 1100°C there was observable grain and pore growth whilst the $Fe_{23}(B,C)$ phase was no longer present.

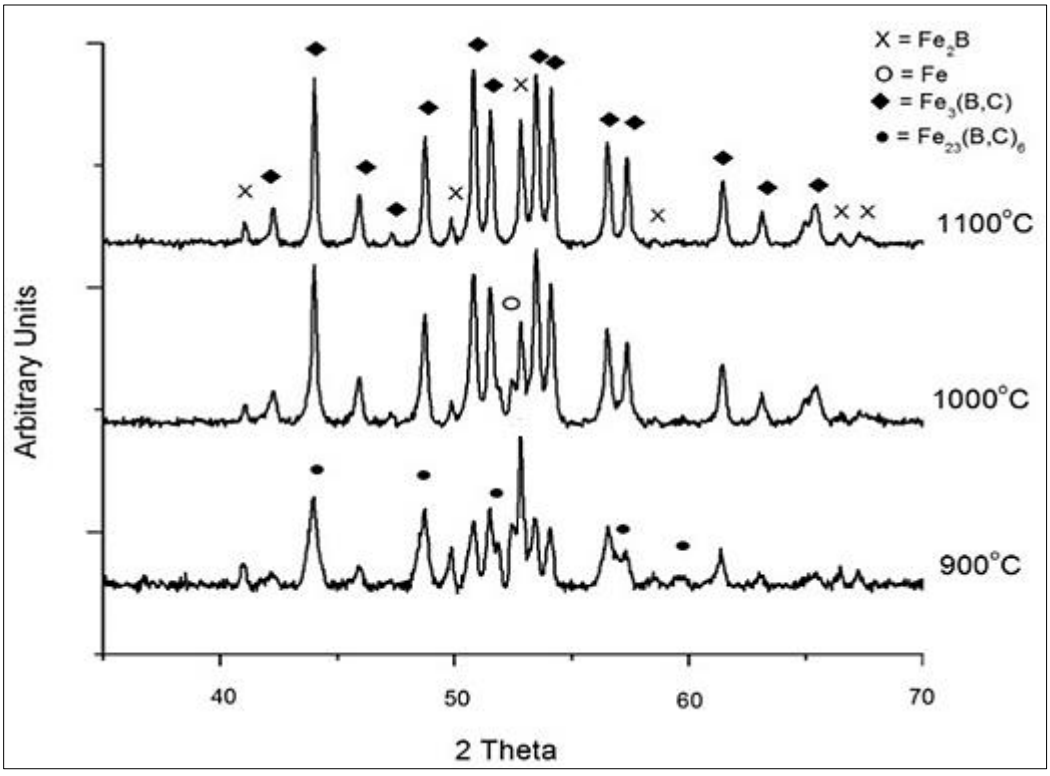


Figure 17: XRD analysis comparing the 80.9 vol. % Fe-B_4C composites sintered at 900, 1000 and 1100°C.

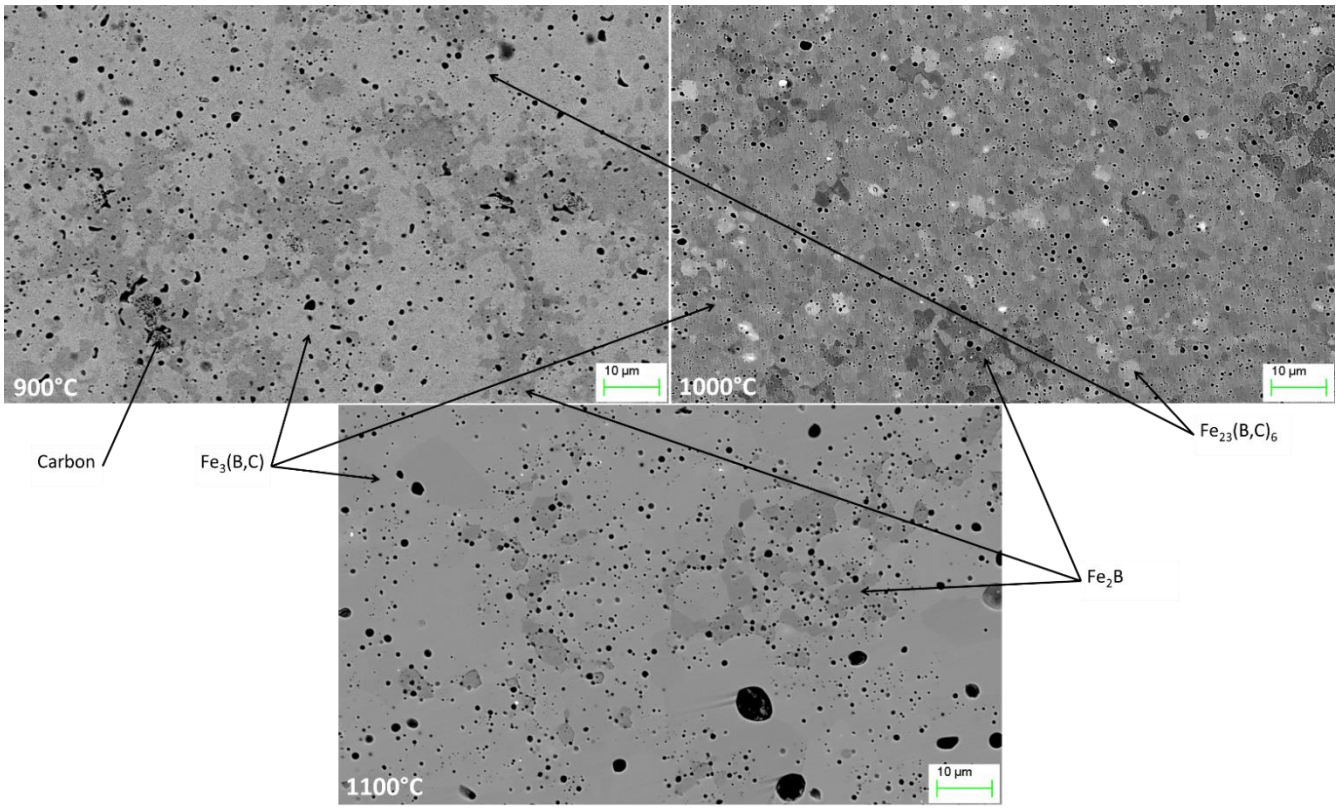


Figure 18: BS-SEM micrographs comparing microstructures of the 80.9 vol. % Fe-B_4C composites sintered at 900, 1000 and 1100°C.

The phases labelled in Figure 18 were identified from the phases determined in Figure 17 in conjunction with EDX analysis to differentiate between the phases. An example of the EDX analysis is shown in Figure 19 for 80.9 vol. % Fe-B_4C sintered at 1000°C and 60 MPa. The same technique was used to identify the phases in the remaining samples. The Fe present at 900 and 1000°C in 80.9% Fe-B_4C in Figure 17, could not be identified in Figure 18. Fe rich $Fe_{23}(B,C)_6$ was observed around the carbon phase in the 69.3 % Fe-B_4C (Figure 18 a) and as the lightest grey phase in the 78% Fe-B_4C (Figure 18 b). The bright white phase observed in the microstructures (most prevalent in Figure 18 b) was seen to be WC contamination from the mixing process.

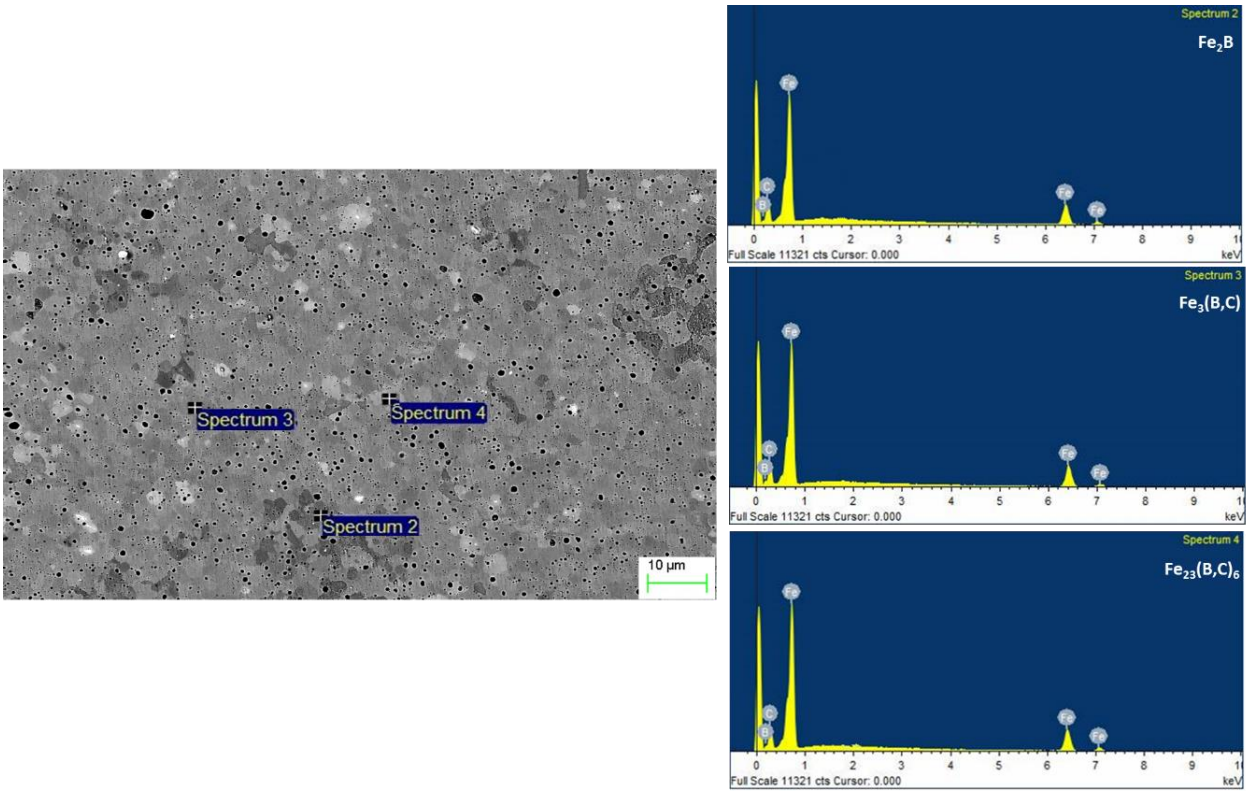


Figure 19: EDX analysis of the 80.9 vol. % Fe-B_4C composites sintered at 1000°C.

4.2.2.2. 78 Vol. % Fe-B_4C

XRD analysis on the 78% Fe-B_4C composites showed the presence of three phases. In Figure 20 it was observed that at 900 and 1000°C Fe_2B, $Fe_3(B,C)$ and $Fe_{23}(B,C)$ were present. The composite sintered at 1100°C showed no presence of the $Fe_{23}(B,C)$ phase while the Fe_2B and $Fe_3(B,C)$ were observed. Although a clear iron phase was not observed, broadening at the base of the major Fe_2B peak (≈ 52.5° 2Theta) suggests a small amount of iron may be present.

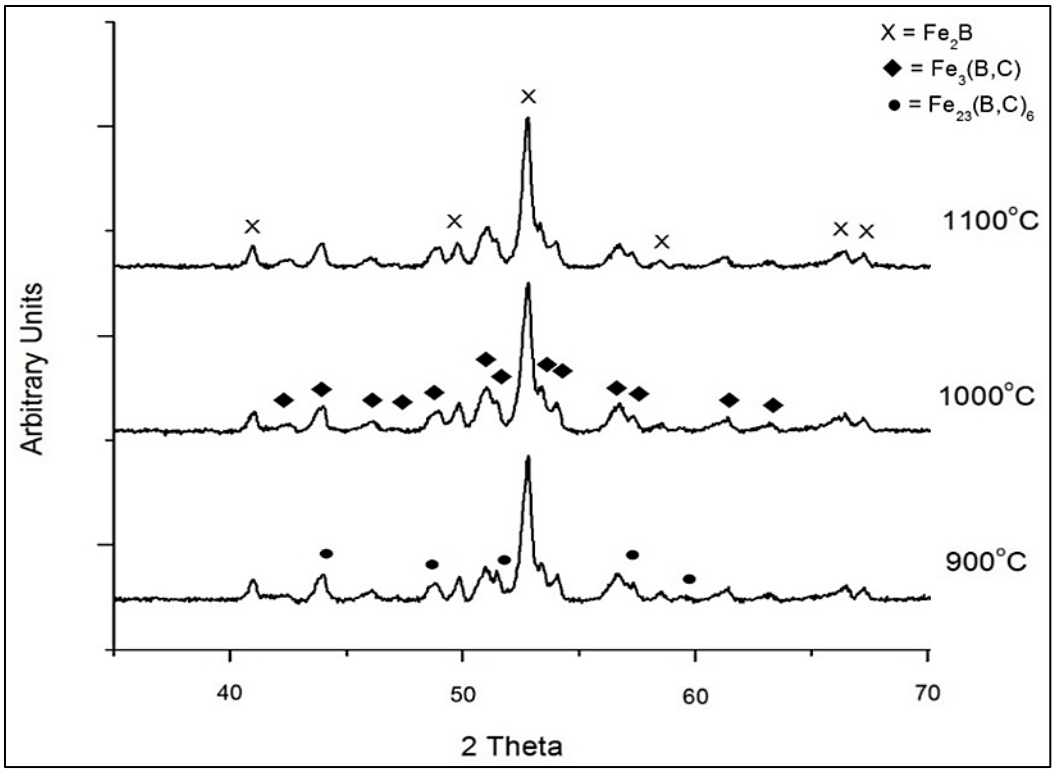


Figure 20: XRD analysis comparing the 78 vol. % Fe-B_4C composites sintered at 900, 1000 and 1100°C.

Although the XRD analysis suggested $Fe_{23}(B,C)$ was no longer present when sintering at 1100°C, SEM images of the composite (Figure 21) revealed very small amounts of the phase were still present. Free carbon was observed in each of the composites with decreasing quantities as sintering temperature increased. A very fine dispersion of porosity was observed at 1000°C, increasing temperature to 1100°C again showed porosity growth. Some WC contamination was again identified as the bright white phase in Figure 21.

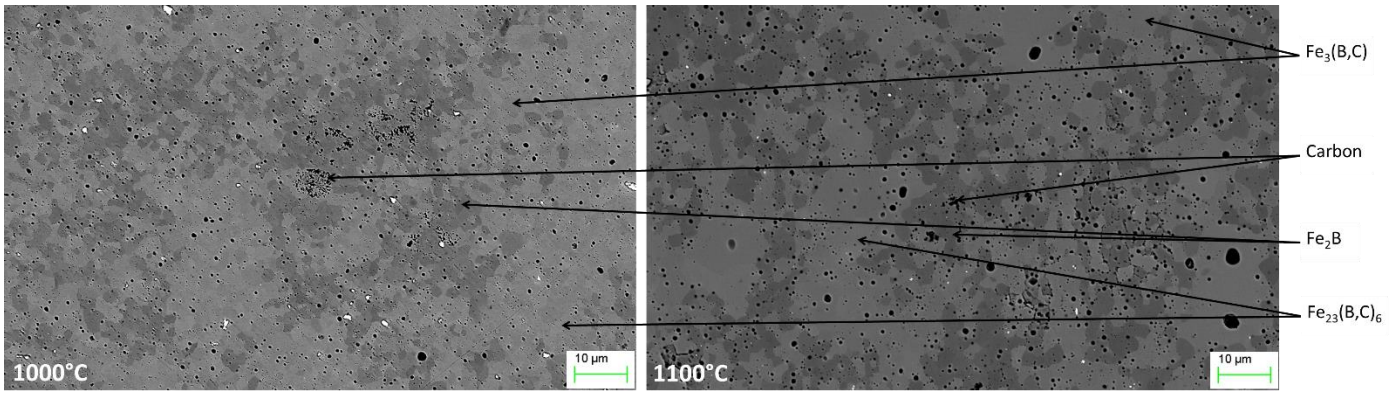


Figure 21: BS-SEM micrographs showing microstructures of the 78 vol. % Fe-B_4C composites sintered at 1000 and 1100°C.

4.2.2.3. 69.3 Vol. % Fe-B_4C

When the iron concentration was lowered to 69.3 vol. %, Fe_2B and $Fe_3(B,C)$ phases were observed while the $Fe_3(B,C)_6$ phase was not detected. XRD analysis showed Fe_2B to be the predominant phase with small amounts of $Fe_3(B,C)$ present throughout the temperature range. The XRD patterns in Figure 22 suggest the presence of the $Fe_3(B,C)$ phase was most prevalent at 1000°C.

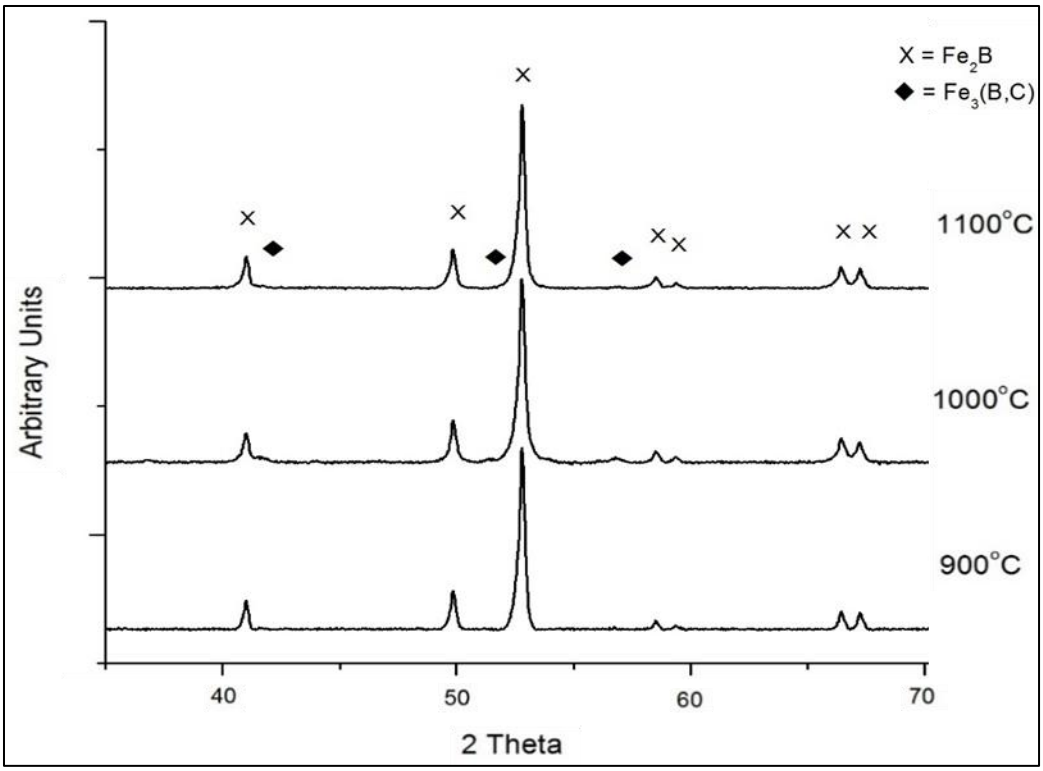


Figure 22: XRD analysis comparing the 69.3 vol. % Fe-B_4C composites sintered at 900, 1000 and 1100°C.

The microstructures in Figure 23 showed evidence of unreacted carbon dispersed throughout each of the sintered composites. There was once again the presence of fine porosity in each of the composites; this appeared to get smaller when the temperature increased to 1000°C from 900°C with a further increase to 1100°C resulting in apparent pore growth. When comparing the phases observed (Figure 22) to the microstructures in Figure 23, it was evident that although Fe_2B was the major phase present in the matrix, a significant amount of the $Fe_3(B,C)$ phase was also present. Using image analysis to quantify the phases present, $Fe_3(B,C)$ appeared to decrease with increasing temperature from ≈ 20 vol. % at 900°C to ≈ 10 vol. % at 1100°C. The phases were identified using EDX analysis, which also suggested the presence of a fine dispersion of FeB through carbon rich areas as shown in Figure 24. These areas are indicative of B_4C grains where Fe and B have reacted to form FeB and C, where the C migrates to the grain boundaries. Figure 24 shows the bright phase dispersed throughout the microstructures to be WC contamination from the mixing process.

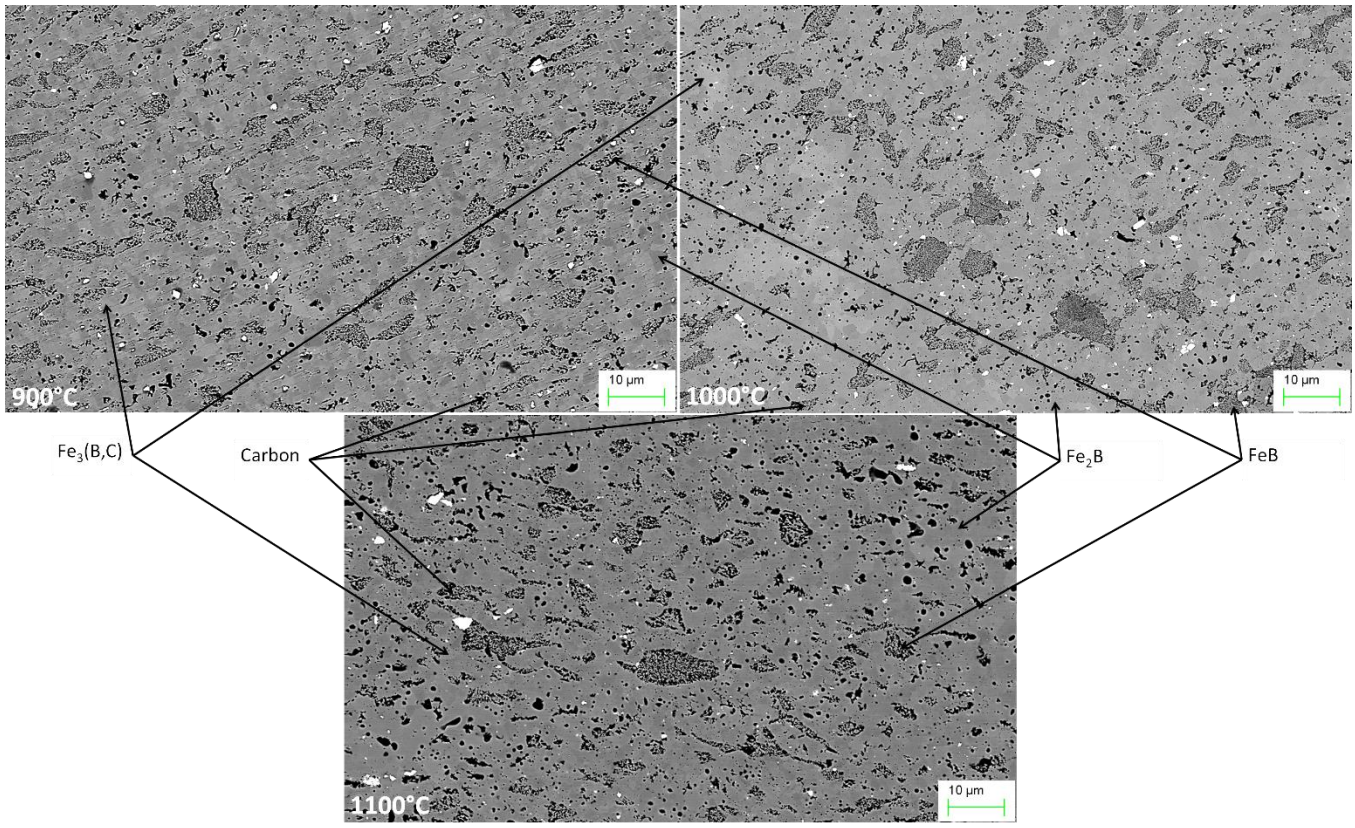


Figure 23: BS-SEM micrographs of the 69.3 vol. % Fe-B_4C composites sintered at 900, 1000 and 1100°C.

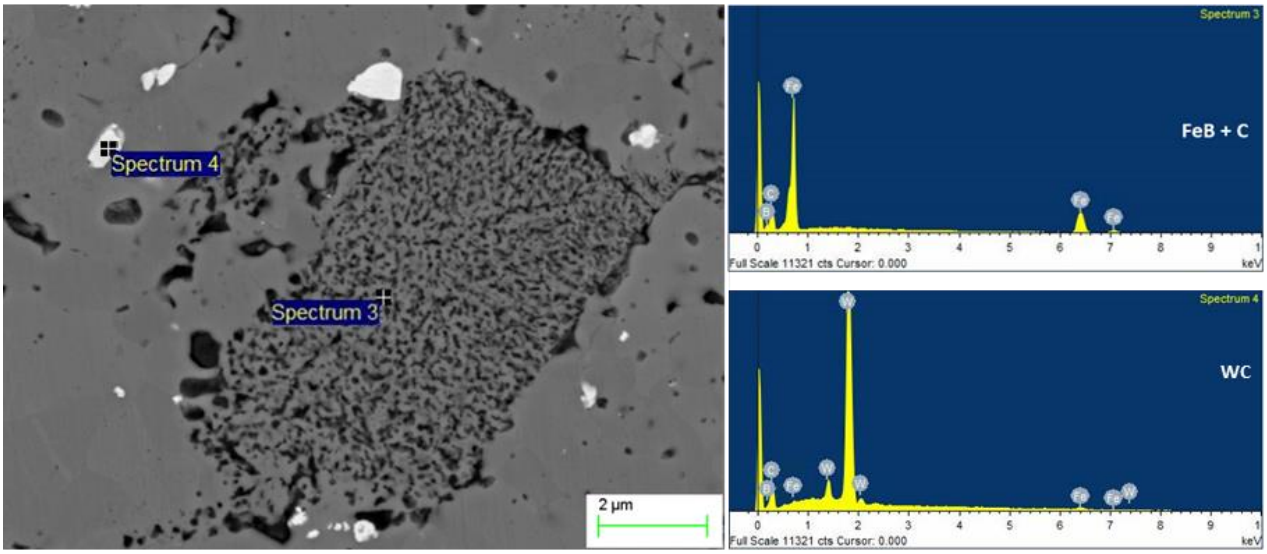


Figure 24: EDX analysis with focus on dark grey phase dispersed through carbon rich areas and bright WC phase in 69.3 vol. % Fe-B_4C composite sintered at 1000°C and 60 MPa.

4.2.2.4. Addition of Ti to Fe-B_4C

To minimize residual carbon produced in the 69.3-80.9 vol. % Fe-B_4C composites, 20 vol. % of the iron was replaced with titanium. As with the respective Fe-B_4C composites, XRD analysis showed Fe_2B, $Fe_3(B,C)$ and $Fe_{23}(B,C)$ were again the major phases produced. This is evident in Figure 25 where it is also apparent that the 78 and 80.9 % (0.8Fe+0.2Ti)-B_4C samples contained unreacted iron while TiC was detected in each of the composites, due to the addition of Ti.

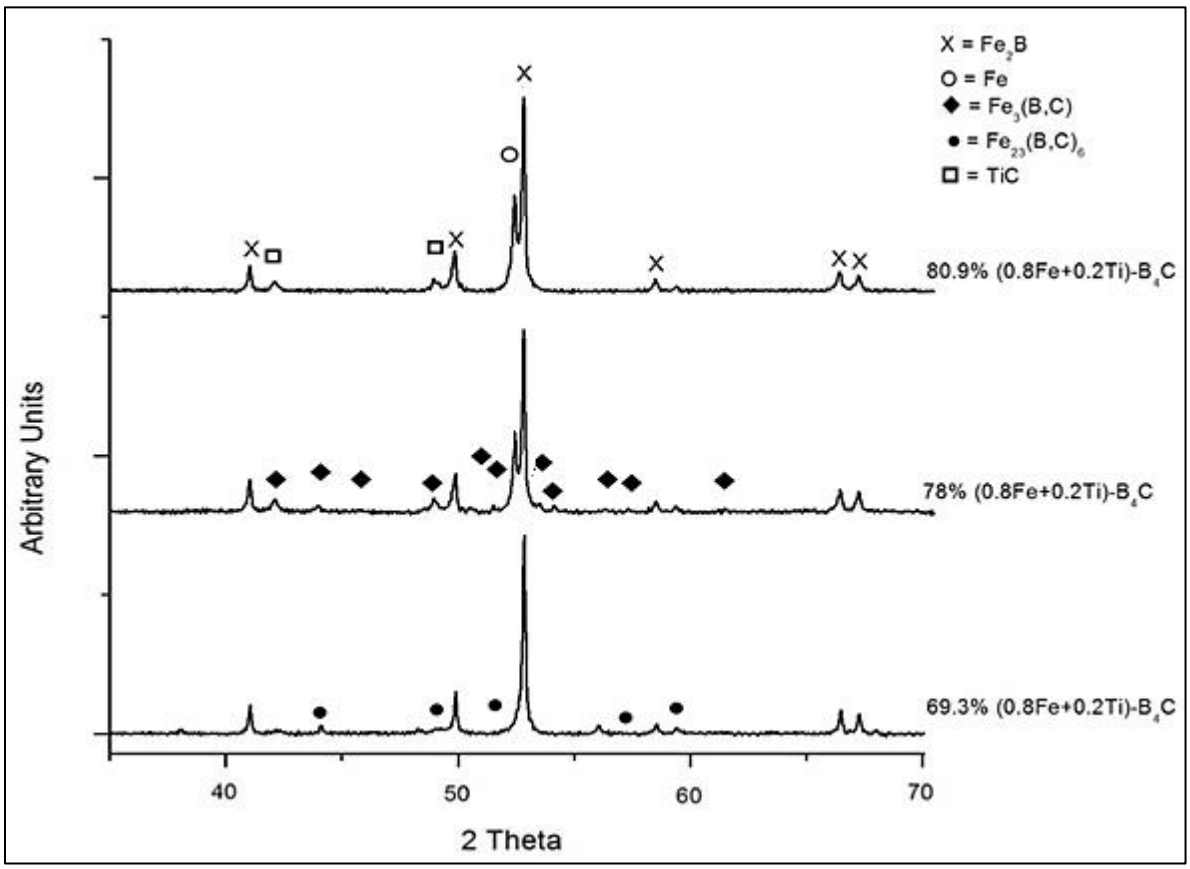


Figure 25: XRD analysis comparing the 69.3 vol. %, 78 vol. % and 80.9 vol. % (0.8 Fe+0.2Ti)-B_4C composites sintered at 1000°C and 60 MPa.

SEM analysis of the composites sintered at 1000°C showed significant changes in microstructure with increasing the (0.8Fe+0.2Ti) concentration, as seen in Figure 26. The total porosity appears

to decrease with increasing the concentration from 69.3 to 80.9 % (0.8Fe+0.2Ti)-B_4C however, the size of the pores appeared to decrease when moving from 69.3 to 78% and showed signs of pore growth when increasing concentration from 78 to 80.9 % (0.8Fe+0.2Ti). The TiC phases observed in were most prominent in large elongated areas; this is a result of the larger Ti powder particle size with respect to the Fe and B_4C powders. Similar carbon rich structures were observed in Figure 26 a) to those in Figure 23 for 69.3 vol. % Fe-B_4C. B_4C grains reacted to form a carbon rich structure, with C dispersed at the grain boundaries of a $(Fe,Ti)_X(B,C)_Y$ phase for the 69.3% (0.8Fe+0.2Ti)-B_4C in Figure 26 a), differing from the Fe only addition where the carbon was dispersed through a FeB phase (Figure 24). The effect is exaggerated in this case as areas of completely un-bonded grains and significant cracking are evident along with the porous structure around the carbon rich areas. While iron rich areas were observed using EDX analysis, pure Fe observed in Figure 25, for 78 and 80.9% (0.8Fe+0.2Ti)-B_4C, could not be clearly identified in Figure 26 b) and c). The bright (white) phase present in Figure 26 was WC contamination from mixing.

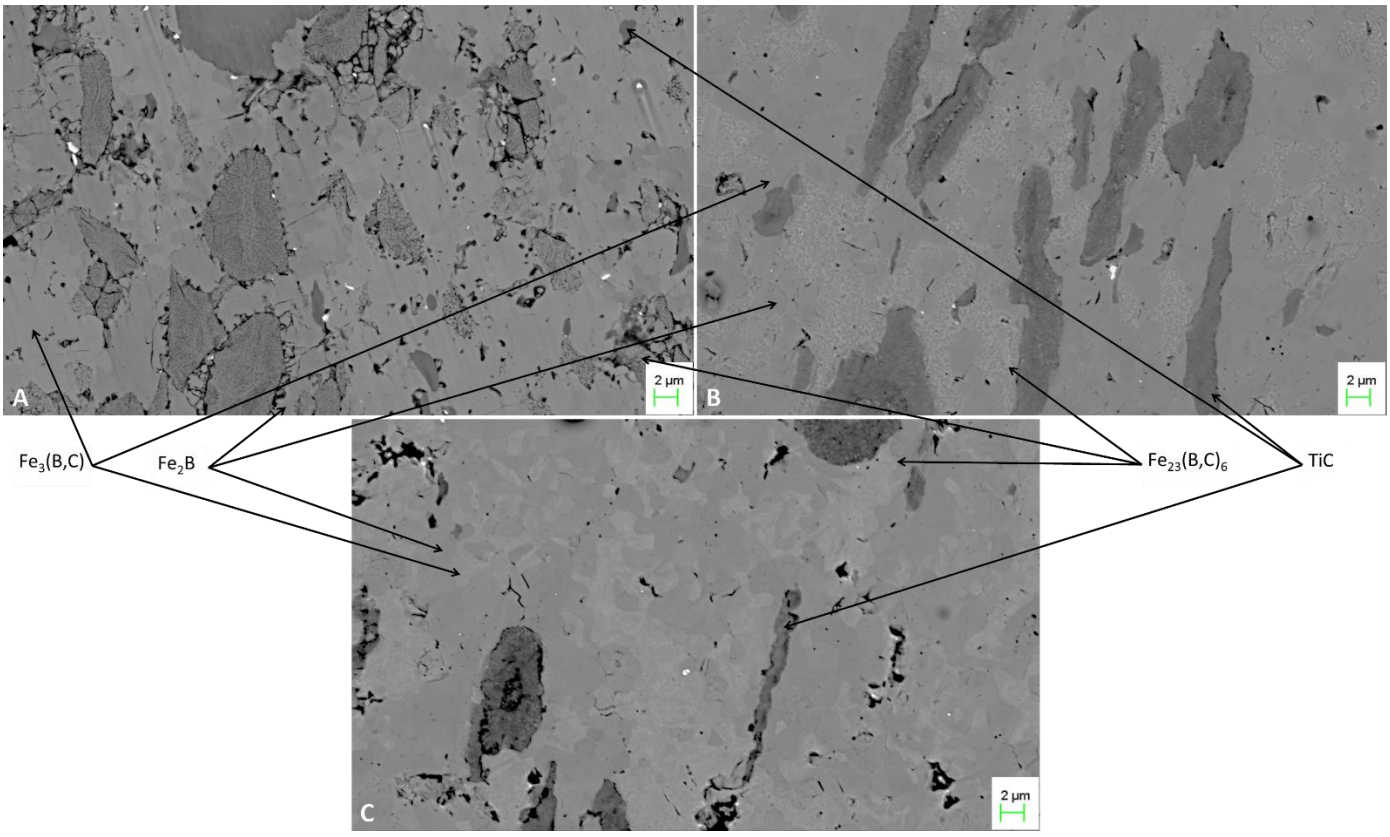


Figure 26: BS-SEM micrographs showing the microstructures of a) 69.3, b) 78 and c) 80.9 vol. % (0.8Fe+0.2Ti)-B_4C composites sintered at 1000°C and 60MPa.

XRD analysis (Figure 25) did not suggest the presence of a titanium boride phase, however EDX observations, as in Figure 27, showed the darker region within the TiC phase to be boron, carbon and titanium rich. Both the light and the dark regions showed the presence of a small quantity of iron in solution as well.

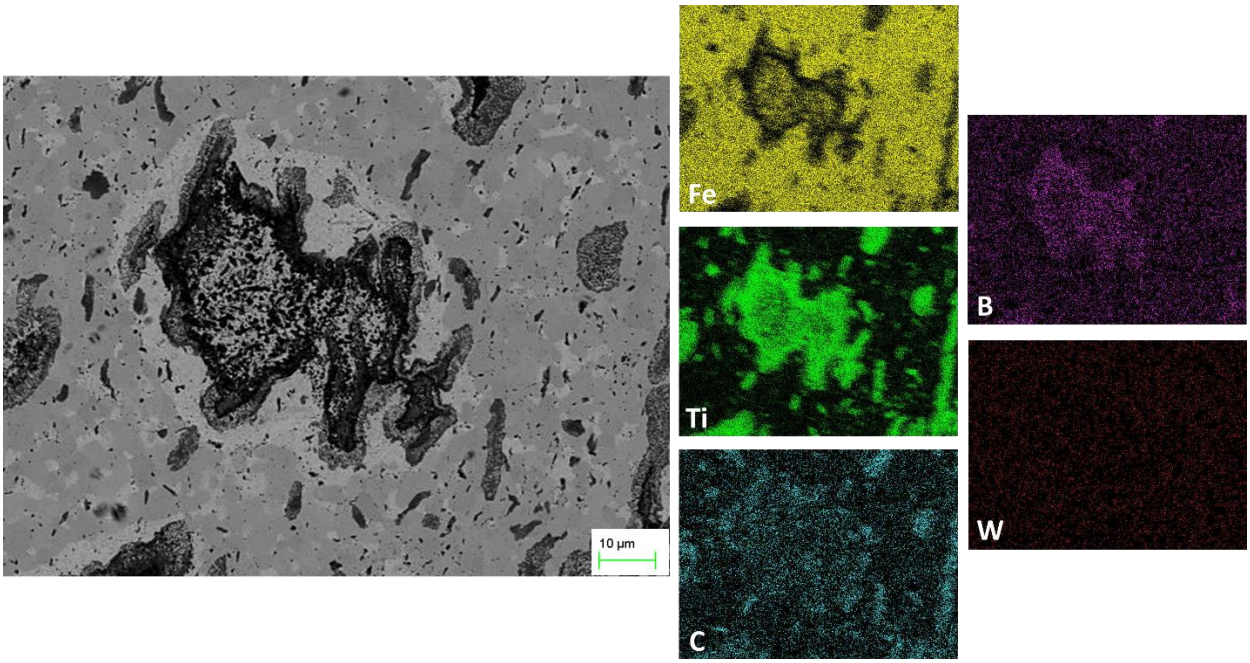


Figure 27: EDX mapping of Ti rich phase in the microstructure of the 69.3 vol. % (0.8Fe+0.2Ti)-B_4C composite sintered at 1100°C and 60MPa.

4.3. Sintering and Characterisation of B_4C Dominant Composites

4.3.1. Density, Hardness and Fracture Toughness

Boron carbide with additions of iron and titanium up to 5 vol. % were investigated and the density, hardness and fracture toughness of the materials produced are reported in Table 9. Once again the density dependence on phases produced as a result of Fe-B_4C interactions meant the calculated relative density relied on image analysis of the cross sections to determine the degree of porosity and hence densification.

A temperature range of 1910-2000°C with pressures of 30-70 MPa was implemented during sintering. Sintering temperature was limited to 2000°C at 30 MPa as higher temperatures and pressures resulted in significant loss of liquid phase formed. This was observed with the 5 vol % Fe-B_4C composite sintered at 2000°C and 70 MPa, as expressed in Table 9, where over 99%

densification was observed (analysis of the cross section) even though the absolute density decreased with the resultant loss of the iron rich liquid phase.

Table 9: Density, hardness and fracture toughness for composites with a high B_4C content.

Sample	Temperature (°C)	Time (min)	Sintering Pressure (MPa)	Absolute Density (g/cm^3)	Relative Density (%)	Open Porosity (Vol. %)	Hardness – HV_5 (GPa)	Fracture Toughness ($MPa.m^{0.5}$)
5%Fe-B_4C	1900	15	70	2.71	95.4±0.5	0.12	19.1±0.8	4.6±0.2
5%Fe-B_4C	1910	15	70	2.72	96.3±0.3	0.04	20.7±2.0	4.5±0.3
5%Fe-B_4C	2000	2	30	2.79	98.4±0.2	0.02	31.4±0.6	4.7±0.1
5%Fe-B_4C	2000	2	70	2.60	99.4±0.2	0.01	32.4±0.7	4.7±0.2
3%Fe-B_4C	1900	15	70	2.61	91.2±0.7	2.96	12.9±1.6	3.9±0.2
3%Fe-B_4C	1910	15	70	2.71	96.3±0.2	0.06	19.3±0.8	4.2±0.3
3%Fe-B_4C	2000	2	30	2.74	97.6±0.4	0.02	32.6±0.5	5.0±0.1
1%Fe-B_4C	1910	15	70	2.58	92.7±0.4	0.21	19.5±0.3	4.0±0.2
1%Fe-B_4C	2000	2	30	2.73	97.7±0.5	0.05	33.1±0.7	5.3±0.2
5%(0.8Fe+0.2Ti)-B_4C	1910	15	70	2.66	95.5±0.5	0.28	20.8±2.4	4.9±0.7
5%(0.8Fe+0.2Ti)-B_4C	2000	2	30	2.74	97.9±0.3	0.11	29.4±0.8	5.0±0.1
3%(0.8Fe+0.2Ti)-B_4C	1910	15	70	2.71	96.9±0.2	0.14	20.9±1.8	5.6±0.1
3%(0.8Fe+0.2Ti)-B_4C	2000	2	30	2.73	97.4±0.2	0.08	27.8±1.4	5.0±0.2
1%(0.8Fe+0.2Ti)-B_4C	1910	15	70	2.67	95.9±0.6	0.27	20.1±0.9	4.9±0.1
1%(0.8Fe+0.2Ti)-B_4C	2000	2	30	2.70	97.6±0.2	0.21	34.6±0.4	5.3±0.1
5%Ti-B_4C (Fe Balls)	1910	15	70	2.53	94.8±0.2	2.47	17.5±0.2	4.5±0.1
5%Ti-B_4C (Fe Balls)	2000	2	30	2.54	95.1±1.0	1.17	21.7±0.8	4.9±0.3
3%Ti-B_4C (Fe Balls)	1910	15	70	2.48	92.9±0.1	3.86	17.8±0.4	3.9±0.1
3%Ti-B_4C (Fe Balls)	2000	2	30	2.59	95.6±0.2	1.26	14.8±0.3	3.8±0.1
1%Ti-B_4C (Fe Balls)	1910	15	70	2.53	92.3±0.4	3.51	20.2±1.0	4.3±0.1
1%Ti-B_4C (Fe Balls)	2000	2	70	2.68	96.9±0.1	0.18	21.8±0.5	4.3±0.1
5%Ti-B_4C (WC Balls)	1910	15	70	2.87	95.2±0.2	0.22	20.8±0.3	4.2±0.1
5%Ti-B_4C (WC Balls)	2000	2	30	2.93	97.2±0.5	0.05	27.1±0.8	5.1±0.1
8%Ti-B_4C (WC Balls)	1910	15	70	2.91	95.2±0.2	0.27	20.9±0.7	4.9±0.6
8%Ti-B_4C (WC Balls)	2000	2	30	2.96	96.7±0.3	0.11	20.2±0.6	4.1±0.2

It must be noted that reproducibility of the hardness values was poor and depended heavily on the polishing of the material and the extent to which pull out of the FeB phase occurred. 1 and 3 % Fe-B_4C samples sintered at 2000°C were sent to Fraunhofer Institute for Ceramic Technologies and Systems (Germany) for evaluation, where the high hardness attained could not be confirmed.

4.3.2. Microstructure and Phase analysis

4.3.2.1. Fe additions to B_4C

Figure 28 shows the phases observed through XRD analysis for composites produced with additions of 1, 3 and 5 % iron to boron carbide. The phases observed were FeB and B_4C; these phases were identified within the microstructure (Figure 29) using SEM with EDX analysis. When observing the FeB phase in Figure 29, it was seen that there were inclusions present within the FeB. These were very small quantities, and seen to mainly consist of WC due to contamination during the milling process (Figure 30). The FeB phase was also seen to contain several areas with cracks; this in conjunction with the shape of the pores suggests that there is pull-out of these grains during grinding and polishing.

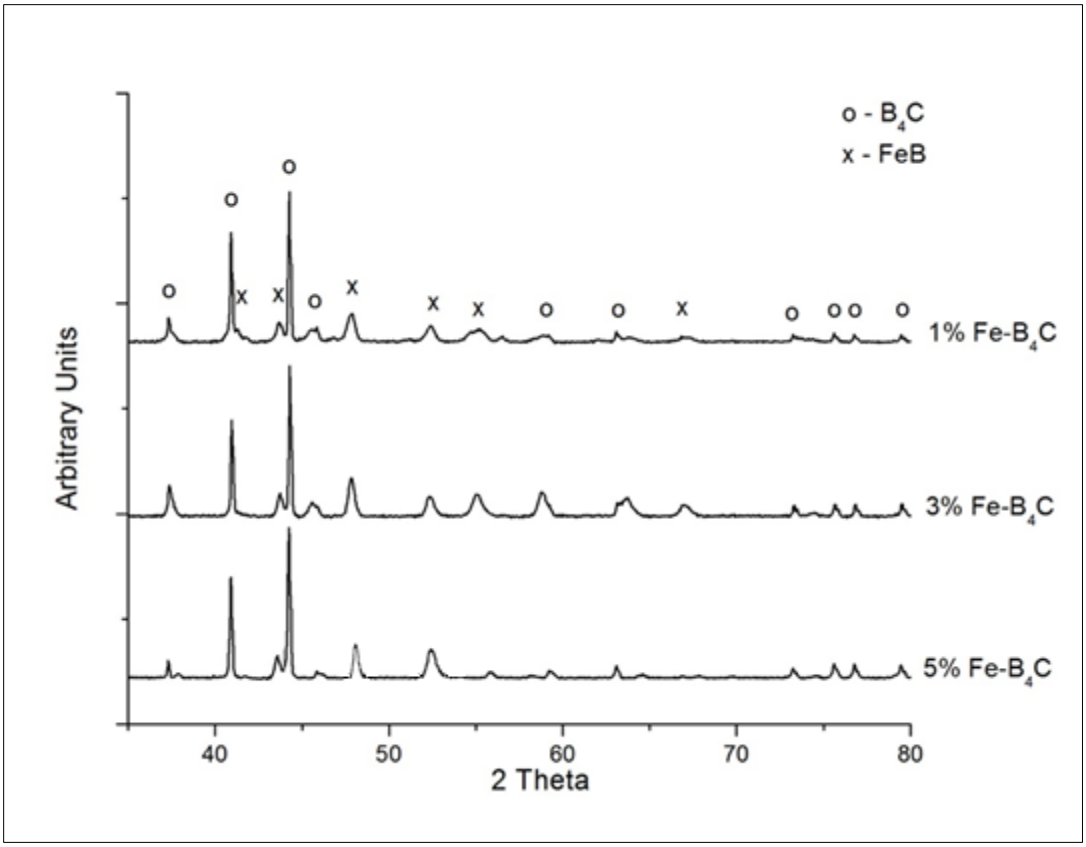


Figure 28: XRD analysis comparing the 5 vol% Fe-B_4C, 3 vol% Fe-B_4C and 1 vol% Fe-B_4C composites sintered at 2000°C and 30MPa.

When observing the microstructures of the materials in Figure 29, the amount of FeB present was nearly the same for each of the compositions. This was due to iron contamination during milling as was shown in Table 7. As a result, the actual range of the Fe additions to B_4C was only 4.51 to 5.83 vol. %, as opposed to 1 – 5 % as the powders were prepared.

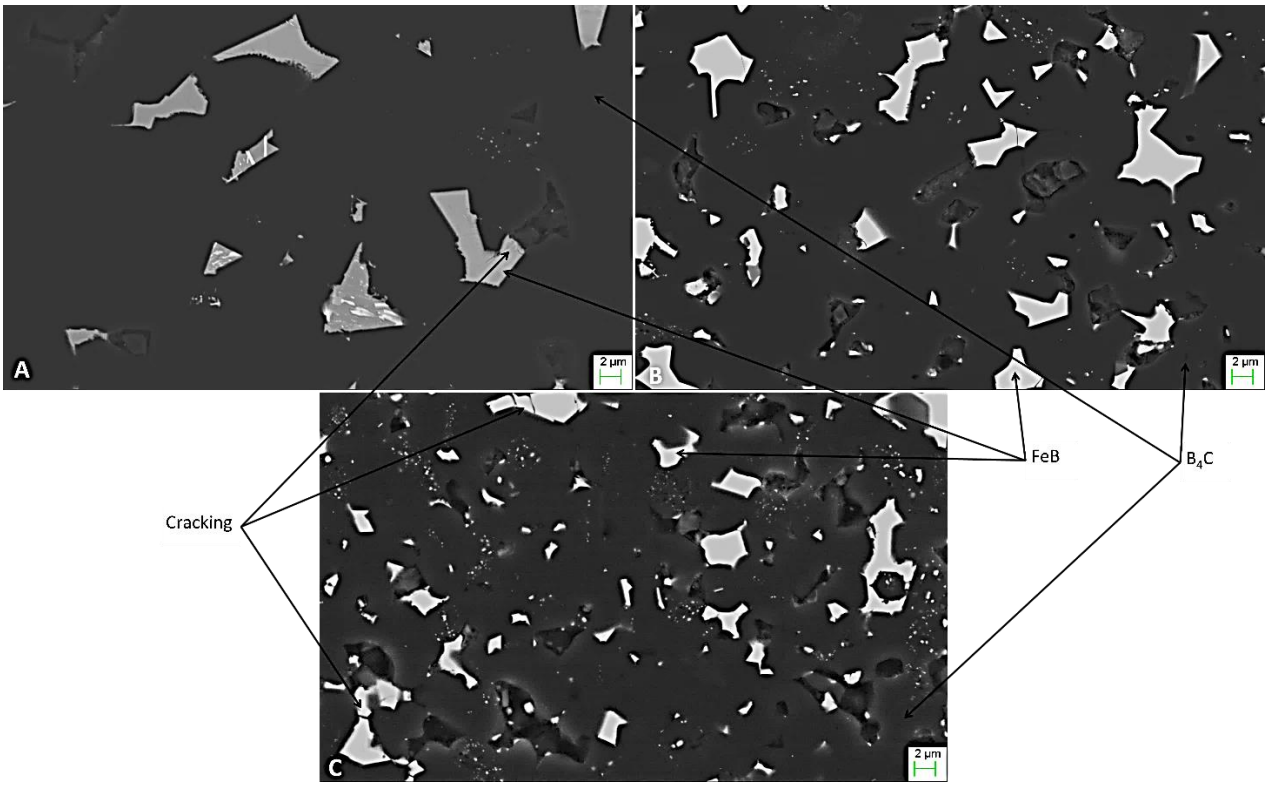


Figure 29: BS-SEM micrographs showing the microstructures of the a) 1 vol% Fe-B_4C, b) 3 vol% Fe-B_4C and c) 5 vol% Fe-B_4C composites sintered at 2000°C and 30MPa.

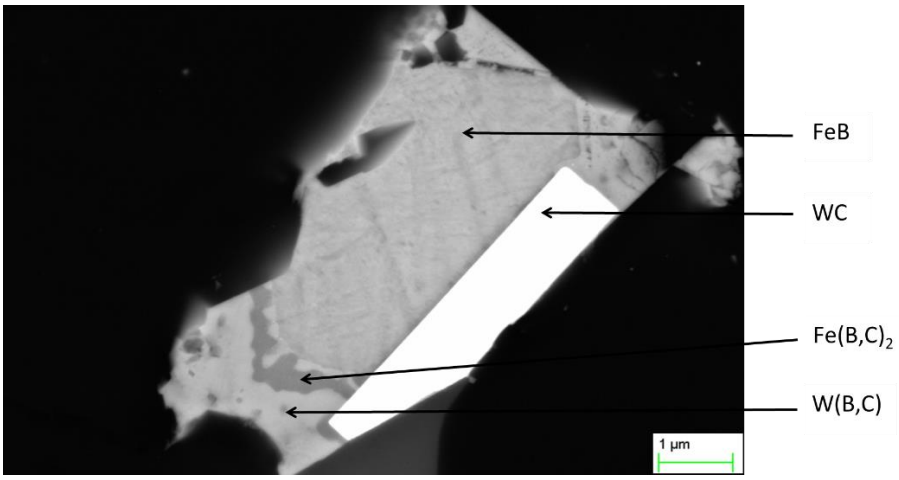


Figure 30: BS-SEM micrograph showing inclusions within FeB phase in 1 vol% Fe-B_4C sintered at 2000°C and 30MPa, identified using EDX analysis. 1 vol% Fe-B_4C

4.3.2.2. Fe and Ti additions to B_4C

20 vol. % of the iron was again replaced with titanium in order to observe the effects this had on the properties of the material and whether this would aid in the prevention of the cracking in the FeB phase observed in Figure 29. The addition to B_4C of the (0.8Fe+0.2Ti) mix was kept constant at 1, 3 and 5%. XRD analysis (Figure 31) showed the main constituents of the composites to be B_4C and FeB, however, the addition of Ti was responsible for the presence of an additional TiB_2 phase within each sintered sample.

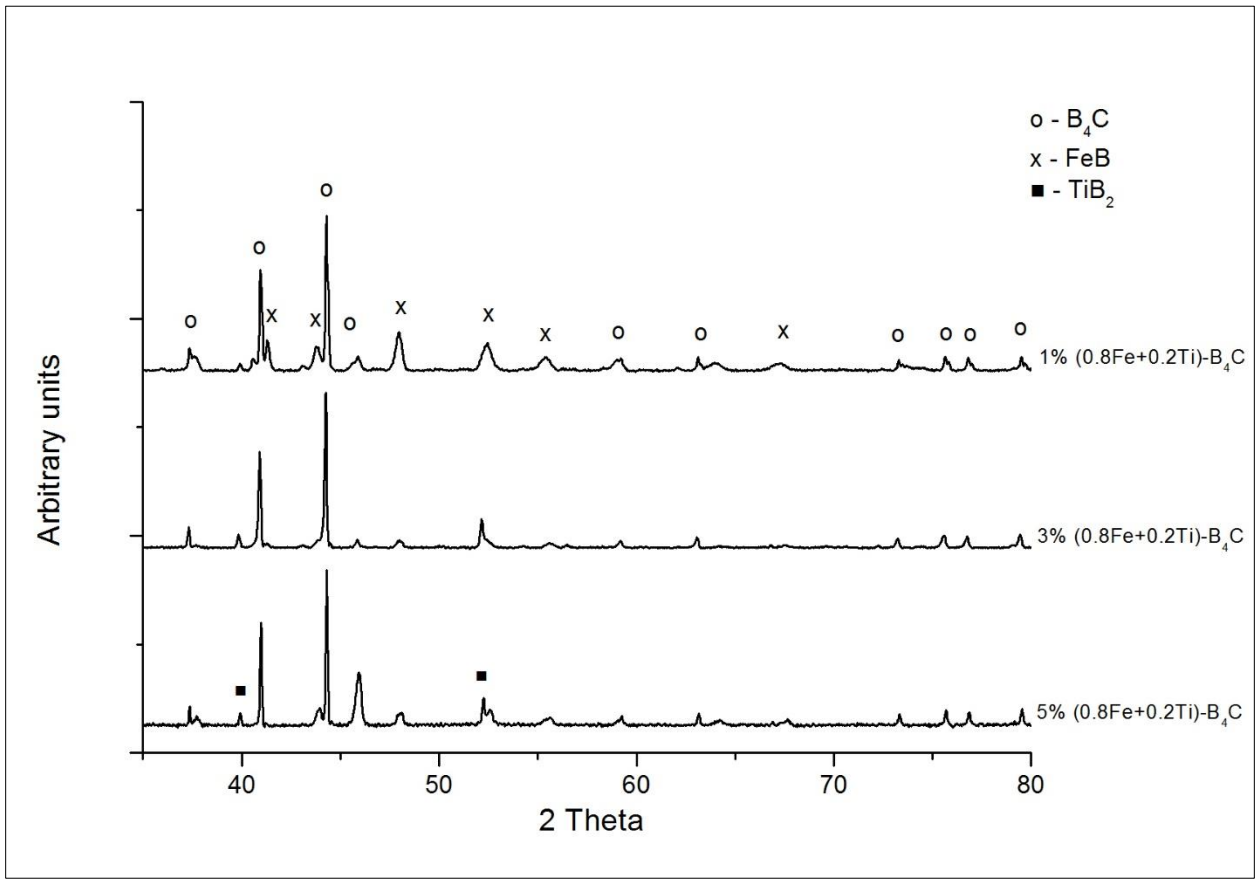


Figure 31: XRD analysis of the 1, 3 and 5 vol% (0.8Fe+0.2Ti)-B_4C composites sintered at 2000°C and 30MPa.

The micrographs depicting the microstructure of the composites in Figure 32 showed significant differences compared to those in Figure 29. WC contamination was again identified and was more prominent in the 1 and 5 % additions. Cracking within this phase was also seen to increase with the additions of Ti. The additional presence of the TiB_2 phase within the region did not improve the microstructure, and it was evident that areas where these phases were present, were more than double the size of those in Figure 29. The dispersion of the additional phases through the B_4C was good, although it was clear that the TiB_2 was not present in isolation, rather in pools of FeB, TiB_2 and WC. There is again presence of grain pull-out in Figure 32, as was the case with the Fe-B_4C composites in Figure 29.

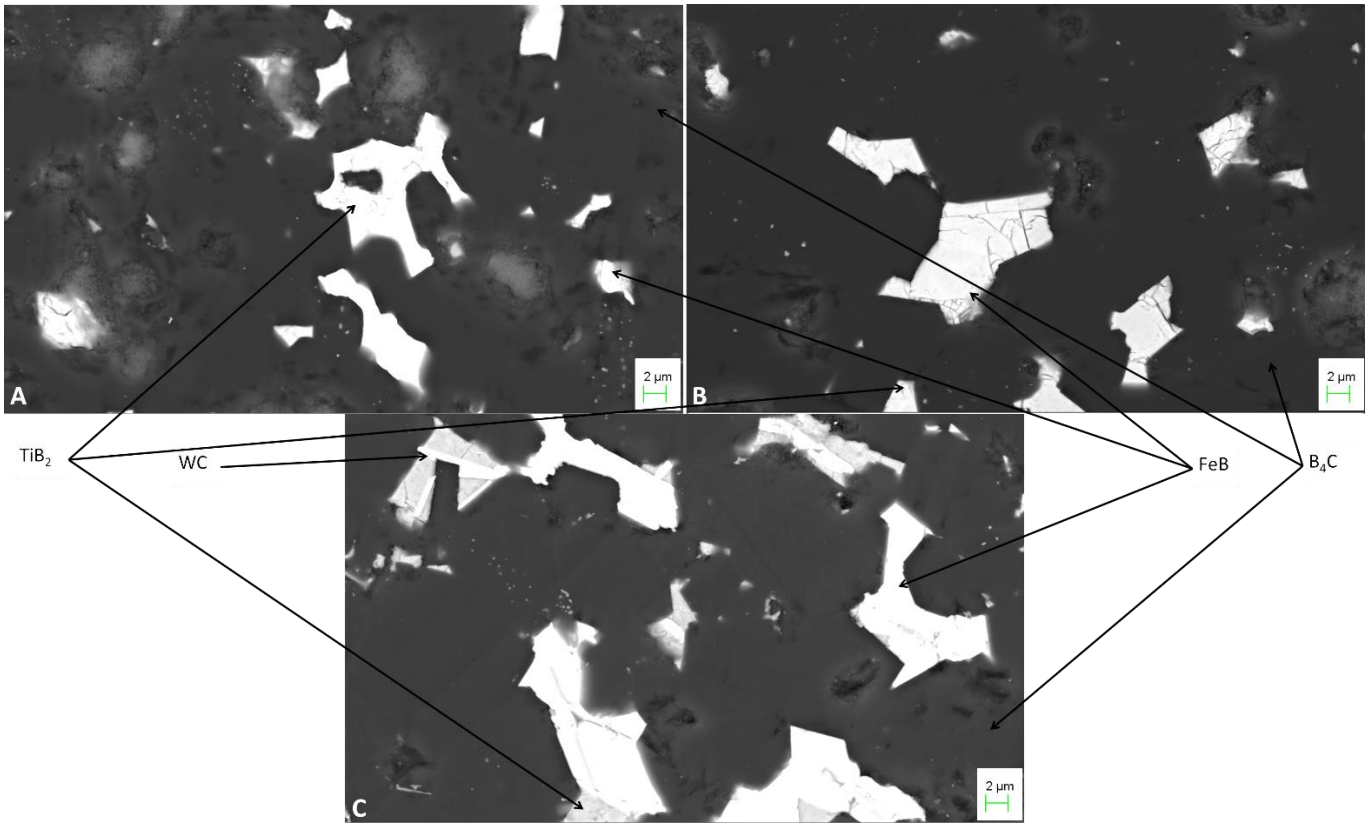


Figure 32: BS-SEM micrographs depicting the microstructures of the A) 1 vol%, B) 3 and C) 5 vol% (0.8Fe+0.2Ti)-B4C composites sintered at 2000°C and 30MPa.

4.3.2.3. Ti additions to B_4C

To observe the effectiveness of using iron as an additive, with respect to more common additives used with B_4C, Ti additions under the same conditions were used for comparison. To observe the extent to which iron contamination from milling media influenced the results, two batches of Ti-B_4C composites were sintered; those with steel milling media as with the Fe-B_4C composites and with WC milling media to prevent Fe contamination. XRD analysis in Figure 33 showed the presence of B_4C and TiB_2 in the composites prepared with Fe and WC milling media. The use of Fe milling media resulted in a significant FeB peak being observed as a result of iron contamination. Conversely, the use of WC milling media showed a significant increase in tungsten contamination with tungsten boride phases present in Figure 33. It was evident from SEM analysis of the microstructures observed in Figure 34 that the use of Ti where Fe was not present (Figure 34 A) did not show signs of excessive grain pull-out while iron contamination in (Figure 34 B) saw an increase in apparent pull-out.

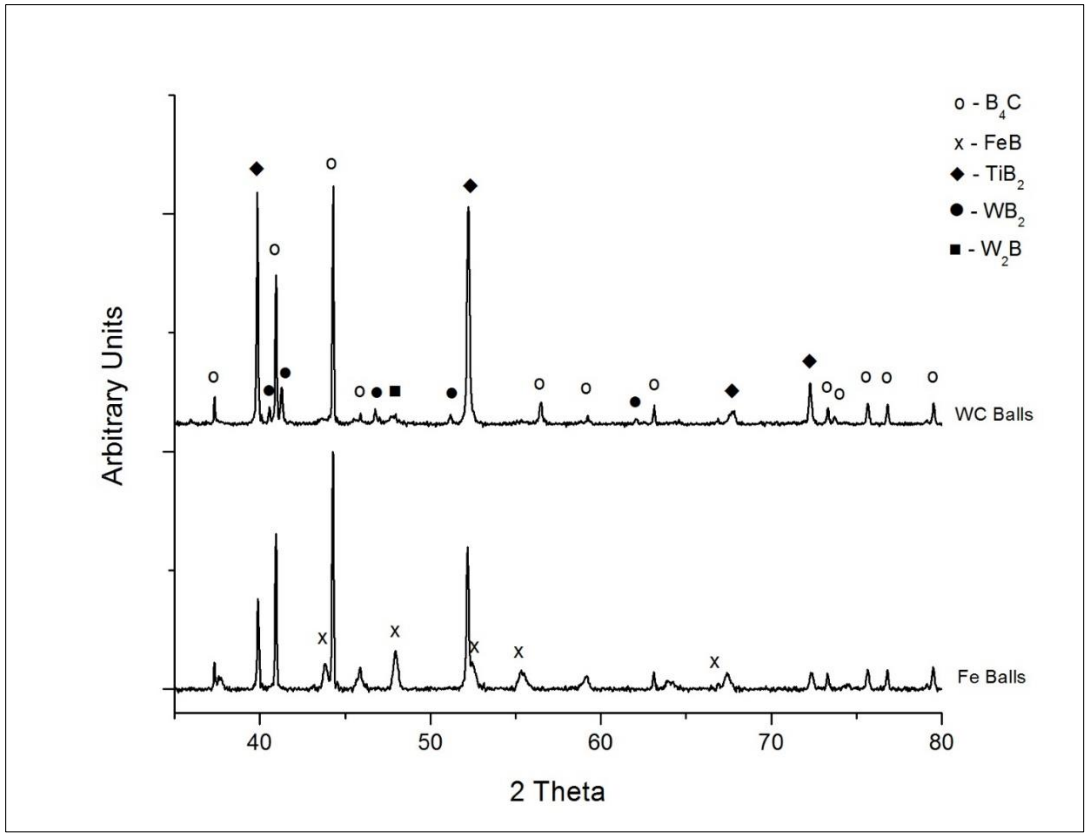


Figure 33: XRD analysis of the 5 vol% Ti-B_4C composites prepared using WC milling balls and Fe milling balls produced at 2000°C and 30MPa.

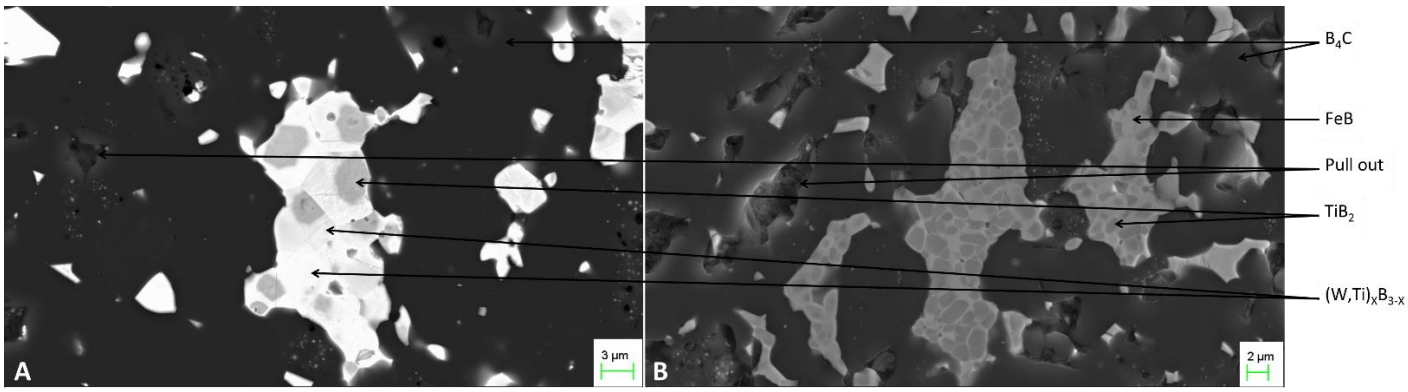


Figure 34: BS-SEM micrographs comparing the 5 vol% Ti-B_4C composites prepared using A) WC milling balls and B) Fe milling balls and produced at 2000°C and 30MPa.

4.4. Transverse Rupture Strength

The ball on three ball (B3B) testing technique was used to determine the transverse rupture strength of selected composites (each with a relative density ≥ 97 %) as laid out in Table 10. To obtain reasonable statistical data, ten tests were performed on each composite as laid out in the experimental procedure. This allowed for the determination of a representative mean (σ_{Mean}) and characteristic strength (σ_o) with the characteristic strength being indicative of that at which the sample would have a probability of survival (Ps) of 37 %. Statistical analysis of the measurement data sets was performed in accordance with BS EN 843-5.[123] Confidence intervals of 90 % (CI^{90}) were applied to consider statistical uncertainties of the m and σ_o parameters, estimated using the maximum likelihood method, and are quoted in Table 10. The effective volume factor (kV in equation 5) and the corresponding stress were determined to allow for comparison of materials of different sizes and also different geometries.

Table 10: B3B strength and Weibull modulus (m) calculated using the ball on three ball test.

Composite	Temperature (°C)	Density (g/cm^3)	Relative Density (%)	σ_{Mean} (MPa)	m [CI^{90}]	σ_o (MPa) [CI^{90}]	V_{eff}	$\sigma_{o,Veff}$ (MPa) [CI^{90}]
69.3% Fe-B_4C	1100	6.80	97.1±0.1	303±34	9.8 [5.4, 13.2]	339.1 [323.2, 355.7]	0.084	263.4 [251.1, 276.3]
78% Fe-B_4C	1100	7.27	97.1±0.2	446±45	12.1 [6.7, 16.4]	495.6 [476.9, 515.1]	0.049	386.5 [371.9, 401.7]
80.9% Fe-B_4C	1100	7.29	97.9±0.2	437±64	6.9 [3.8, 9.3]	497.1 [464.4, 532.2]	0.182	388.3 [362.8, 415.7]
69.3% (0.8Fe+0.2Ti)-B_4C	1100	6.20	97.2±0.2	323±25	11.6 [6.4, 15.7]	361.1 [346.6, 376.2]	0.060	283.3 [272.0, 295.2]
1% Fe-B_4C	2000	2.61	97.7±0.5	411±41	9.9 [5.5, 13.4]	458.9 [437.6, 481.3]	0.120	370.5 [353.3, 388.5]
1% (0.8Fe+0.2Ti)-B_4C	2000	2.61	97.6±0.2	377±56	5.6 [3.1, 7.6]	431.4 [396.5, 469.3]	0.586	392.1 [360.4, 426.5]

Observing the characteristic strengths in Table 10 showed σ_o to increase from 339.1 MPa to 495.6 MPa as the Fe concentration increases from 69.3 to 78 %. The further increase to 80.9 % Fe saw a slight change in σ_o to 497.1 MPa, however the σ_{Mean} values show the 80.9 % Fe-B_4C to be lower than that of the 78 % Fe-B_4C. Observing the standard deviation of the 78 and 80.9 % Fe suggests that there is in fact little to no change in strength at these compositions. The addition of Ti in the 69.3% (0.8Fe+0.2Ti)-B_4C showed little effect on the strength compared to the 69.3 %

Fe sample. It is clear from Table 10 that additions of 1% Fe to B_4C resulted in a characteristic strength of 458.9 while replacing 20 vol % of the iron in this composition with Ti saw a decrease in characteristic strength to 431.4 MPa.

Table 10 shows the unbiased Weibull modulus of 12.1 for the 78% Fe-B_4C composite was the largest observed while the modulus of 5.6 for the 1% (0.8Fe+0.2Ti)-B_4C was the lowest.

4.4.1. Analysis of Fracture

The majority of composites were seen to break into three pieces (Figure 35), however, a few did break into more (up to six). This was more prevalent among the composites containing 99 vol. % B_4C. Fracture still initiated at the centre for all the samples and this was corroborated through SEM analysis shown in Figure 36 (A1, B1, C1, D1) and Figure 37 (A1, B1).

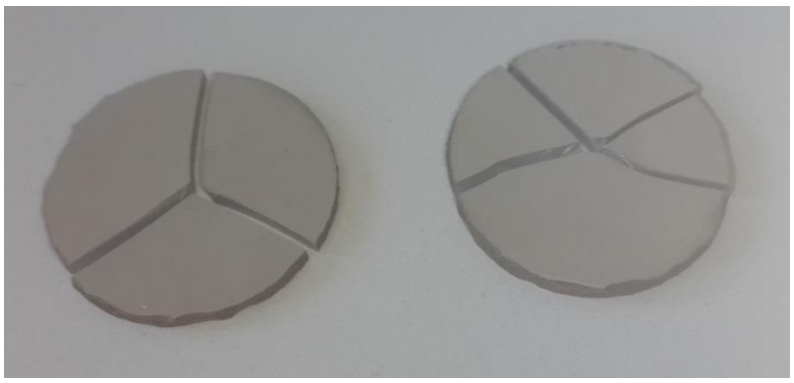


Figure 35: Typical mode of fracture observed showing initiation at the center of the samples.

In Figure 36 (A2, B2, C2) there was evidence of both intergranular and transgranular fracture as cracks propagated through the samples. The porosity observed in these composites was present at the grain boundaries. The structure of each of these composites was fairly similar however, in Figure 36 (A2) the carbon rich areas, previously observed in Figure 23, were clearly observable.

These areas were seen to have a sponge-like appearance with carbon dispersed through iron rich areas which XRD (Figure 22) and EDX analysis suggest to be Fe(B,C). Fracture through the 69.3% (0.8Fe+0.2Ti)-B_4C in Figure 36 (D2), showed evidence of transgranular fracture with no clearly observable intergranular fracture.

Figure 37 showed transgranular fracture with areas of pull-out in the 1% Fe-B_4C while the addition of Ti in the 1% (0.8Fe+0.2Ti)-B_4C saw evidence of transgranular fracture through the B_4C phase, with areas of intergranular fracture around the TiB_2 containing phase.

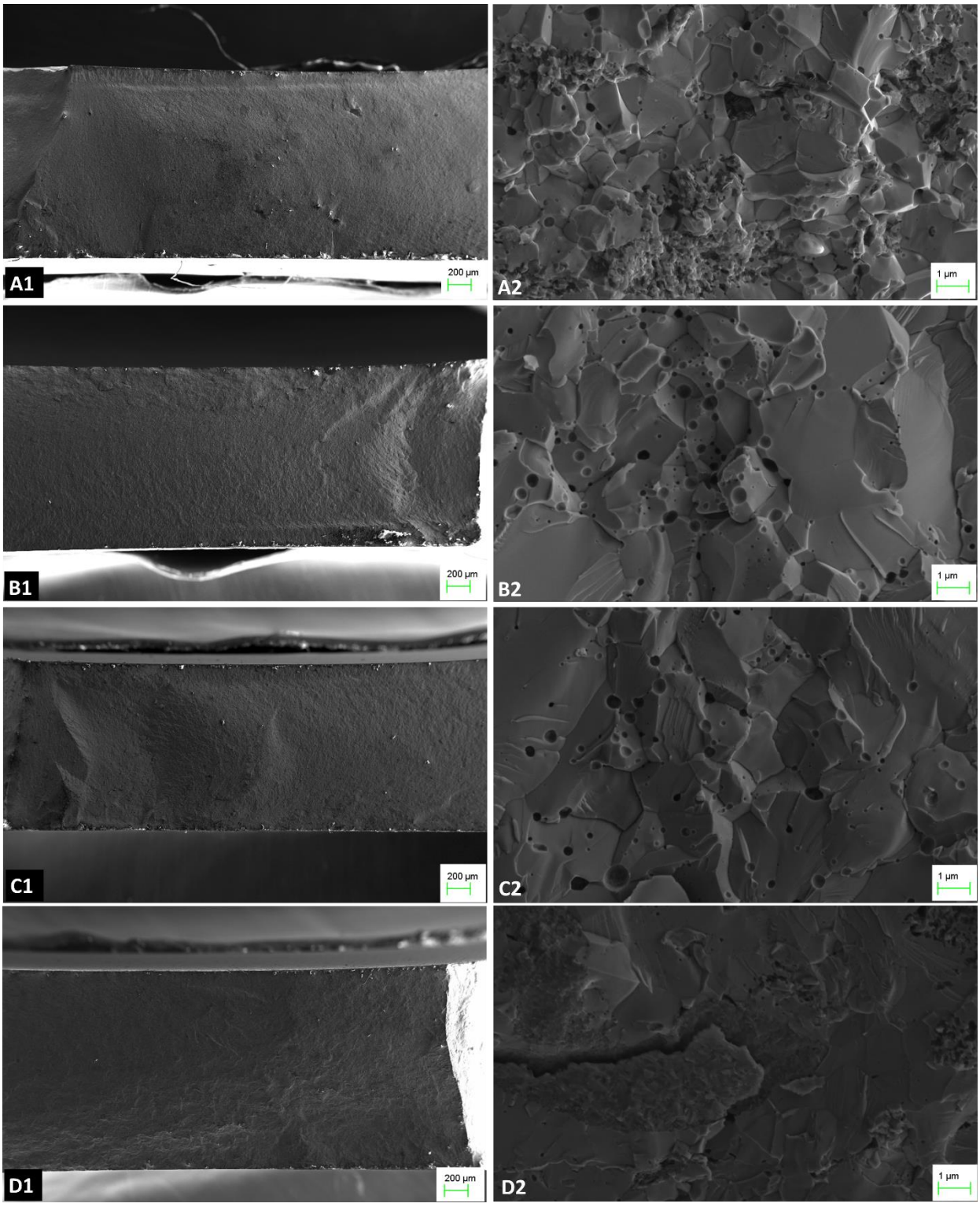


Figure 36: SE-SEM micrographs showing the microstructure of the A) 69.3 vol%, B) 78 vol% and C) 80.9 vol% Fe-B_4C B3B fractured composites sintered at 1100°C and 60 MPa.

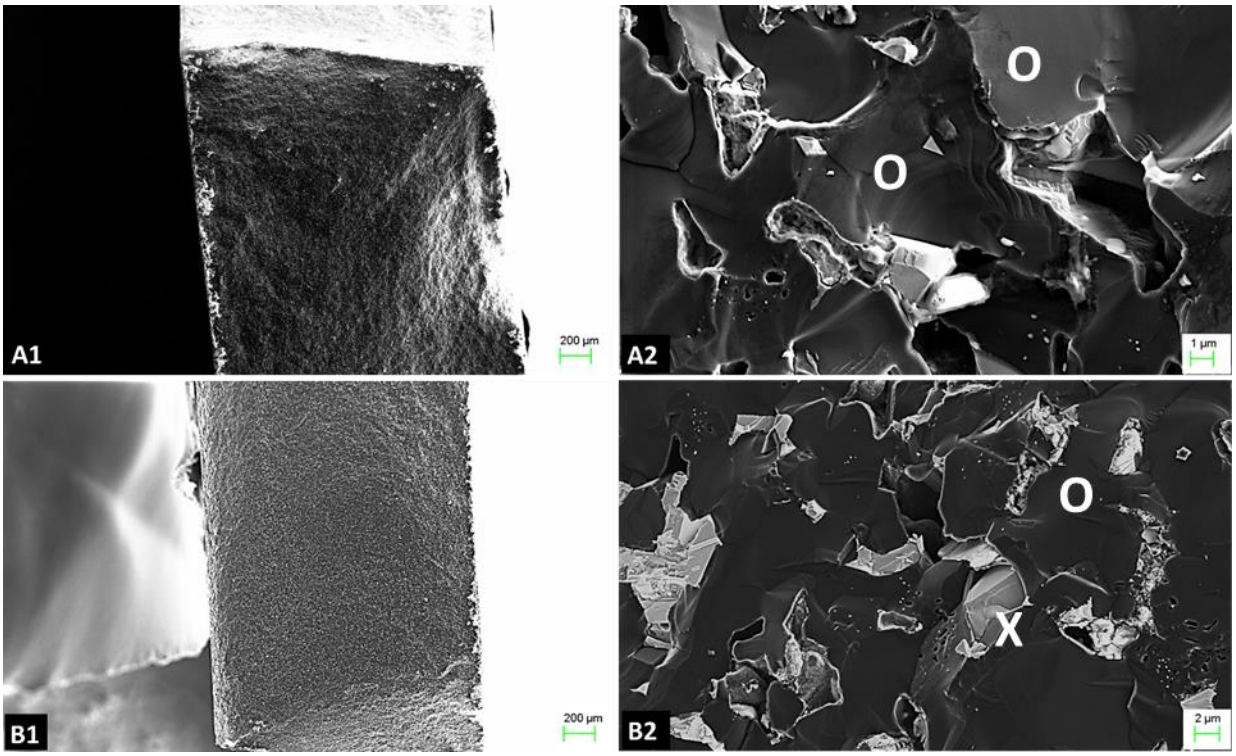


Figure 37: SE-SEM micrographs of the microstructure observed for A) 1% Fe-B_4C and B) 1% (0.8Fe+0.2Ti)-B_4C TRS fractured composites sintered at 2000°C and 30 MPa (Transgranular fracture marked O and intergranular marked X).

4.5. Wear

The wear resistance of select composites was investigated using the sliding wear technique. The samples were prepared and the tests carried out as described in chapter 3.2.6. The behaviour of both the composite and the sliding counterbody (wear ball) was observed.

4.5.1. Wear Resistance of Balls and Composites

The sliding wear resistance testing was primarily determined using INOX 420 stainless steel balls. Silicon nitride balls were used on select compositions to provide a comparison between the wear balls and their effect on wear resistance. The compositions investigated, along with their corresponding wear rates and friction coefficients, are shown in Table 11.

Table 11: Sliding wear resistance (load = 10 N, speed = 0.21 m/s, sliding distance = 300 m, environment – air, no lubricant, humidity 55 to 65%).

Composite	Temperature (°C)	Pressure (MPa)	Density (g/cm^3)	Relative Density (%)	Wear Ball	Coefficient of Friction (μ)	Ball Wear			Sample Wear	
							Wear Scar Diameter (μm)	ΔV_{Ball} ($x10^{-3}$ mm^3)	Ball Wear Rate ($x10^{-6}$ mm^3/Nm)	Wear Volume ($x10^{-2}$ mm^3)	Sample Wear Rate ($x10^{-6}$ mm^3/Nm)
69.3% Fe-B_4C	1100	60	6.80	97.1±0.1	SS	0.79±0.02	980	15.2±0.3	5.08±0.10	2.67±0.04	8.90±0.14
78% Fe-B_4C	1100	60	7.27	97.1±0.2	SS	0.84±0.01	990	15.9±0.1	5.29±0.11	3.92±0.03	13.08±0.10
80.9% Fe-B_4C	1100	60	7.29	97.9±0.2	SS	0.91±0.02	1070	21.7±0.4	7.23±0.14	4.12±0.06	13.72±0.20
69.3% Fe-B_4C	1100	60	6.80	97.1±0.1	SN	0.58±0.01	495	1.0±0.7	0.33±0.01	0.53±0.01	1.77±0.02
78% Fe-B_4C	1100	60	7.27	97.1±0.2	SN	0.69±0.01	560	1.6±0.5	0.54±0.02	1.40±0.01	4.66±0.03
80.9% Fe-B_4C	1100	60	7.29	97.9±0.2	SN	0.80±0.02	820	7.4±0.2	2.48±0.06	2.20±0.04	7.32±0.13
69.3% (0.8Fe+0.2Ti)-B_4C	1100	60	6.20	97.2±0.2	SS	0.84±0.01	1380	60.4±0.6	20.14±0.29	3.72±0.04	12.39±0.12
1% Fe-B_4C	2000	30	2.73	97.7±0.5	SS	0.70±0.03	690	3.7±0.1	1.24±0.04	5.39±0.06	17.98±0.19
1% Fe-B_4C	2000	30	2.73	97.7±0.5	SN	0.48±0.01	807	7.0±0.2	2.33±0.06	11.08±0.14	36.92±0.48
1% (0.8Fe+0.2Ti)-B_4C	2000	30	2.68	97.6±0.2	SS	0.70±0.03	680	3.5±0.1	1.17±0.03	10.56±0.02	35.20±0.08
5% Fe-B_4C	2000	30	2.79	98.4±0.2	SS	0.82±0.02	970	14.6±0.3	4.87±0.10	8.83±0.13	29.45±0.43
5% Ti-B_4C	2000	30	2.96	97.2±0.5	SS	0.71±0.03	958	13.9±0.3	4.63±0.10	3.50±0.05	11.68±0.16

*Wear Ball: SS = stainless steel and SN = silicon nitride

Each composite that underwent wear testing was produced under conditions allowing for densification of at least 97 %. The composites with the higher additions of iron selected (69.3% Fe-B_4C, 78% Fe-B_4C, 80.9% Fe-B_4C) were all sintered at 1100°C and 60MPa. When tested with steel balls, it was evident that increasing iron concentration resulted in higher coefficients of friction and wear rates. The same trend was observed when using Si_3N_4 balls, however, resultant wear rates were significantly lower in comparison to steel balls. The introduction of Ti in the 69.3% (0.8Fe+0.2Ti)-B_4C sample showed less wear resistance than its 69.3% Fe-B_4C counterpart, with the coefficient of friction and wear rate being more comparable to 78% Fe-B_4C. Thus, the 69.3% Fe-B_4C composite showed the highest wear resistance with a wear rate of 8.90×10^{-6} mm^3/Nm when using steel balls and 1.77×10^{-6} mm^3/Nm with silicon nitride.

The 1% Fe-B_4C had a wear rate of 17.98×10^{-6} mm^3/Nm with steel balls and 36.92×10^{-6} mm^3/Nm with silicon nitride balls. The addition of titanium in the 1% (0.8Fe+0.2Ti)-B_4C showed an increase in wear rate to 35.20×10^{-6} mm^3/Nm with steel balls, almost double that of the corresponding 1% Fe-B_4C even though they had almost identical friction coefficients. Increasing the iron concentration to 5% also showed an increase in friction coefficient and wear rate compared to the 1 % addition with steel balls. A 5% Ti-B_4C composite was used for comparative purposes and was seen to have higher wear resistance than the 1 and 5 % iron additions with a wear rate of 11.68×10^{-6} mm^3/Nm.

The wear rates of the balls were calculated by measuring the wear scar on its surface under an optical microscope. This allowed for the volume of material lost and the subsequent wear rate to be determined as per the experimental procedure. Table 11 reports the wear rates determined for each of the balls in the tests performed. It is evident from these results that the for the high Fe compositions, the wear on the balls increased with increasing the Fe content and while the same trend was observed for the Si_3N_4 balls, the volume worn was significantly less than the stainless steel balls. The addition of titanium in the 69.3% (0.8Fe+0.2Ti)-B_4C saw a drastic increase in the wear rate of the stainless steel ball. As shown in Table 11, the ball wear rate was ≈ 4 times the 5.08×10^{-6} mm^3/Nm seen for the 69.3% Fe-B_4C composite, with a wear rate of 20.14×10^{-6} mm^3/Nm.

The ball wear rates observed for the 1 vol. % additions to B_4C showed the Si_3N_4 ball to have a wear rate of 2.33×10^{-6} mm^3/Nm, approximately double those observed on the stainless steel

balls. Introducing Ti in the 1% (0.8Fe+0.2Ti)-B_4C sample showed little to no change in the wear observed on the wear balls. The steel balls used on the composites with 5 vol. % additions of Fe and Ti showed wear rates of 4.87×10^{-6} mm^3/Nm and 4.63×10^{-6} mm^3/Nm respectively. Increasing the iron from 1 to 5 vol. % again showed an increase (≈ 4×) in the observed wear for the steel balls.

4.5.1. Analysis of Wear Scars

The appearance of the wear scars present on the balls was investigated and shown in Figure 38. The appearances of the steel balls used on the high Fe-B_4C were all similar, apart from the size of the wear scar. In each of these cases (69.3% (0.8Fe+0.2Ti), 69.3% Fe, 78% Fe and 80.9% Fe with B_4C) the balls appear to have been ground down in the process of sliding across the surface. The 69.3% (0.8Fe+0.2Ti)-B_4C composite had the largest wear scar observed on the balls (1380 µm) with areas where large amounts of material were removed while interacting with the sample. The stainless steel balls used on the (1-5% Fe and (Fe+Ti) to B_4C) composites each showed what appeared to be material that had molten and solidified at the boundary of the scar. This was most prominent in the 1% Fe-B_4C and the 1% (0.8Fe+0.2Ti)-B_4C. Minuscule amounts of this structure were observed at the boundary of the 5% Fe-B_4C however, when investigating the 5% Ti-B_4C, this was no longer visible.

From Figure 38, there were again similarities in appearance for the Si_3N_4 balls used in sliding wear tests on the 69.3, 78 and 80.9% Fe-B_4C. Most notably when observing these balls is the change in the scar size on the ball, increasing from 495 µm when used on 69.3% Fe-B4C composites to 820 µm when used on 80.9 % Fe-B_4C. The surface of these balls had a smeared appearance when compared to the surface of the Si3N4 ball that was used on the 1% Fe-B_4C which had a wear scar of similar size (810 µm) to the ball used on 80.9% Fe-B_4C (820 µm). This ball looks to have been ground down during the sliding process in a less aggressive fashion than the stainless steel balls used on the high Fe-B_4C composites.

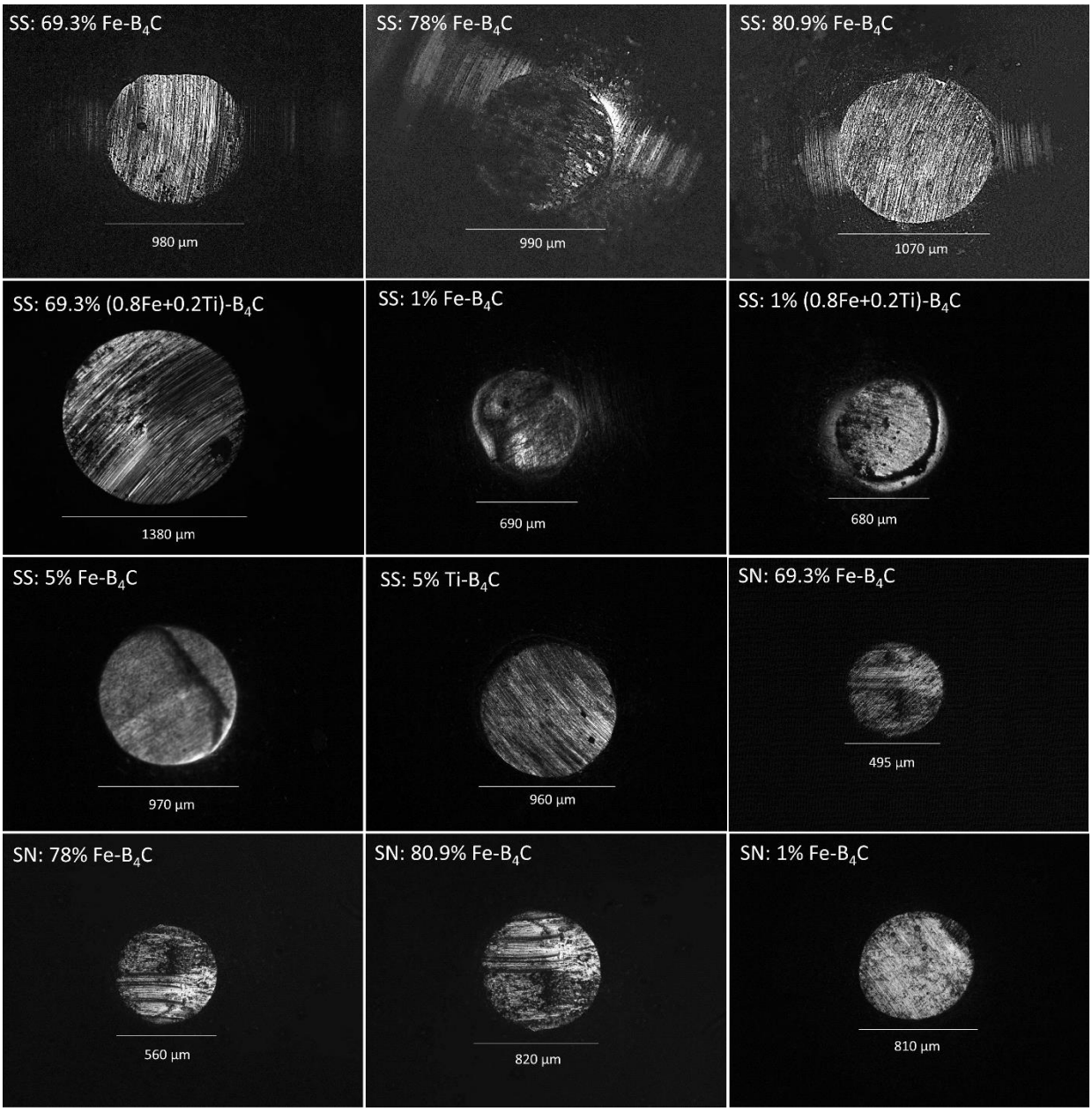


Figure 38: Wear scars observed on stainless steel (SS) and silicon nitride (SN) wear balls under an optical microscope.

To understand the wear behaviour of the materials tested, SEM and EDX analysis was used to observe the wear tracks produced. SEM allowed not only for the general size and regularity of the wear track to be observed, but also the wear debris present and the microstructure within the track, providing an insight into the manner with which wear occurred. EDX analysis was primarily used to identify the phases of any debris present in the wear track.

4.5.1.1. Analysis of wear scars for tests performed using stainless steel balls

Figure 39 shows the wear tracks produced using steel balls, and evidence of the wear debris present in each, for the 69.3% Fe-B_4C, 78% Fe-B_4C, 80.9% Fe-B_4C and 69.3% (0.8Fe+0.2Ti)-B_4C composites. The width of the wear scar was seen to increase with increasing iron concentration, going from ≈500 to ≈800 μm for the 69.3% Fe-B_4C and 80.9% Fe-B_4C composites respectively. Wear debris was present in each wear track; however, the quantity of debris appeared to increase with increasing iron content. A number of grooves were present within the wear tracks as a result of the material being gouged out by the wear ball.

EDX was used to identify the elements present in the wear track. Figure 40 shows the elemental EDX maps that were produced when observing and identifying the wear debris in the wear track. In each case, the debris was determined to be an iron oxide phase. There is a small presence of chromium associated with these phases which would have been present in the stainless steel ball.

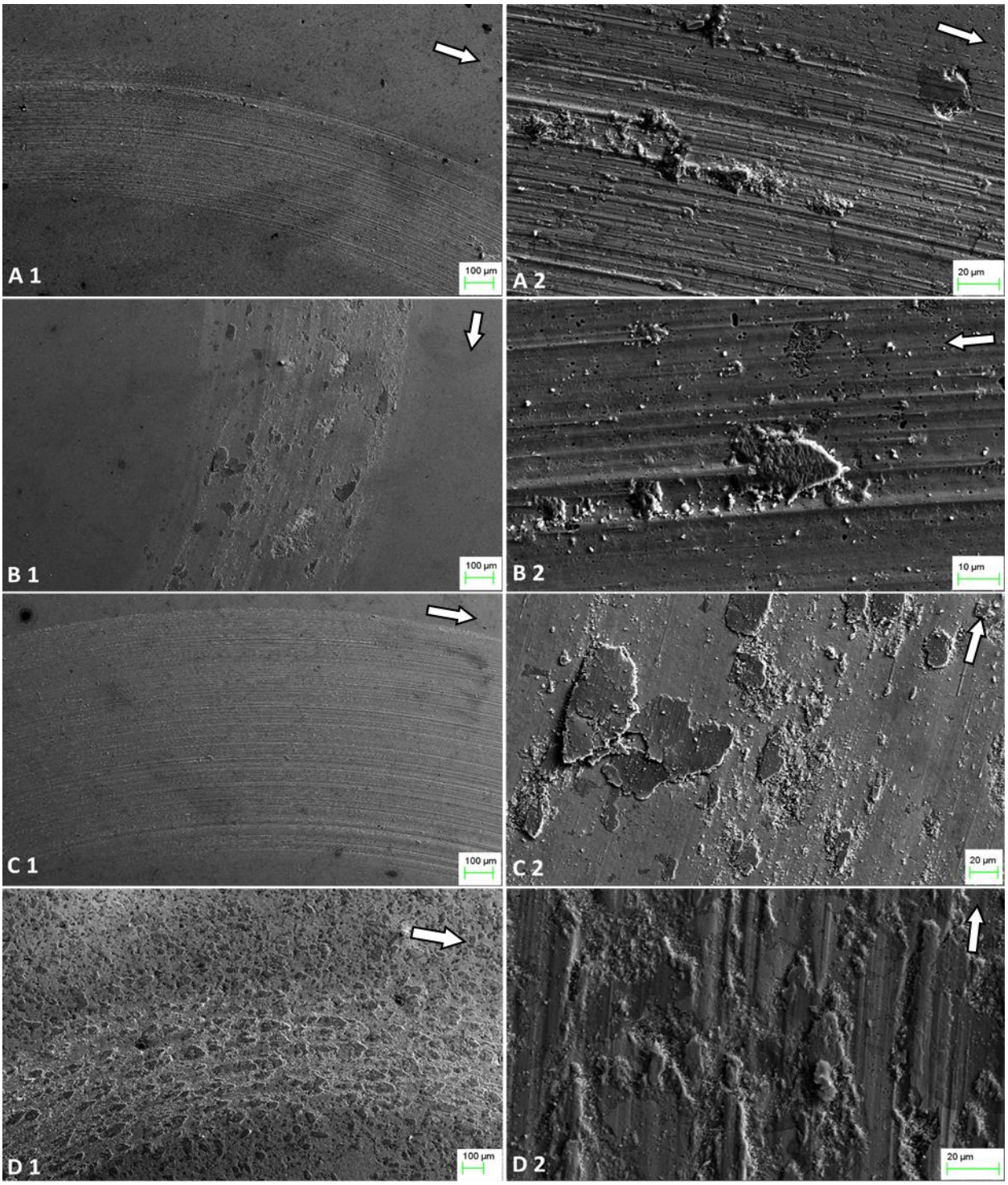


Figure 39: SE-SEM micrographs of the wear scar and its appearance therein for A) 69.3% Fe- B_4C, B) 78% Fe- B_4C, C) 80.9% Fe-B_4C and D) 69.3% (0.8Fe+0.2Ti)-B_4C sintered at 1100°C and 60 MPa with ball direction indicated.

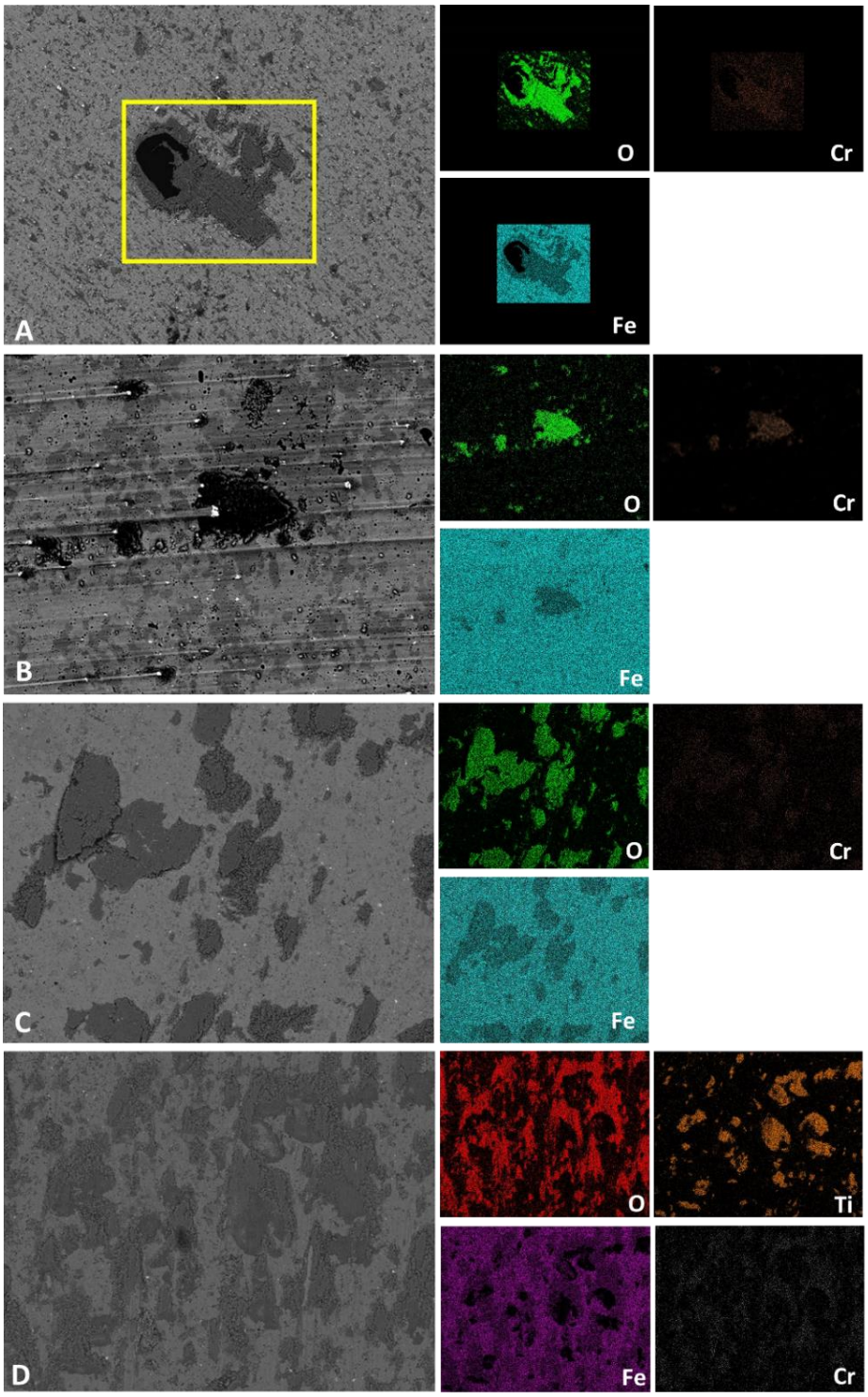


Figure 40: EDX analysis showing wear debris on the A) 69.3% Fe-B_4C, B) 78% Fe-B_4C, C) 80.9% Fe-B_4C and D) 69.3% (0.8Fe+0.2Ti)-B_4C to contain an oxide phase.

When observing the microstructure of the wear track at higher magnifications, a number of cracks were observed, the majority of which ran perpendicular to the sliding direction of the ball. This was the case for each of the composites but was most excessive in the 80.9% Fe-B_4C composite depicted in Figure 41. Examination of the cracks in the backscatter SEM micrograph (Figure 41 b.) showed evidence of crack deflection with intergranular and transgranular cracks indicated with the black and white arrows respectively. Intergranular cracks are most commonly noticed where a secondary phase is met, although not always as indicated by the white arrows. From the secondary electron SEM micrograph in Figure 41 a), areas where material had been removed from the surface were visible.

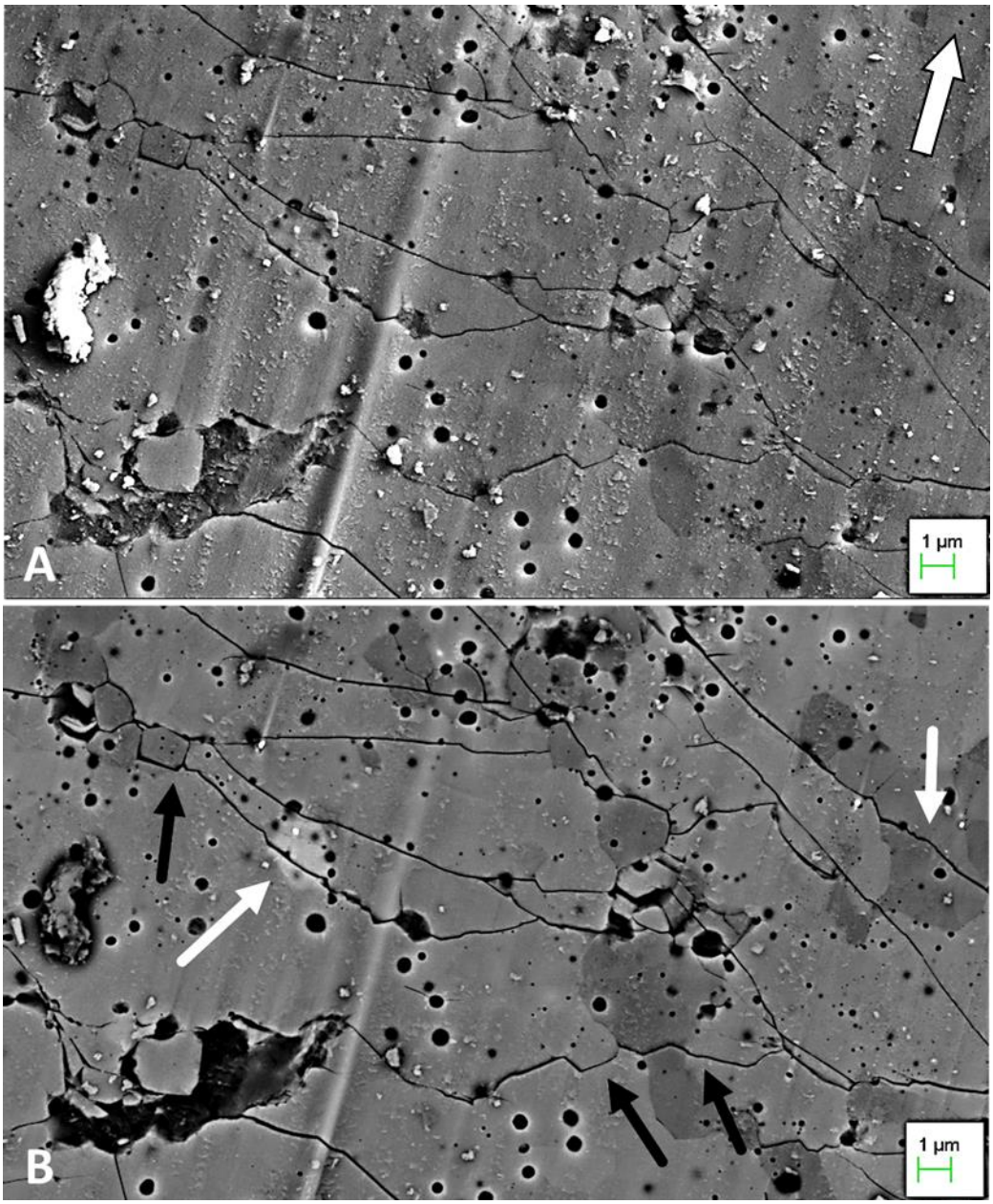


Figure 41: SEM micrographs of the wear scar of the 80.9 vol% Fe-B_4C showing cracks and debris in a) secondary electron mode with ball direction indicated and b) backscatter mode with crack type indicated. (white arrows – transgaranular, black arrows intergranular fracture)

The wear track was observed for 1% Fe-B_4C, 1% (0.8Fe+0.2Ti)-B_4C and 5% Fe-B_4C in Figure 42. The appearance of the wear tracks in Figure 42 (A1, B1, C1) was similar for each for each composite at lower magnifications. At higher magnifications, where the microstructure within

the wear track was observed, differences were more apparent. The 1 and 5% Fe-B_4C (Figure 42 (A2, C2)) show areas where a large amount of material was removed from the surface. The extent of surface damage was greater in the 1% Fe-B_4C even though the widths of the wear tracks were approximately the same (≈ 780 μm). While there was some debris on these surfaces, the 1% (0.8Fe+0.2Ti)-B_4C sample in Figure 42 (B2) had significant quantities of debris throughout the wear track. The surface of the sample showed signs of the same behavior as those without addition of Ti with debris being deposited in the areas where material had been removed from the surface. EDX analysis (Figure 43) showed the debris present to be an iron oxide phase. The presence of the debris was least prominent in 5% Fe-B_4C while the Ti addition resulted in a large increase in the presence of the oxide phase in the 1% (0.8Fe+0.2Ti)-B_4C when compared to the 1% Fe-B_4C.

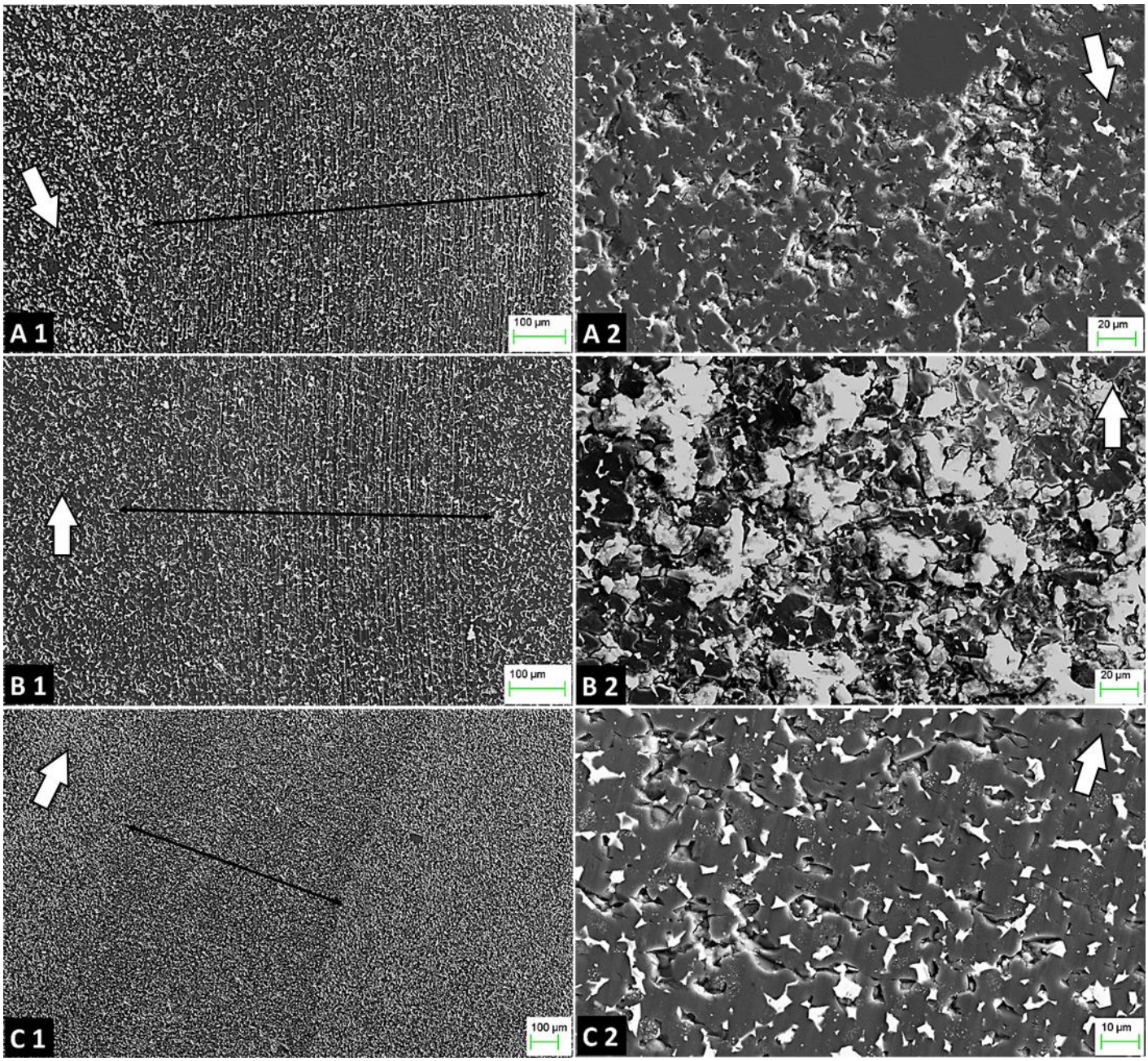


Figure 42: SE-SEM micrographs of the wear scar and its appearance therein for A) 1% Fe-B_4C, B) 1% (0.8Fe+0.2Ti)-B_4C and C) 5% Fe-B_4C when using stainless steel balls with ball direction indicated.

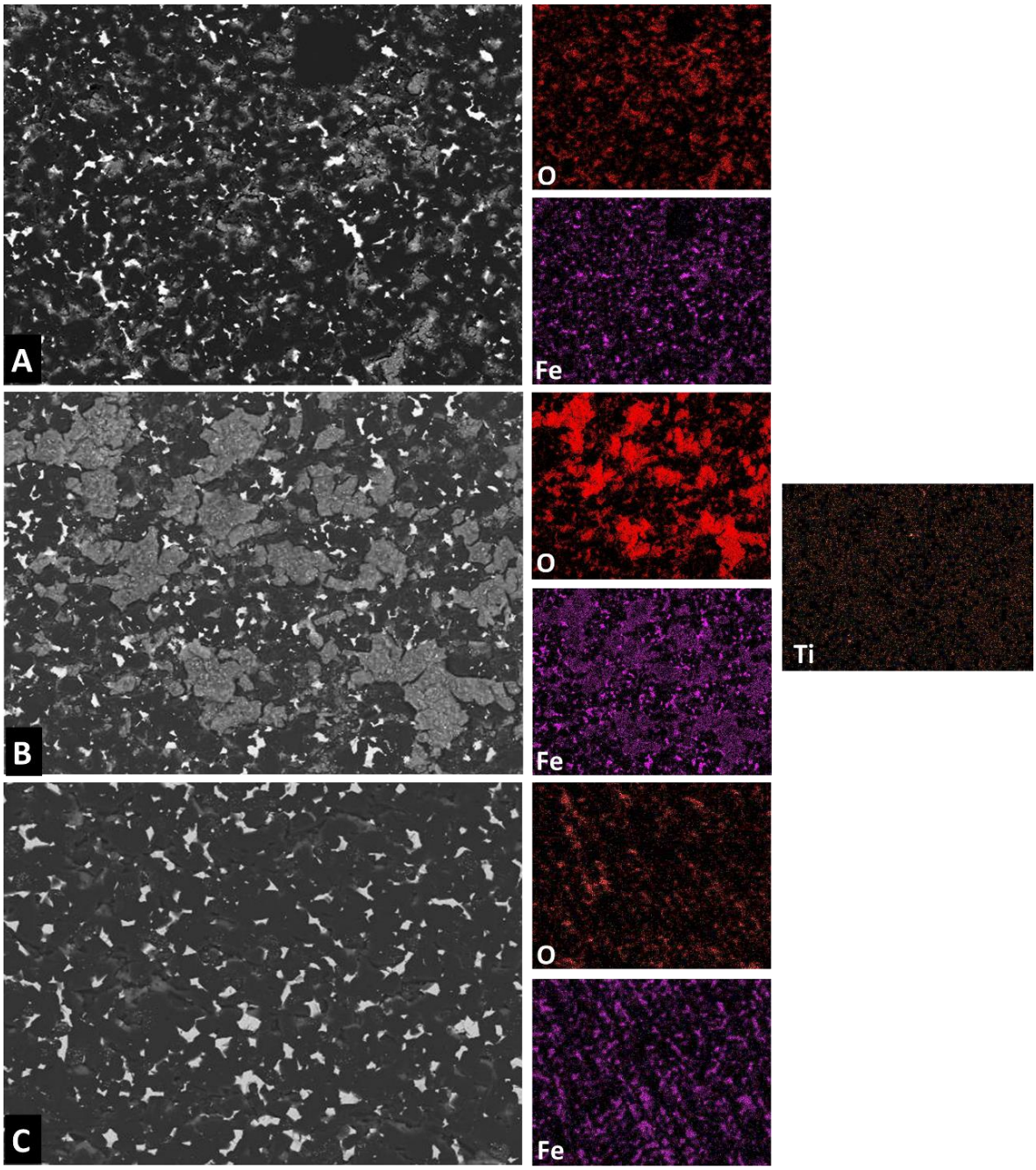


Figure 43: EDX analysis of the wear track for A) 1% Fe-B_4C, B) 1% (0.8Fe+0.2Ti)-B_4C and C) 5% Fe-B_4C.

4.5.1.2. Wear scar analysis for tests performed with silicon nitride balls

Silicon nitride wear balls were used as the counterbody on select samples to observe the difference when compared with the stainless steel. From Figure 44 (A1, A2) it was clear that the use of Si_3N_4 balls on the 1% Fe-B_4C composite produced a wear track with a width of ≈ 800 µm and the microstructure along the wear track showed evidence of the FeB phase being removed more readily than the B_4C matrix material.

The use of Si_3N_4 balls on 78 and 80.9% Fe-B_4C resulted in wear tracks of ≈600 and 700 µm respectively. This was shown in Figure 44 (B1, C1) where it was also clear that the wear track contained large amounts of debris which had the appearance of being smeared across the surface during testing. In Figure 44 (B2, C2) the wear track was viewed at higher magnifications where it became apparent that there were once again cracks dispersed throughout the wear track surface.

When investigating 1% Fe-B_4C (Figure 45 (A)), oxide debris was seen to congregate mostly in areas where FeB was and had previously been present. Although EDX analysis suggests the presence of Si on the surface, this was only in areas where WC was present, due to similarities in the Si and W EDX spectra, as seen in Figure 45. Thus, there was no real correlation between the Si and O in this composite, suggesting mainly iron oxide wear debris. The debris present in Figure 45 (B and C) was mainly a silicon oxide phase with a small presence of iron oxide. Figure 45 (B and C) shows the higher Fe compositions of 78 and 80.9 % with B_4C had areas with no debris between areas of debris which had been pushed aside where the ball was in contact with the sample.

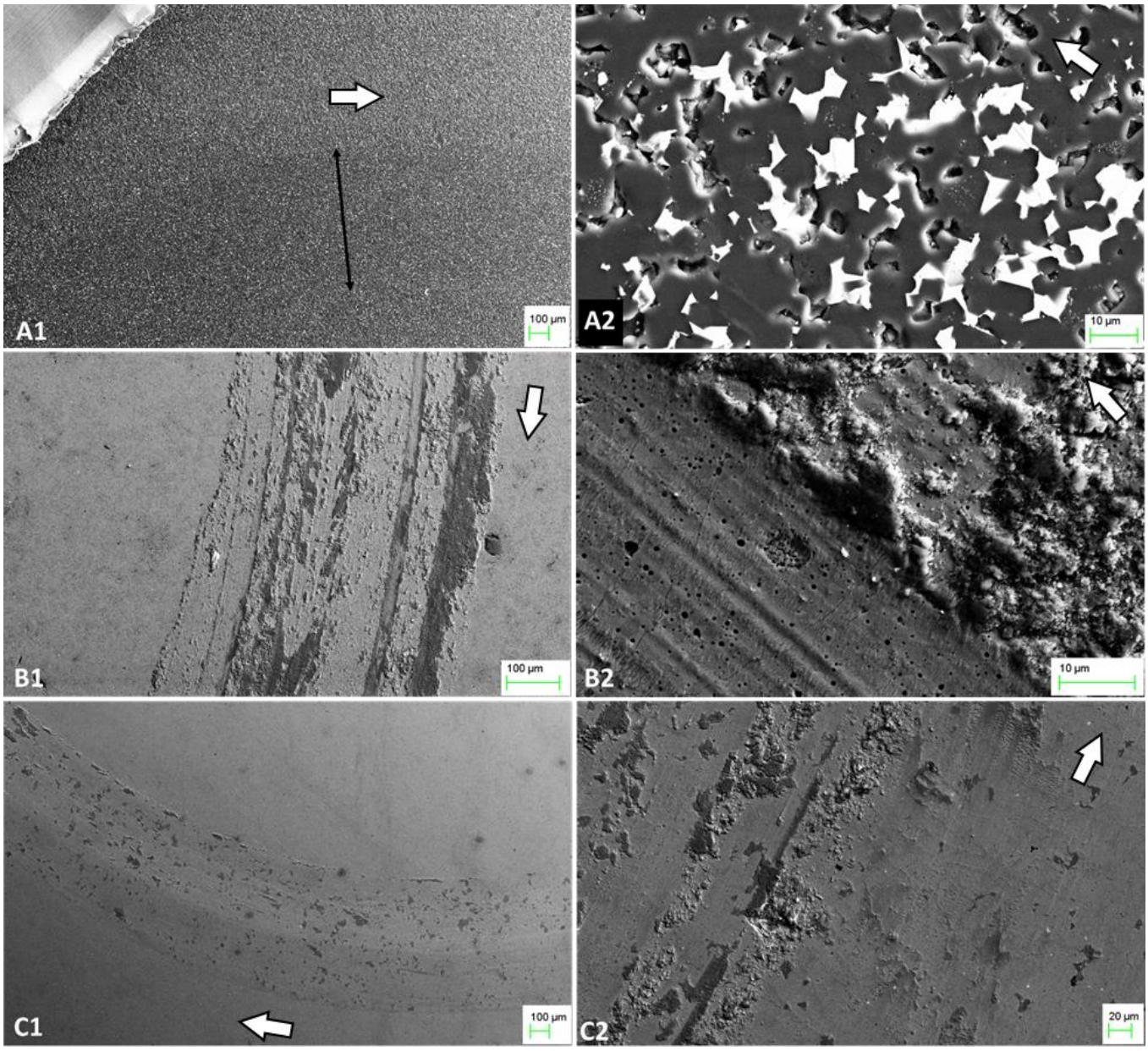


Figure 44: SE-SEM micrographs of the wear scar for A) 1% Fe-B_4C, B) 78% Fe-B_4C and C) 80.9% Fe-B_4C when using silicon nitride balls with ball direction indicated.

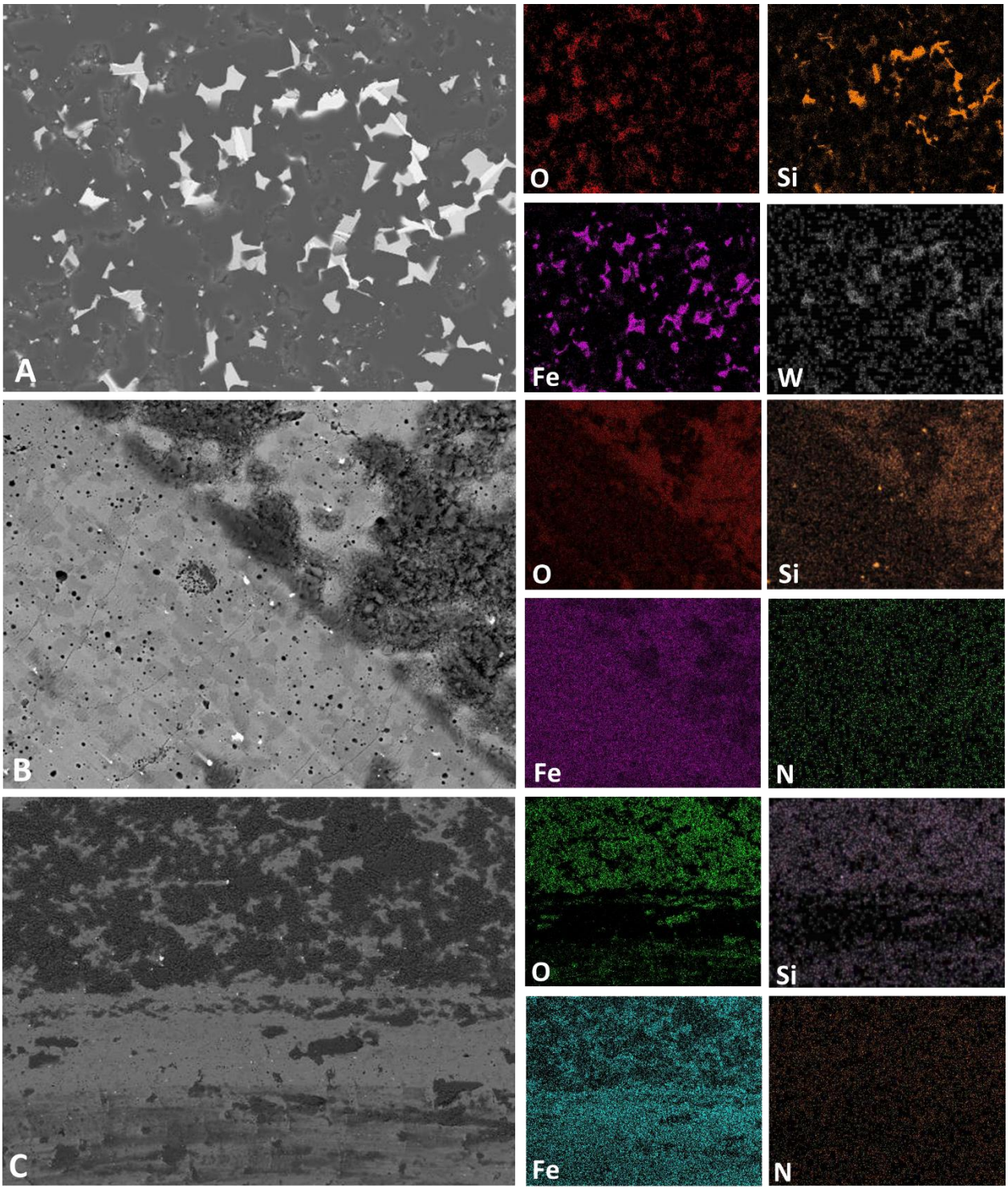


Figure 45: EDX analysis on wear debris for A) 1% Fe-B_4C, B) 78% Fe-B_4C and C) 80.9% Fe-B_4C when using Si_3N_4 balls.

The appearance of the microstructure of the wear track in the 78 and 80.9% Fe-B_4C samples was similar, with both exhibiting signs of microcracks across the surface and a scale-like appearance in areas throughout the respective wear tracks. The effect was visible in Figure 46 depicting the 80.9% Fe-B_4C composite with the scale-like structure using secondary electron mode in the micrograph in Figure 46 (A) and the cracks in Figure 46 (B) applying backscatter mode. The cracks were seen to deflect around secondary phases and at pore interfaces.

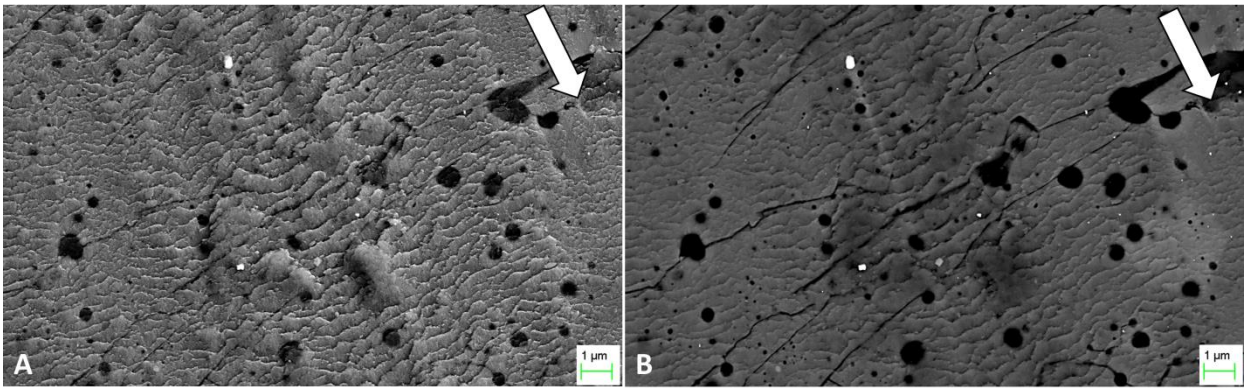


Figure 46: SEM micrographs (SE-mode) (A) and (BS-mode) (B) of the wear track microstructure in the 80.9% Fe-B_4C composite tested with Si_3N_4 balls with the ball sliding direction indicated.

5. Discussion

5.1. Powder Processing

Powder metrology performed using particle size analysis and SEM provided information on the size range, presence of agglomeration and morphology of each powder used. The particle size distributions of the powders were described by the d_{10}, d_{50} and d_{90} particle sizes observed. The d_{50} values determined (Figure 14 and Table 6) were used as an indication of the average particle size[145] and were in agreement with those provided by the suppliers (Table 3).

Agglomeration was observed in each of the Fe, B_4C and Ti powders through SEM analysis, however, ultrasonication up to 30 min was sufficient to disperse the powders and produce unimodal size distributions. Particle sizes observed in the SEM micrographs (Figure 15) agreed with the measured particle size distribution curves (Figure 14). The larger outlying particles (d_{90}-Table 6) in the B_4C and Ti are consistent with powders of angular geometries being sieved to < 10 and < 44 μm respectively.[146] The B_4C, Fe and Ti phases observed through XRD analysis of the starting powder (Figure 16), along with EDX elemental analysis, were as expected and in line with the suppliers' claims of ≥ 99 % purity.

When considering contamination from the milling media, the composition ranges shifted. The effect of contamination on the compositions is shown in Table 12, where composites with small additions to B_4C were the most affected. The 1 to 5 vol. % Fe-B_4C composition range shifted to between 4.5 and 5.8 vol. % Fe-B_4C, resulting in a smaller investigation range.

Table 12: Effect of milling ball contamination on the powder composition for sintering.

Powder Composition pre-mixing (vol. %)	Powder Composition post-mixing (vol. %)
1 % Fe- B_4C	4.5 % Fe- B_4C
3 % Fe- B_4C	5.2 % Fe- B_4C
5 % Fe- B_4C	5.8 % Fe- B_4C
69.3 %Fe- B_4C	69.9 % Fe- B_4C
78 % Fe- B_4C	78.4 % Fe- B_4C
80.9 %Fe- B_4C	81.3 % Fe- B_4C
1 % (0.8Fe+0.2Ti) - B_4C	3.8 % (0.95Fe+0.05Ti) - B_4C
3 % (0.8Fe+0.2Ti) - B_4C	4.8%(0.88Fe+0.12Ti) - B_4C
5 % (0.8Fe+0.2Ti) - B_4C	5.7 % (0.82Fe+0.18Ti) - B_4C
69.3 % (0.8Fe+0.2Ti) - B_4C	69.8%(0.8Fe+0.2Ti) - B_4C
78 %(0.8Fe+0.2Ti) - B_4C	78.4%(0.8Fe+0.2Ti) - B_4C
80.9 % (0.8Fe+0.2Ti) - B_4C	81.3%(0.8Fe+0.2Ti) - B_4C
1% Ti - B_4C	3.7 % (0.73Fe+0.27Ti) - B_4C
3% Ti - B_4C	4.7 % (0.36Fe+0.64Ti) - B_4C
5% Ti - B_4C	5.5 % (0.10Fe+0.90Ti) - B_4C
5% Ti - B_4C	7.1 % (0.69Ti+0.31WC) - B_4C
8% Ti - B_4C	9.9 % (0.80Ti+0.20WC) - B_4C

For continuity and ease of relating materials to each other, the samples are referred to as their initial mix composition, but the post mix compositions were considered when analyzing the materials.

5.2. Sintering behavior and properties of sintered composites

Results obtained from sintering B_4C with additions of Fe $\geq$ 69.3 vol. % were analysed and compared to one another. Sintering data from the SPS process was used to provide the densification curves for each of the materials shown in Figure 47.

Densification curves in Figure 47, show the effect of composition on densification results attained (Table 8) at sintering temperatures of 900, 1000 and 1100°C and a pressure of 60 MPa. The pyrometer responsible for the temperature reading and its subsequent control in the SPS,

only provides sintering data from temperatures above 400°C. At these temperatures, densification of each sample had already begun. Consequently, the exact temperatures at which rearrangement of the particles occurs and densification begins were not determined, and are said only to have occurred below 400°C. T_1, T_2 and T_3 identified in Figure 47, represent stages during sintering where shifts in densification behaviour were observed. To define these points more clearly, they are shown in Figure 48 along with the densification rate for 78 vol. % Fe-B_4C sintered at 1100°C.

T_1 occurred in each of the composites sintered as seen in Figure 47 (a,b and c). From Figure 48 it is clear that T_1 marks an area during sintering where a sudden increase in densification rate was observed, which at T_1, slows and proceeds at a rate slower than before T_1. Densification continues at this rate up to T_2, where densification begins to slow and appears to be ending. Densification after T_2 tends to plateau with densification rates after this point being very low (Figure 48), indicative of the end of densification.

It is evident in Figure 47 (a) that densification curves for composites sintered at 900°C differ from those at higher sintering temperatures Figure 47 (b and c), where a third point of interest (T_3) after the apparent end to densification at T_2 is shown. T_3 is indicative of the end of rapid densification in Figure 47 (b and c), with densification rates after this point being low. The shift in densification between T_2 and T_3 was an effect of changing the heating rate; this is clear in Figure 48, where the change in densification corresponds to the change in current being applied, when the sintering temperature was reached. Densification in each composite plateaued at the final sintering temperature, marking the end of densification.

Although the densification trend and identified points of interest throughout this composition range were similar, the effect of composition on densification was clear; particularly at 900°C where 69.3 vol. % Fe-B_4C composite showed < 90 % densification relative to the 78 and 80.9 % Fe where densification was above 95 % (Figure 47 a). The difference in densification between compositions lessened with increasing temperature, as densification of the 69.3 % Fe-B_4C composites improved (Figure 47 b and c).

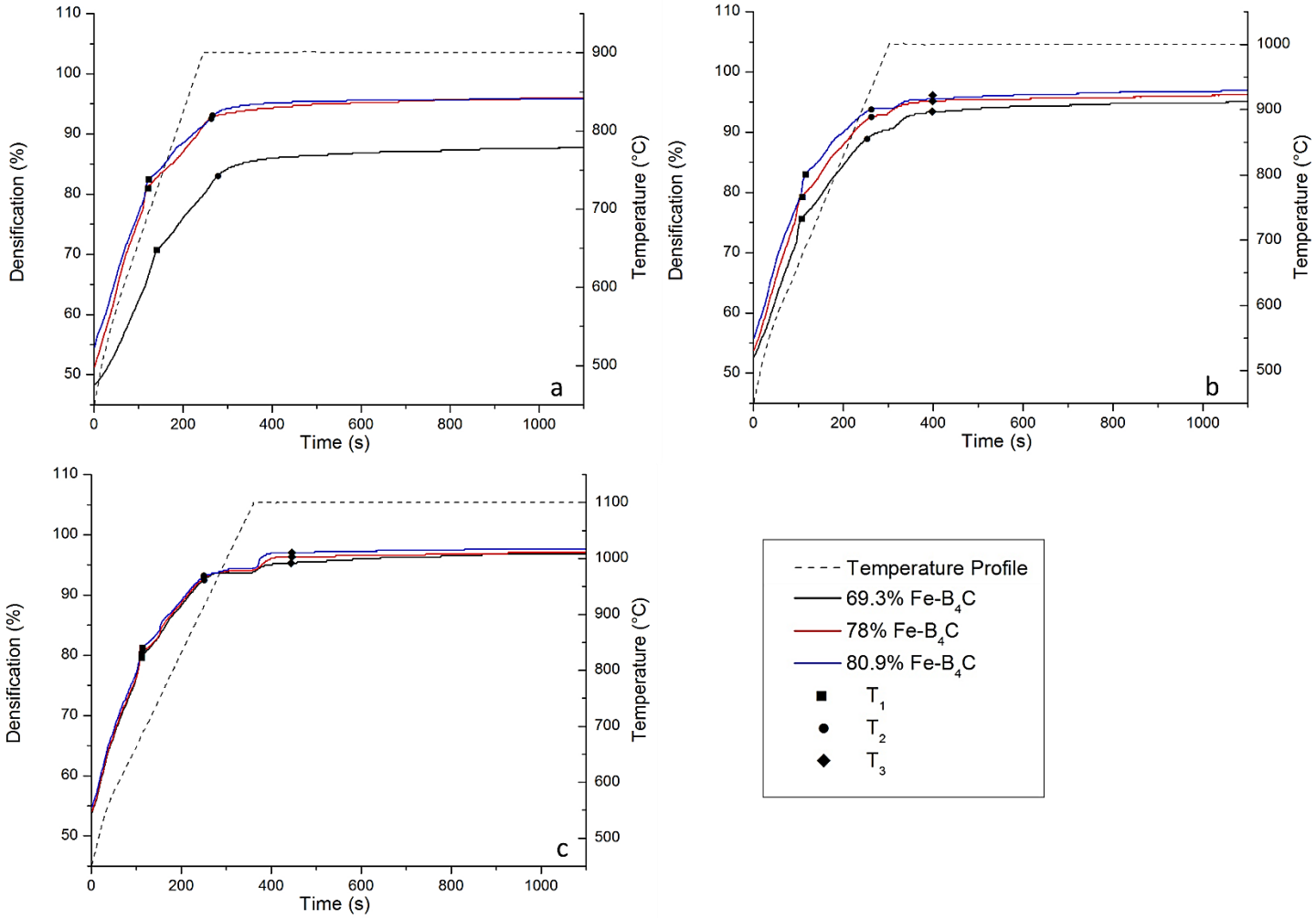


Figure 47: Densification curves for 69.3, 78 and 80.9 vol. % Fe-B_4C composites sintered at a) 900°C, b) 1000°C and c) 1100°C.

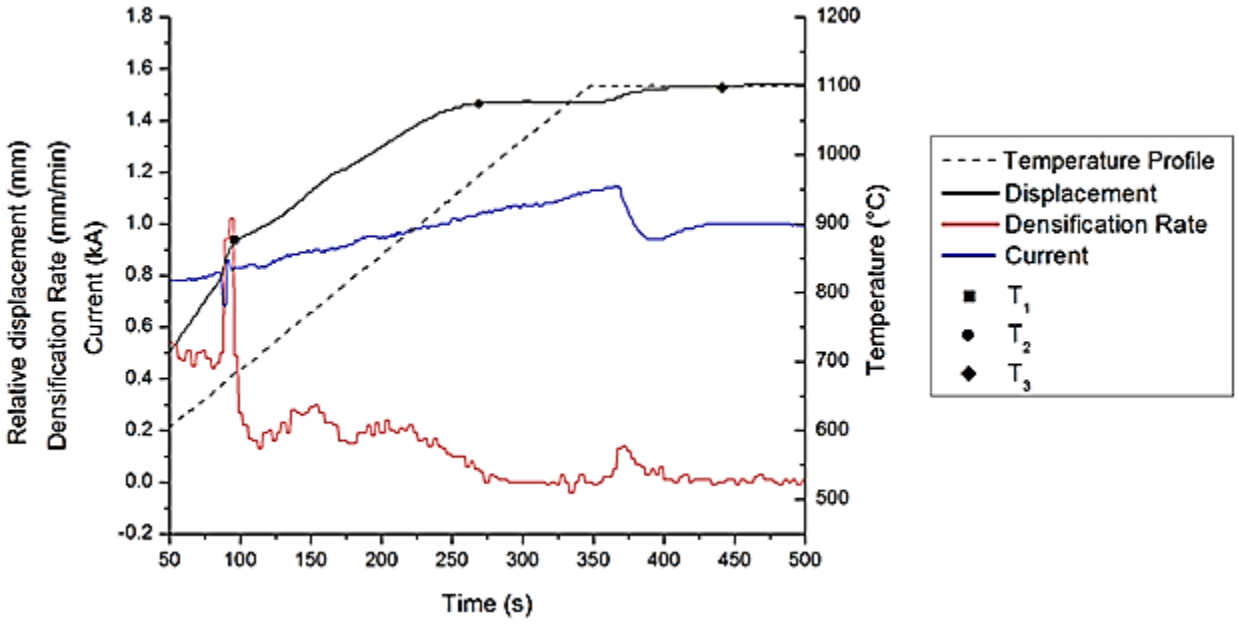


Figure 48: Densification curve for 78 vol. % Fe-B_4C sintered at 1100°C and 60 MPa, with densification rate and applied current during sintering.

Figure 49 compares the points observed relative to the temperature at which they occur. T_1 was observed between 680 and 720°C and was likely the result of Fe and B_4C reacting.[5, 147] From Figure 48, the sintering data at T_1 shows a drop in the current being supplied, suggesting the occurrence of an exothermic reaction; however, there were no accompanying spikes in temperature to substantiate this as had been observed by Laszkiewicz-Łukasik et al.[148] where exothermic reactions took place during SPS sintering.

For a given composition, the temperature at T_1 should be the same for all three sintering temperatures. It is clear from Figure 49 that this was not the case, temperature at T_1 varied, with the biggest variation over a 40°C range observed for the 69.3 % Fe-B_4C composites. The deviation is an indication of the reproducibility of the results, and is caused by the lack of control in temperature when heating up to 400°C where the pyrometer is able to read temperature. From 400°C the system aims to correct itself to match the required heating rate; thus, variations in the initial heating rates of different samples resulted in temperature deviations around T_1. The effect is less noticeable at T_2, due to more stable control in the system at higher temperatures.

In composites sintered at 900°C, point T_2 was observed shortly after the sintering temperature was reached. In the remaining composites, subjected to higher temperatures, T_2 occurred between 910 and 920°C. T_3 present in the composites sintered at 1000 and 1100°C marked the end of densification at the respective sintering temperatures. The sintering temperature – pressure combination, for these compositions in this work, was restricted to 1100°C and 60 MPa as liquid phase, formed between 1000 and 1100°C,[80, 149] losses were observed when attempting to sinter at higher temperatures and pressure.

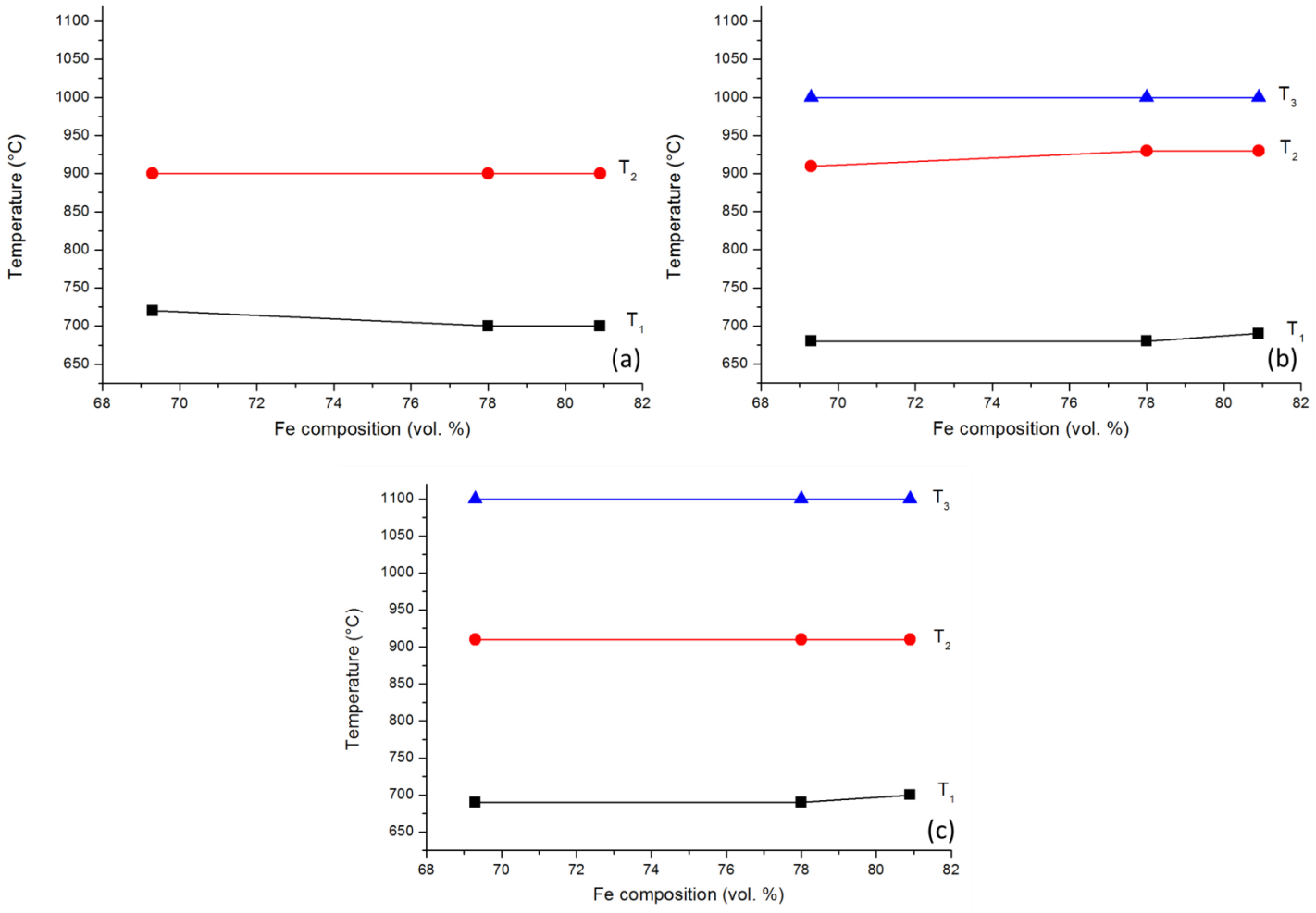


Figure 49: Comparison of densification points of interest (T_1, T_2 and T_3) when sintering at a) 900°C, b) 1000°C and c) 1100°C.

The densification during sintering of the composites with low Fe additions to B_4C (Table 9) was studied and the densification curves shown in Figure 50 (a). Indicated on Figure 50 (a) are again the points of interest during the densification process; labeled T_A, T_B, T_C and T_D. The densification rate curve for 5 vol. % Fe-B_4C is shown in Figure 50 (b) to better illustrate the behavior identified at T_A, T_B, T_C and T_D.

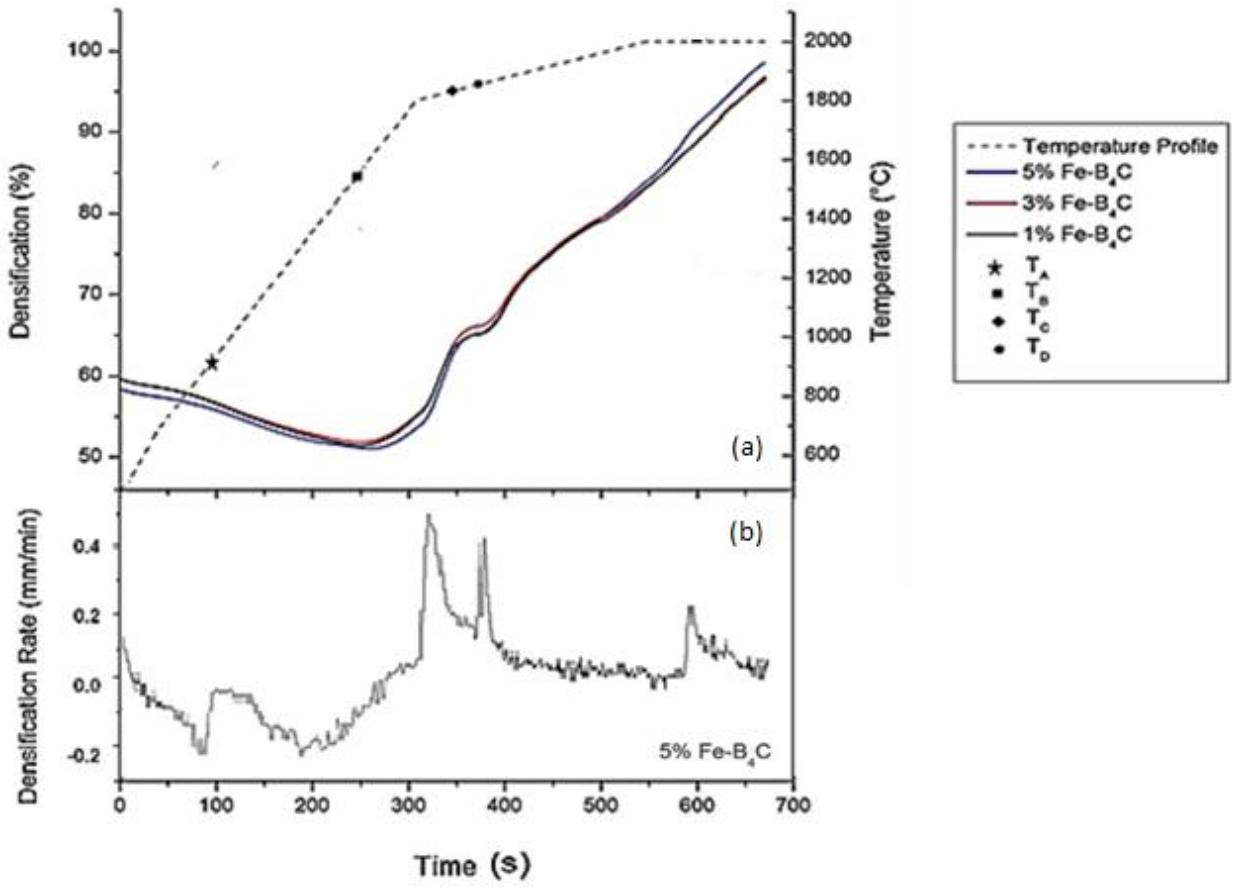


Figure 50: a) Densification curves for 1, 3 and 5 vol. % Fe-B_4C composites sintered at 2000°C and 30 MPa, with b) densification rate of 5 vol. % Fe-B_4C.

T_A observed at ≈ 940°C, showed a very small change in the densification trend as the material is heated. As with the high Fe compositions discussed previously in Figure 47 and Figure 49, this is indicative of the Fe and B_4C reacting with each other causing the slight shift in the expansion behaviour. It was clear from the densification rate curve of 5 vol. % Fe-B_4C in Figure 50 (b) that

up to T_B, piston displacement is controlled by expansion of the graphite die, with densification below 0 mm/min. T_B, at ≈ 1550°C, relates to the initial onset of densification; rearrangement of particles takes place and is considered the starting point of densification.

As the temperature increases from T_B, there is a zone of rapid densification up to T_C at ≈ 1820°C where the densification rate drops in line with changing the heating rate Figure 50 (a and b). This suggests the formation of a transient liquid phase, as a result of the iron boride phase produced through the interaction of Fe with B_4C, which promotes densification in this range.[69] The densification results are similar to those obtained by Frage et al.[69], they differ from T_B, where in this work the heating rate was decreased from 250 to 50°C/min at 1800°C up to the final sintering temperature, while in work by Frage et al, heating was constant and points T_C and T_D were observed on a smaller scale at a temperature < 1800°C.

From T_D (≈ 1880°C) the densification rate improves again as interactions between B_4C particles begin to affect densification. These interactions are promoted in the presence of the iron rich liquid phase increasing densification. Similarities in the densification curves in Figure 50 (a), with 1 and 3 % Fe-B_4C being almost identical above 1100°C, was a result of smaller composition variations (Table 12) due to Fe contamination from the milling media.

5.2.1. Theoretical density and composition analysis

Typically, theoretical density would be calculated as per equation 21; where the theoretical density of each individual powder component relative to their respective composition determines the theoretical density.

$$\frac{1}{\rho} = \sum_{i=1}^{n} \frac{x_i}{\rho_i} \qquad \text{Equation 21}$$

Where;

ρ = Calculated Theoretical Density of the Material (g/cm^3)

x_i = Mass Fraction of Material i

ρ_i = Theoretical Density of the Material i (B_4C = 2.51 g/cm^3 [2], Fe = 7.86 g/cm^3 [150] and Ti = 4.51 g/cm^3 [151])

Due to the reaction of boron carbide with the iron during sintering, determining the theoretical density from the powders using equation 21 was not suitable. Thus, porosity and relative density were determined using image analysis as laid out in the experimental procedure (chapter 3.2.1). As a result, the suggested theoretical density of each composite was determined using the measured density (Table 8 and Table 9) with respect to the relative density attained as per equation 22, and displayed in Table 13 and Table 14.

$$\rho_{T,S} = \frac{\rho_{Bulk}}{\rho_{Rel}} \qquad \text{Equation 22}$$

Where;

$\rho_{T,S}$ = Theoretical Density of Sintered Material (g/cm^3)

ρ_{Bulk} = Measured Bulk Density of Sintered Material (g/cm^3)

ρ_{Rel} = Relative density (%)

Table 13 and Table 14 showed the densities, calculated using equation 21, of the respective starting powder compositions, the compositions after mixing (accounting for contamination - Table 7), as well as the measured density of the sintered composites.

The observed densities for high vol. % additions to B_4C (Table 13) were greater than those of the starting powder mixture. Although the absolute and relative density of the composites increased with increasing sintering temperature, the suggested/inferred theoretical density decreased. Similarly, longer sintering times saw a decrease in suggested theoretical density calculated for the 69.3 % Fe-B_4C composites sintered at 1000°C for 2, 5 and 15 min. These observations are suggestive of the phases formed during sintering and their evolution with temperature and sintering hold time, and demonstrate the extent of deviation in suggested theoretical density,

from that of the powder, caused by the reactions. From Table 13 it is clear that theoretical density deviations relative to the starting powder increased with increasing B_4C content where the largest difference of 1.16 g/cm^3 is observed.

Table 13: Comparison of theoretical density of pre-mixed and mixed powder components to the sintered composites with high vol. % additions to B_4C.

Sample (vol. %)	Pre-mixed Powder Density (g/cm^3)	Mixed Powder Density (g/cm^3)	Sintered Composite				
			Temperature (°C)	Absolute Density (g/cm^3)	Porosity from Image Analysis (%)	Relative Density (%)	Suggested Theoretical Density (g/cm^3)
80.9% Fe-B_4C	6.84	6.86	900	7.26	3.9±0.1	96.1±0.1	7.55±0.01
			1000	7.27	3.0±0.1	97.0±0.1	7.49±0.01
			1100	7.29	2.1±0.2	97.9±0.2	7.45±0.02
78% Fe-B_4C	6.68	6.71	900	7.23	4.0±0.7	96.0±0.7	7.53±0.05
			1000	7.25	3.7±0.5	96.3±0.5	7.53±0.04
			1100	7.27	2.9±0.2	97.1±0.2	7.49±0.02
69.3% Fe-B_4C	6.22	6.25	900	6.51	12.2±0.9	87.8±0.9	7.41±0.08
			1000	6.76	4.9±0.2	95.1±0.2	7.11±0.01
			1100	6.8	2.9±0.1	97.1±0.1	7.00±0.01
			1000 (2 min)	6.73	7.5±0.7	92.5±0.7	7.28±0.06
			1000 (5 min)	6.74	6.2±0.3	93.8±0.3	7.19±0.02
80.9% (0.8Fe+0.2Ti)-B_4C	6.3	6.32	900	6.7	4.1±0.2	95.9±0.2	6.99±0.01
			1000	6.87	2.5±0.1	97.5±0.1	7.05±0.01
			1100	6.9	1.7±0.4	98.3±0.4	7.02±0.03
78% (0.8Fe+0.2Ti)-B_4C	6.16	6.19	900	6.55	5.4±0.6	94.6±0.6	6.92±0.04
			1000	6.82	2.4±0.1	97.6±0.1	6.99±0.01
			1100	6.9	1.4±0.1	98.6±0.1	7.00±0.01
69.3% (0.8Fe+0.2Ti)-B_4C	5.75	5.79	900	5.81	7.3±0.6	92.7±0.6	6.27±0.04
			1000	6.04	3.9±0.5	96.1±0.5	6.29±0.03
			1100	6.2	2.8±0.2	97.2±0.2	6.38±0.01

Table 14 shows the density values of the 1-8 vol. % additions to B_4C were typically smaller than the mixed powder density. The suggested theoretical densities in Table 14 were greater than those of the mixed powder prior to sintering. Unlike the high additions to B_4C in Table 13, where sintering temperature had an effect on the theoretical density as a result of phase changes during sintering, sintering temperature had little to no effect on theoretical density in Table 14. This

suggests Fe in the starting powder reacted fully with B_4C below the sintering temperature. Composition had a small effect on theoretical density, due to small changes in composition associated with the sintered powder.

Table 14: Theoretical density of pre-mixed and mixed powder components for 1-5 vol. % additions to B_4C.

Sample (vol.%)	Pre-mixed Powder Density (g/cm^3)	Mixed Powder Density (g/cm^3)	Sintered Composite			
			Temperature (°C)	Absolute Density (g/cm^3)	Relative Density (%)	Suggested Theoretical Density (g/cm^3)
5% Fe-B_4C	2.78	2.82	1900	2.71	95.4±0.5	2.84±0.02
			1910	2.72	96.3±0.3	2.82±0.01
			2000	2.79	98.4±0.2	2.83±0.01
3% Fe-B_4C	2.67	2.79	1900	2.61	91.2±0.7	2.86±0.03
			1910	2.71	96.3±0.2	2.82±0.01
			2000	2.74	97.6±0.4	2.81±0.02
1% Fe-B_4C	2.56	2.75	1910	2.58	92.7±0.4	2.78±0.02
			2000	2.73	97.7±0.5	2.79±0.02
5% (0.8Fe+0.2Ti)-B_4C	2.74	2.78	1910	2.66	95.5±0.5	2.79±0.02
			2000	2.74	97.9±0.3	2.80±0.01
3% (0.8Fe+0.2Ti)-B_4C	2.65	2.74	1910	2.71	96.9±0.2	2.79±0.01
			2000	2.73	97.4±0.2	2.80±0.01
1% (0.8Fe+0.2Ti)-B_4C	2.56	2.71	1910	2.67	95.9±0.6	2.79±0.02
			2000	2.70	97.6±0.2	2.77±0.01
5% Ti-B_4C (Fe Balls)	2.61	2.65	1910	2.53	94.8±0.2	2.67±0.01
			2000	2.54	95.1±1.0	2.68±0.04
3% Ti-B_4C (Fe Balls)	2.57	2.66	1910	2.48	92.9±0.1	2.67±0.01
			2000	2.59	95.6±0.2	2.71±0.01
1% Ti-B_4C (Fe Balls)	2.53	2.67	1910	2.53	92.3±0.4	2.74±0.02
			2000	2.68	96.9±0.1	2.76±0.00
5% Ti-B_4C (WC Balls)	2.61	2.90	1910	2.87	95.2±0.2	3.01±0.01
			2000	2.93	97.2±0.5	3.02±0.02
8% Ti-B_4C (WC Balls)	2.67	2.94	1910	2.91	95.2±0.2	3.06±0.01
			2000	2.96	96.7±0.3	3.06±0.01

To better comprehend the changes in theoretical density shown in Table 13 and Table 14, the phases produced during sintering were assessed. Table 15 gives the phases identified through

XRD and EDX analysis in section 4.2.2 and 4.3.2 for each of the Fe-B_4C composites. The phases expected to be present from the Fe-B-C equilibrium phase diagrams in Figure 10(chapter 2.3.2)and from ASM Alloy Phase Diagram Center - Diagram No's: 2000010, 2000009, 2000362 [90, 91], in conjunction with phase data from Rogl et al.[149] and Hasebe et al.[81], are also shown in Table 15. This allowed for better understanding of the phases formed.

Table 15: Phases present in sintered Fe-B_4C composites (X = observed, E = expected from phase diagrams[81,90,91,151]).

Sample	Temperature (°C)	Products							
		Fe_2B	**FeB**	**$Fe_3(B,C)$**	**$Fe_{23}(B,C)_6$**	**Fe**	**C**	**B_4C**	**L**
80.9% Fe-B_4C	900	E-X		E-X	X	X	X		
	1000	E-X		E-X	X	X			
	1100	E-X		X					E
78% Fe-B_4C	900	E-X		E-X	X		X		
	1000	E-X		E-X	X		X		
	1100	E-X		X	X		X		
69.3% Fe-B_4C	900	E-X	E-X	X			E-X		
	1000	E-X	E-X	X			E-X		
	1100	X	E-X	X			X		E
5% Fe-B_4C	1900 - 2000		E-X					E-X	E
3% Fe-B_4C	1900 - 2000		E-X					E-X	E
1% Fe-B_4C	1910, 2000		E-X					E-X	E

From the high Fe containing composites in Table 15 and observations of their microstructures (chapter 4.2.2), the two most prevalent phases formed were; Fe_2B and the metastable Fe_3C type phase with some residual carbon. Reaction 3 and 4 (mentioned in chapter 4.2.1 and shown again), correlate to the starting composition of the 78 and 69.3% Fe-B_4C compositions; however, observations in Table 15 suggest reactions 3 and 5 were the main reactions that took place during sintering.

$$11Fe + B_4C = 4Fe_2B + Fe_3C \qquad \text{Reaction 3}$$

$$7Fe + B_4C = 4FeB + Fe_3C$$ Reaction 4

$$8Fe + B_4C = 4Fe_2B + C$$ Reaction 5

Reaction 4 was expected for the 69.3% Fe-B_4C, corresponding to a 7Fe:1B_4C mole ratio, where FeB would have been the predominant phase along with Fe_3C. However, while FeB was observed in small amounts amongst the carbon rich areas (Figure 24), the XRD data showed Fe_2B was the majority phase with very little Fe_3C (Figure 22).

B atoms are able to substitute and take the place of C atoms in the Fe_3C lattice. As a result, the Fe_3C phase observed was a metastable $Fe_3(B,C)$ solid solution phase.[81] Similarly, the metastable $Fe_{23}(B,C)_6$ phase was observed in the sintered materials in much smaller quantities. The presence of this phase differs from that of the $Fe_3(B,C)$ phase in that it did not fall within the expected composition ranges on the respective equilibrium phase diagrams (ASM Alloy Phase Diagram Center - Diagram No's: 2000010, 2000009, 2000362[90]).

Due to the nature of the rapid sintering process, the phases produced are not in equilibrium. As a result, phases observed in the sintered composites (Table 15) deviate from those predicted in the Fe-B-C phase diagrams. The other consideration is the crystallization of the liquid phase during cooling, and the subsequent phases formed. According to the partial reaction scheme within the metastable phase range, compiled by Rogl et al.[149], the possible phases produced during the crystallization of the liquid phase are γ-Fe, Fe_2B and $Fe_3(B,C)$; the phase composition being dependent on the starting Fe-B-C composition. $Fe_{23}(B,C)_6$ is formed between 800 and 965°C, and decomposes into γ-Fe and $Fe_3(B,C)$ at higher temperatures. $Fe_{23}(B,C)_6$ has the potential to precipitate during cooling, but is not stable below 800°C.[149]

When observing the microstructures (chapter 4.2.2) of the high Fe containing composites in Table 15, it was clear that although reactions 3 and 5 relate to the relevant phases, the stoichiometry was not representative of the sintered composites. Analysis of the cross-sections (analysed in the same manner as porosity, described in chapter 3.2.1) allowed for approximations of the respective amounts of Fe_2B and $Fe_3(B,C)$ formed during sintering, as shown in Table 16. It is evident from Table 16 that the combination of Fe_2B and $Fe_3(B,C)$ made up the majority of

the phases produced, responsible for over 90% of the total phases observed in all but one case; the 80.9% Fe-B_4C sintered at 1000°C where ≈ 80 vol. % of the phases were Fe_2B and $Fe_3(B,C)$. This was expected, as observations of the microstructure (Figure 18) show it as the composite with the greatest $Fe_{23}(B,C)_6$ presence (estimated at ≈ 19 vol. %).

Table 16: Microstructure analysis of the amounts of Fe_2B and $Fe_3(B,C)$ in the matrix and relative to each other.

Sample	Temperature (°C)	Composition of total phases (excl. porosity) made up by $Fe_2B/Fe_3(B,C)$ (Vol.%)	Volume Fe_2B:Fe_3B (%)		Molar ratio Fe_2B:$Fe_3(B,C)$	
			Fe_2B	$Fe_3(B,C)$	Fe_2B	$Fe_3(B,C)$
80.9% Fe-B_4C	900	96.8	31	69	1.0	1.5
	1000	80.1	49	51	1.0	0.7
	1100	99.9	20	80	1.0	2.9
78% Fe-B_4C	900	97.1	46	54	1.0	0.8
	1000	97.8	44	56	1.0	0.9
	1100	96	48	52	1.0	0.8
69.3% Fe-B_4C	900	97.5	65	35	1.0	0.4
	1000	90.8	80	20	1.0	0.2
	1100	92.3	48	52	1.0	0.8

From the phase diagrams (ASM Alloy Phase Diagram Center - Diagram No's: 2000010, 2000009, 2000362[90]) the Fe_2B:$Fe_3(B,C)$ molar ratio was estimated, using the tie-line rule,[152] to be between 1:0.3 and 1:0.4 for the 78 and 80.9 vol. % Fe-B_4C composites, while the presence of $Fe_3(B,C)$ is not suggested for 69.3 % Fe-B_4C. Comparing these ratios to those observed in Table 16 is indicative of the deviations from equilibrium; showing a greater $Fe_3(B,C)$ presence than would be expected at equilibrium, in each of the composites.

Using these products, an estimation of the reaction free energies was determined and shown in Figure 51. The free energies of the Fe_2B-$Fe_3(B,C)$ products (Table 16) were calculated using thermodynamic data from Ohtani et al.[153] relative to the initial Fe-B_4C compositions shown in Table 17. Free C and $Fe_{23}(B,C)_6$ were not considered in the estimation, thus the reactions were balanced using the molar ratios shown in Table 16 and Table 17,

Table 17: High Fe-B_4C mixed powder molar composition.

Sample	Post mixing Fe:B_4C mole ratio
80.9 vol. % Fe-B_4C	13.45 : 1
78 vol. % Fe-B_4C	11.26 : 1
69.3 vol. % Fe-B_4C	7.18 : 1

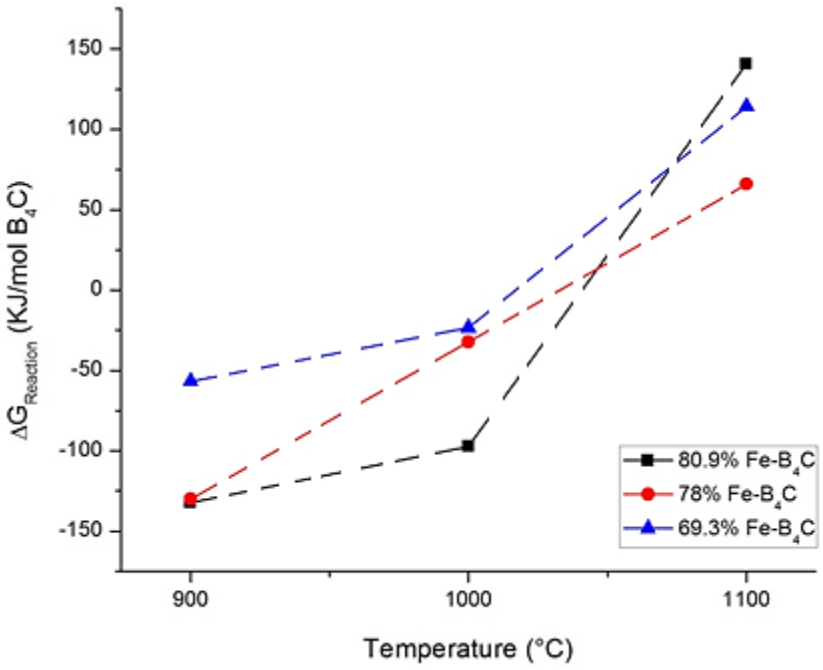


Figure 51: Estimation of reaction free energy from Fe_2B-$Fe_3(B,C)$ compositions.

The reaction free energy of the high Fe-B_4C samples, in Figure 51, increases with increasing temperature. This suggests that the higher temperatures are responsible for the production of the least stable combination of phases during sintering. An iron rich liquid phase begins to form at 1097°C according to Rogl et al.[149], which will solidify during cooling. The cooling parameters

implemented will determine the nature of the phases produced, with faster cooling rates more likely to trap metastable phases precipitated during cooling.[154]

Free energies of formation calculated from thermodynamic data provided by Ohtani et al.[153] (for: Fe, Fe_xB_y and Fe_3C) and from thermodynamic data supplied by Mintek (South Africa) using THERMO software (for: B_4C) are shown in Figure 52. It is evident that the formation energy of iron borides increases with increasing iron content, while the iron carbide phases have the highest formation energies. The $Fe_x(B,C)_y$ phases form through the substitution of C with B, thus the Fe_3C and $Fe_{23}C_6$ phases form first.[81] Fe_3B has been produced directly for similar compositions Lomovsky et al.[155]; however the cooling rates were significantly faster with laser heating being implemented.

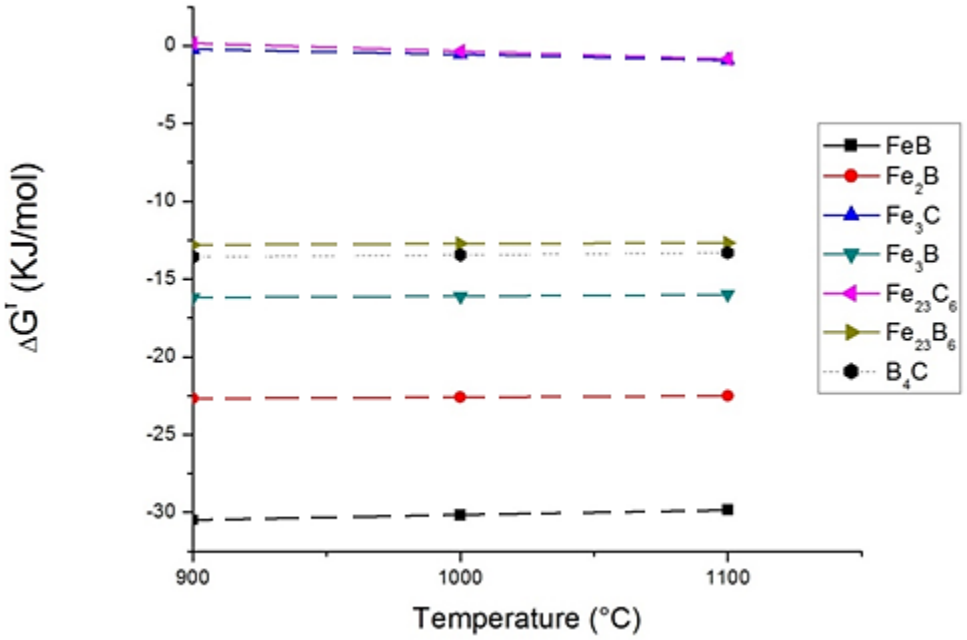


Figure 52: Free energy of formation of Fe_xB_y and $Fe_a(B,C)_b$ phases at 900, 1000 and 1100°C.

The free energies of reactions 3, 4 and 5 were calculated using thermodynamic data provided by Mintek (South Africa) and shown in Figure 53, where it is evident that the free energies of reaction 3 and 5 are relatively similar with free energies fluctuating < 10 kJ/mol with increasing temperature from 900 to 1100°C. Reaction 4 is shown in Figure 53 to have the lowest Gibbs free energy decreasing with increasing temperature to ≈ 660 kJ/mol at 1100°C.

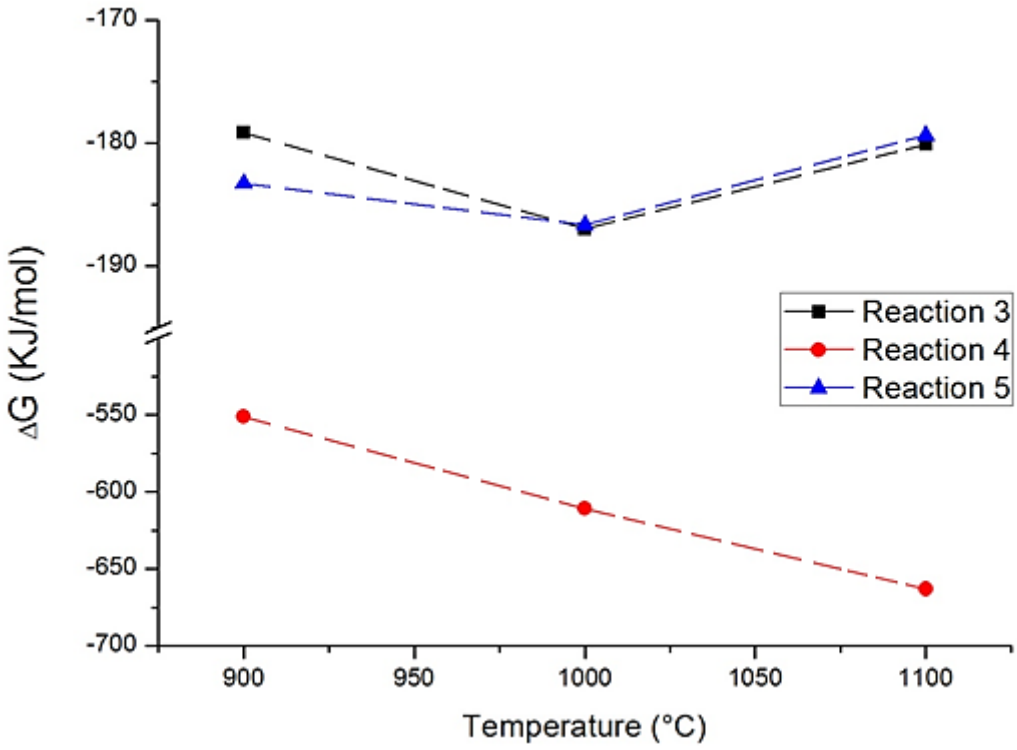


Figure 53: Reaction free energy at 900, 1000 and 1100°C for reactions 3, 4 and 5.

Comparing the estimated reaction free energies determined in Figure 51 to those of the suggested reactions taking place in Figure 53 it is seen that the estimated free energies are greater than those from the reactions. Reaction 3 relates to the same product combination, Fe_2B and Fe_3C, in Figure 51 and shows a difference of ≈ 50 kJ/mol at 900°C for the 78 and 80.9 % Fe-B_4C. However, the difference increased as temperature increased, additional evidence that the reactions taking place in the SPS are not at equilibrium, with free energies > 0 kJ/mol at 1100°C in Figure 51.

It was clear from the phases observed in the microstructure of the sintered material, that even with rapid heating and cooling rates, B_4C completely reacted with Fe and therefore, only brittle phases could be formed. The fast reaction rates between B_4C and Fe, have been noted previously by Terry et al.[156] where B_4C was added to a Fe melt and quenched, but still reacted completely.

Composites containing 1 to 5 vol. % Fe additions also underwent reactions during the sintering process (Table 15). The main phases present in each of the sintered compounds were unreacted B_4C and FeB, which is in agreement with the phase diagram shown by Aizenshtein et al.[91] (Figure 10, chapter 2.3.2). This suggests the iron added reacts with B_4C as per reaction 6. The free energy of reaction 6 was determined to be -144.6 and -136.9 kJ/mol at 1910 and 2000°C respectively.

$$4Fe + B_4C = 4FeB + C \qquad \text{Reaction 6}$$

The amount of the FeB present was determined using image analysis (analysed in the same manner as porosity, described in chapter 3.2.1), and by calculating the FeB produced through reaction 6. The results were compared to each other in

Table 18, along with the resultant relative density of the composites (equation 22) and that determined through cross-sectional analysis of the porosity (from Table 14).

Table 18: Comparison of low Fe-B_4C phase compositions and corresponding theoretical densites calculated using reaction 6 and analysis of the cross-section.

Sample	Measured ρ (g/cm^3)	Relative Density (Table 14) (%)	Suggested Theoretical ρ (g/cm^3)	Reaction		Cross-section Analysis	
				FeB (Vol. %)	$\rho_{(TR)}$ (g/cm^3)	FeB (Vol. %)	$\rho_{(TI)}$ (g/cm^3)
5% Fe-B_4C	2.79	98.4±0.2	2.83±0.01	7.9	2.84	7.9±0.1	2.85
3% Fe-B_4C	2.74	97.6±0.4	2.81±0.02	7.1	2.81	7.2±0.1	2.82
1% Fe-B_4C	2.73	97.7±0.5	2.79±0.02	6.1	2.77	6.6±0.2	2.79

* Note – the quantity of FeB measured using image analysis included impurities present within the phase.

Comparing the amounts of FeB that would be expected from the reaction of B_4C with Fe to the amount observed through image analysis in

Table 18, the values were similar for the 3 and 5 % Fe-B_4C composites. Analysis of the cross-section at 1% suggests the composite contained ≈ 0.5 % more FeB than was expected when considering the reaction. The difference may be accounted for within the errors of the various measurements required to produce these results; user dependence in cross-section analysis and typical measurement errors in determining the weight loss of the milling media to account for

starting composition. There was little evidence of free carbon at the boundary of FeB and B_4C with EDX analysis suggesting the majority was in solution with the FeB. Free carbon that was present at the grain boundary may have been pulled out during polishing and subsequently not identified. Munhollon et al.[157] showed the sensitivity of free carbon to pull-out in B_4C ceramics, while Aizenshtein et al.[91] showed the presence of graphite at the reaction interface for Fe reacting with B_4C.

Quantification of the FeB phase allowed for the theoretical density of the materials to be calculated. The theoretical densities determined from the FeB products, $\rho_{(TR)}$ and $\rho_{(TI)}$ (

Table 18), were in agreement with those in Table 14, indicating the image analysis of cross-sectional areas was sufficient in determining densification and corresponding relative density.

The effect of replacing 20% of the Fe in the composites with Ti was observed (chapter 4.2.2.4 and 4.3.2.3). In the additions ≥ 69.3 % to B_4C, while Fe_2B and $Fe_3(B,C)$ remained the majority phases, XRD analysis (Figure 25) showed the presence of TiC which through SEM and EDX analysis (Figure 27) was observed to be surrounding a TiB phase with a small amount of iron in solution. This was most evident in the 78 and 80.9% (0.8Fe+0.2Ti)-B_4C composites while the addition of Ti to the 69.3 % composite did not improve the presence free carbon within the microstructure (Figure 26).

Additions of the Fe-Ti mix ≤ 5 % to B_4C showed the presence of a TiB_2 phase amongst the FeB. As with the Fe only additions, WC contamination from the milling pot was observed and seen to coalesce as inclusions within the FeB-TiB_2 pools (Figure 32). The comparison of Ti additions to B_4C mixed using steel balls and those mixed with WC balls showed significant differences in the phases observed and the extent to which additional Fe picked up during milling affects the phase composition. Where Fe milling balls were used, the dispersion of an FeB phase throughout the TiB_2 phase was evident. Significant WC contamination (Table 7) when using WC milling balls resulted in the interaction of Ti with WC to produce TiB_2 and $(W,Ti)_XB_{3-X}$ phases (Figure 34).

5.2.2. Temperature and composition effects on densification

The dependence of relative density on sintering temperature for the 69.3, 78 and 80.9 vol. % Fe-B_4C systems (Table 8) is shown in Figure 54. It is evident that increases in sintering temperature corresponded to increased densification in each of the composites. From Figure 54 it is clear that iron composition had a significant influence on densification at 900°C, where there was a densification difference of ≈ 8 % between 69.3 % Fe-B_4C and the 78 and 80.9 % Fe-B_4C composites. This difference decreased with increasing temperature, and at 1100°C, the relative density of the 69.3 and 78 % Fe-B_4C were comparable. There was no significant difference in densification between the 78 and 80.9% Fe-B_4C at 900°C however; sintering at 1000 and 1100°C produced higher relative densities in 80.9 % Fe-B_4C (≈ 1 % at 1100°C).

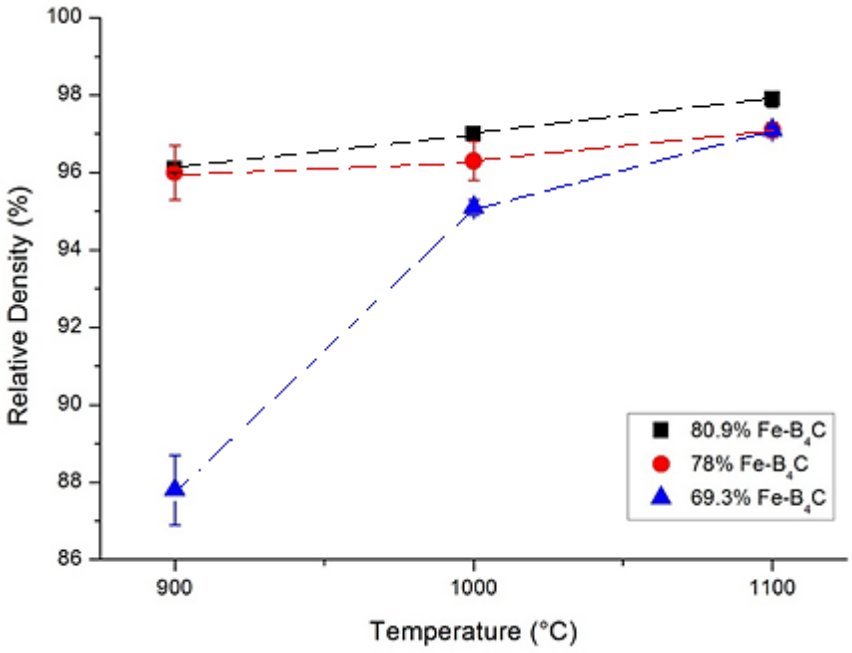


Figure 54: a) Effect of sintering temperature on densification in 69.3, 78 and 80.9% Fe-B_4C composites sintered at 60 MPa.

The influence of sintering temperature on densification was most prominent in the 69.3% Fe-B_4C composites (Figure 54), where a relative density increase of ≈ 9 % was observed between 900 and 1100°C. Taking into account the measurement error observed, there were very slight

densification changes in the 78 % Fe-B_4C while a small but noticeable increase was observed for 80.9 % Fe-B_4C.

The density results tend to plateau suggesting further temperature increases would produce little to no improvements in densification results. Further temperature increases were however limited due to the formation of an iron rich liquid phase, as mentioned in chapter 5.2.1.

Although densification above 97% was achieved for each of the compositions when sintering at 1100°C, the fine dispersion of porosity was observed in all the sintered composites (Figure 18, Figure 21 and Figure 23). Corresponding to the increased densifications, the amount of porosity decreased as the temperature increased; however, this was accompanied by pore growth along with grain growth in the microstructure at 1100°C.[158] This was most notable in Figure 18 c), the 80.9 % Fe-B_4C composition, where sintering at 1100°C resulted in the largest grains (up to 10 µm) and several pores in excess of 3 µm.

Observing the microstructures in Figure 18, Figure 21 and Figure 23, grain size typically ranged between 1 and 2.5 µm, which was smaller than the initial starting powder sizes of < 10 µm for the B_4C and 1-10 µm for iron (Table 3). As a result, it is clear that the reaction sintering process facilitates the precipitation of a fine grained product, when using spark plasma sintering. The dispersion of porosity within the microstructure when sintering Fe rich composites with additions of B_4C was a result of the dissolution of boron carbide particles in contact with the iron matrix.[9]

From Table 8, it is evident that substituting titanium for 20 % of the iron resulted in a very small improvement in densification when sintering at 1000 and 1100°C where densification > 98% was achieved for 78 and 80.9 % (0.8Fe+0.2Ti)-B_4C composites. The fine porosity observed in the Fe only composites appeared to be improved however, the porosity observed was large, irregular and at the grain boundaries resulting in areas where there was no bonding between grains.

The effect of iron content from 1 to 5 % with B_4C in the starting powder is shown in Figure 55. It is clear that at 1910°C densification improved by more than 3 % with increasing iron content from 1 to 3%. Improved densification with increasing Fe relates to larger quantities of the transient FeB liquid phase enhancing densification.[69, 91, 158] Further Fe increases to 5% showed

no additional improvement in densification although a small decrease in open porosity was observed (Table 9). Increasing temperature to 2000°C saw significant improvement in densification, relative to the respective compositions at 1910°C, with over 97 % densification achieved for each composition. Considering the error, there was very little change in densification with increasing composition at 2000°C, although the 5 % Fe did appear to attain the best densification result.

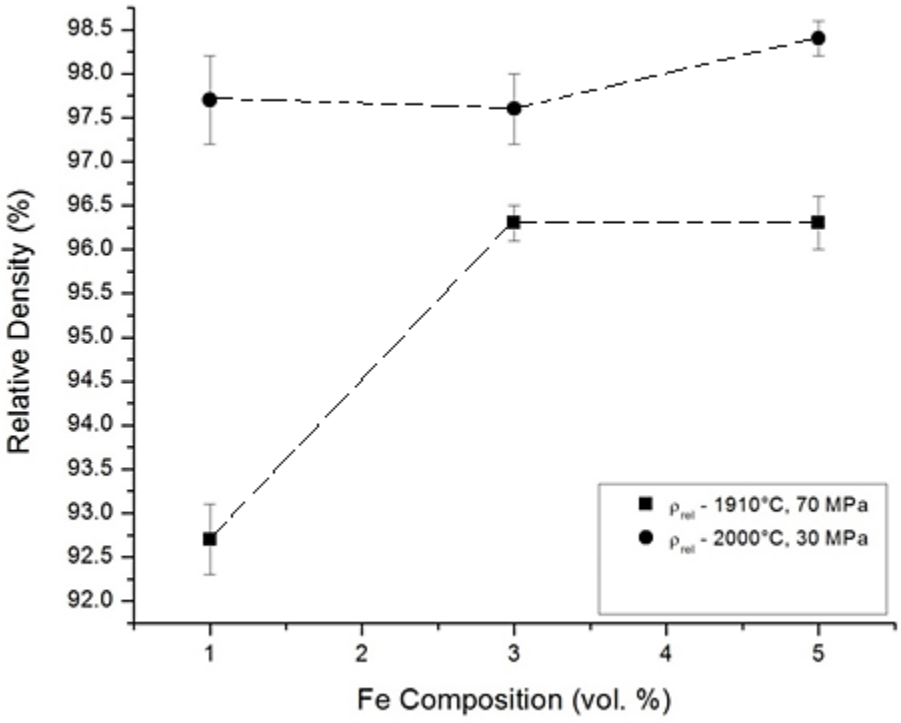


Figure 55: Effect of increasing Fe content from 1 to 5 vol. % in the starting powder on densification and open porosity when sintering at 1910°C and 2000°C.

Observing the microstructure and the porosity therein (Figure 29), it was evident that there were areas of pull out. The FeB phase, with sections up to 8 µm, showed evidence of cracking and pulling away from the B_4C interface. This was a result of the differences in the thermal expansion coefficients and the subsequent stresses induced as a result of the mismatch. Frage et al. observed similar effects in B_4C with 5.5 % Fe and determined the radial and tangential stress to be greatest at the interface and greater than the FeB-B_4C bond strength.[69] Free carbon at the

interface exacerbated pull-out by weakening the already stressed FeB-B_4C interface.[69, 157] Comparing the densification to similar compositions in literature showed comparable densification and appearances in microstructure when sintering at 2000°C and 30 MPa.[69] Relative to pure B_4C materials, shown in Table 1, a wide variety of full densification values have been suggested over a range of temperatures < 2000°C. The differences arise from the use of different types of SPS furnaces, resulting in differences in the manner in which the temperature is read.[43] Comparing B_4C sintered using the same furnace type and parameters; ≈ 1-2 % increase in densification is achieved with the addition of Fe.

The differences in heating rate may have played a small role, but, given the small variation, this is more likely differences due to the iron contamination during milling, aiding densification.

Comparing the densification results to those where Ti was added along with Fe (Table 9), it was clear that the addition of Ti did not improve densification at 2000°C. As with the Fe only additions, the best densification was achieved with the 5 vol. % addition with negligible improvements observed when increasing from 1 to 5 vol. % (0.8Fe+0.2Ti)-B_4C. Open porosity was observed to be greater than the pure iron counterparts.

The TiB_2 phase that formed was present along with the FeB and WC inclusions, and the addition to the microstructure did not improve the behavior of the FeB with B_4C. The combination of phases was still prone to cracking during cooling and the resultant pull-out during polishing. With the addition of Ti, the FeB-TiB_2 regions increased in size with sections in excess of 10 µm. Pure Ti additions showed less densification than the iron containing counterparts with the same additions to B_4C where there is no densification assistance from a liquid phase.[158]

5.2.3. Comparison of hardness and fracture toughness results

The hardness behavior of high Fe containing composites (Table 8) differed significantly between compositions, as shown in Figure 56. The 69.3 vol. % Fe-B_4C composite sintered at 1100°C had the highest hardness of 13.7 GPa, where the hardness was seen to increase with increasing sintering temperature. The maximum hardness was observed at 1000°C in the 78 and 80.9 % Fe

composites (13.2 and 10.9 GPa respectively), where unlike the 69.3 % Fe-B_4C, increasing the temperature to 1100°C resulted in a decrease in hardness. The decrease was most significant in the 78 % Fe-B_4C, although the hardness was still higher than 80.9 % Fe-B_4C which had the lowest hardness at all temperatures.

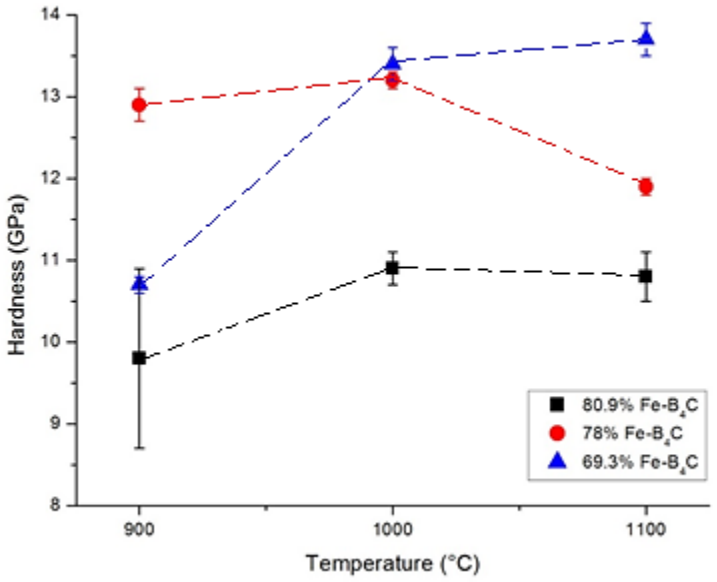


Figure 56: Relationship between temperature and hardness for high Fe additions to B_4C produced using SPS.

A hardness increase greater than 2 GPa was observed for 69.3 % Fe-B_4C in Figure 56 when increasing the sintering temperature from 900 to 1000°C corresponding to the increase in densification from 87.8 to 95.1 % and demonstrating the negative effects of poor densification on hardness.[159] Although the densification did not decrease at 1100°C for the 69.3 % Fe-B_4C composite, the change in hardness was negligible compared to 1000°C. Hardness for all the compositions increased with increasing sintering temperature to 1000°C, and was expected to increase with temperatures of 1100°C for all the compositions, corresponding with the increase in density observed in Figure 54 a). This was not the case as seen in Figure 56 for the 78 and 80.9 % Fe-B_4C whose hardness decreased significantly, indicating the dependence of hardness on additional parameters.

As mentioned in chapter 5.2.2, at 1100°C there was coalescence and growth of pores and grains. As a result, the expected increases in hardness with improved densification were negated by the presence of the larger pores and grains, with the respective effects on the hardness properties competing with each other.[159] Also, the evolution of phases at the different sintering temperatures resulted in composition variations as well as different grain size distributions at the different temperatures for each respective composition. SEM micrographs of the microstructures (Figure 18, Figure 21 and Figure 23) showed fine multiphase structures in each of the materials sintered at 1000°C. The structure at 1000°C was the most refined for each of the compositions; the finer structure along with the fine porosity was responsible for the best hardness observed for the78 and 80.9 % Fe-B_4C composites at 1000°C.[99, 100]

The type and amount of the phases present will also affect the hardness relative to the hardness of the phases present. The Fe_2B to $Fe_3(B,C)$ ratio observed in Table 16 showed the 80.9 % Fe composites contained the most $Fe_3(B,C)$ and the sample sintered at 1000°C contained ≈ 19 % $Fe_{23}(B,C)_6$. From literature it was evident that the hardness of the phases increases in the following order; $Fe_3(B,C)$, $Fe_{23}(B,C)_6$, Fe_2B and FeB.[160] As a result, where larger amount of $Fe_3(B,C)$ are observed, the hardness will decrease as is evident in Figure 56 for the 80.9 % Fe-B_4C where the highest Fe_2B:$Fe_3(B,C)$ ratios of 1:1.5 and 1:2.9 were observed, at 900°C and 1100°C respectively.

Although the phases have been ranked in this manner, observing data from literature it was clear that the hardness values quoted for these phases overlap significantly. As mentioned in chapter 2.3.2, the hardness of the phases produced in Fe-B-C composites ranged from 7 – 22 GPa.[10, 78, 82-88] The hardness values achieved for the composites shown in Figure 56 fall within this range, suggesting little difference in the hardness when using SPS to sinter the Fe-B-C materials. It must be noted however, the majority of the hardness values from literature used indentation loads as low as 0.1 N, which influenced the results significantly (Fe_2B: 12 GPa, 9.8 N and 20 GPa, 0.1 N).[85, 161]

The relationship between fracture toughness and sintering temperature, from Table 8, for the high Fe-B_4C composites are observed in Figure 57. It is evident in Figure 57 that at 900°C there was little difference in fracture toughness when observing the error range. As temperature

increased to 1000°C, fracture toughness of the 69.3% Fe-B_4C did not shift while 78 % Fe-B_4C showed a small increase. Further temperature increases to 1100°C resulted in the highest fracture toughness obtained in the 69.3 % Fe-B_4C composite, 3.4 MPa.$m^{0.5}$.

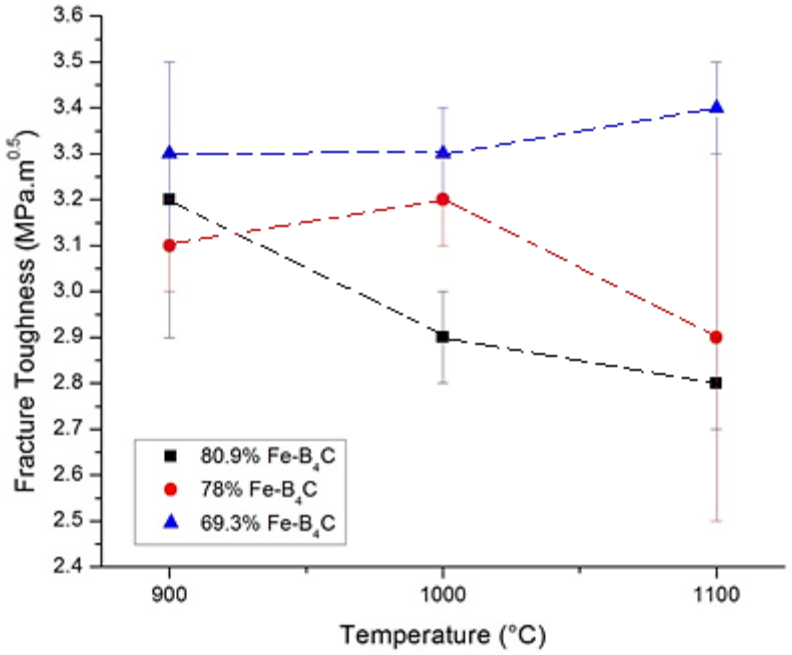


Figure 57: Sintering temperature effects on fracture toughness in composites with high Fe additions to B_4C.

78 % Fe-B_4C showed a decrease at 1100°C, corresponding to the decrease observed in the hardness of the same material (Figure 56). 80.9 % Fe-B_4C (Figure 57) showed a decrease in fracture toughness with increasing temperature, from 3.2 MPa.$m^{0.5}$ at 900°C to 2.8 MPa.$m^{0.5}$ at 1100°C. The microstructure at 1000°C was fine and well dispersed resulting in the improved fracture toughness; however growth of the phase at 1100 resulted in the decrease in fracture toughness.[100] Brittle $Fe_{23}(B,C)_6$ was most prevalent in the 80.9 % Fe-B_4C composition (Table 15) at 1000°C making up ≈ 19 vol. % and is caused the corresponding decrease in fracture toughness at 1000°C while grain growth with the significant presence of $Fe_3(B,C)$ was responsible for the further decrease at 1100°C.

The fracture toughness values obtained fall within the range given in literature for the various phases produced, shown in chapter 2.3.2 to be between 2.01 and 4.65 MPa.m$^{0.5}$. The fracture toughness of Fe_2B had values in literature throughout the 2.01 to 4.65 MPa.m$^{0.5}$ range, however $Fe_3(B,C)$ was below 3 MPa.m$^{0.5}$.[78, 84, 86, 88, 89] This suggests that along with porosity, grain growth the presence of the more brittle $Fe_3(B,C)$ e-B_4C sintered at 1000°C and the 78 and 80.9% Fe-B_4C sintered at 1100°C result in the decrease in fracture toughness.[100]

Figure 58 shows the microstructure around the Vickers indentation, using a 5 kg load, along with the cracks used to determine the indentation fracture toughness. It was clear from Figure 58 a) that the propagation of the cracks was hindered by the presence of a two-phase microstructure, through a secondary phase toughening mechanism. Where the interface is weak relative to the grain, intergranular cracking may occur.[162] This is seen in Figure 58 a) where the crack meets a second phase and changes direction as the crack propagates along the grain boundary of the second phase. Figure 58 b) showed transgranular crack propagation in the 80.9 % Fe-B_4C composites as the amount of the Fe_2B relative to the $Fe_3(B,C)$ phase was less than in samples containing smaller amounts of Fe (Table 15).

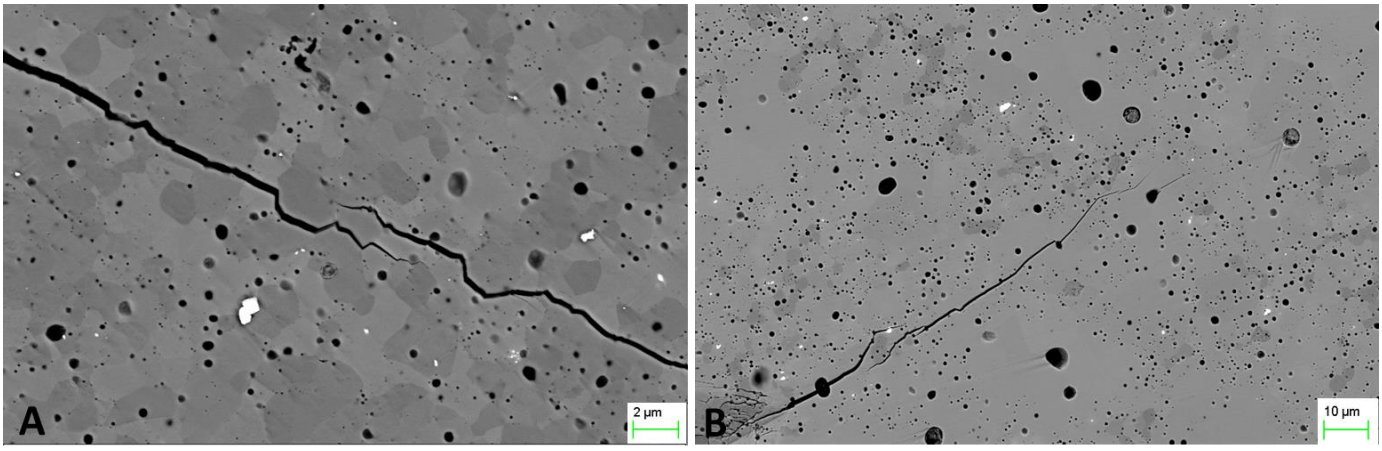


Figure 58: BS-SEM analysis of Vickers (5 kg) indentation cracks showing evidence of a) intergranular cracks in 78 vol. % Fe-B_4C sintered at 1000°C and b) transgranular crack propagation in 80.9 vol. % Fe-B_4C sintered at 1100°C.

Table 8 (chapter 4.2.1) shows adding Ti to the system resulted in a decrease in hardness for the majority of the samples relative to the composites with iron only additions. The hardness of the 69.3 % (0.8Fe+0.2Ti)-B_4C material was the highest obtained at 14.4 GPa, while 78 % (0.8Fe+0.2Ti)-B_4C reached 11.6 GPa when sintering at 1100°C and 60 MPa. Both values fell within the error of the pure Fe produced under the same conditions. Unlike the Fe-B_4C composites, the hardness of the 69.3 and 78 % composites was seen to increase with increasing sintering temperature. Meanwhile the 80.9 % (0.8Fe+0.2Ti)-B_4C was the opposite, with hardness decreasing as temperature increased. It was evident From Table 8 that samples with additions of Ti showed some improvements in the fracture toughness compared to the pure Fe. The 80.9 % (0.8Fe+0.2Ti)-B_4C attained the highest fracture toughness of 5.9 $MPa.m^{0.5}$ when sintering at 900°C and 60 MPa. The variations between temperature and additions to B_4C, again could not be looked at individually, and had to be inclusive of the temperature effects on the microstructure of the materials produced. The evolution of the microstructure was major factor affecting the hardness and fracture toughness of the composites with the addition of Ti. The formation of the hard TiC phase was responsible for increase increased hardness and fracture toughness of the materials.[163]

Figure 59 compares the hardness of the low Fe containing composites shown in Table 9. At 2000°C hardness was found to be > 30 GPa for each of the materials, with a maximum of 33.1 GPa for 1% Fe-B_4C, whilst lowering the sintering temperature to 1910°C resulted in significantly lower hardness (< 21 GPa). The relative density achieved for the composites was mentioned in Figure 59, thus the effect of densification on the hardness of the materials was observed and seen to be crucial to the hardness of the composites.[57, 159] At 2000°C, where densification above 97 % occurred, increasing Fe content was seen to correspond to a decrease in hardness. This was expected with the increasing presence of the softer FeB phase (≈ 16.5 GPa).[87]

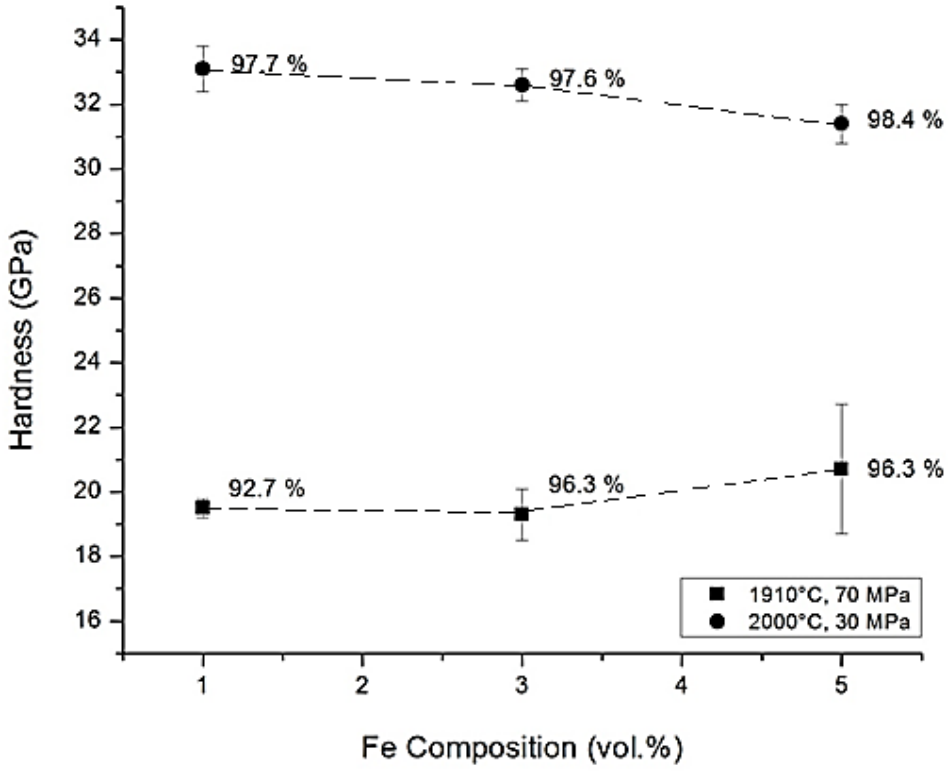


Figure 59: Comparison of hardness at 1910°C and 2000°C for low Fe containing composites, with relative density observed.

Comparing the hardness obtained in Figure 59 to those from literature in Table 1 (chapter 2.3.1), it was evident that the hardness values were comparable. Hayun et al.[55] reported hardness values of 32± 2 GPa which would fall within the range of the hardness observed in Figure 59 for the 1, 3 and 5 % Fe-B_4C sintered at 2000°C. Moshtaghiou et al.[57] achieved 100 % densification with a hardness of 36.4 GPa when SPS sintering pure B_4C at 1800°C and 70 MPa, with the superior hardness associated with the good densification and the sub-micron microstructure (688 nm) produced. The hardness of the materials sintered at 1910°C was comparable to those in Table 1 where densification was of the same order of magnitude. Thus it can be said good densification is essential to achieve the higher hardness range in these composites.[159]

Comparing Figure 59 to B_4C with 3.5 and 5.5 vol. % Fe additions that were pressureless sintered by Mizrahi et al.[92] and shown in chapter 2.3.2, showed that for samples of similar composition,

SPS improved densification and the subsequent hardness of the materials. This was expected with the application of pressure and FAST heating of the sample.[43]

Replacing 20 % of the Fe with Ti showed little difference in hardness at 1910°C (Table 9), and was seen to decrease at 2000°C for the 3 and 5 % (0.8Fe+0.2Ti)-B_4C composites. The 1 % addition to B_4C showed a slight improvement in hardness (34.6 GPa) relative to the iron only composition. The Ti-B_4C composites that were investigated showed an increased hardness with increasing amounts of Ti, reaching a maximum of 27.1 GPa at 2000°C, which was lower than the Fe only composites. The formation of TiB_2 phase was responsible for the slight improvement in hardness,[58] and in the presence of the FeB liquid phase its distribution was improved relative to the pure Ti; where distribution was controlled by mixing and the larger particle size of the Ti material relative to B_4C in the starting powder (Figure 32 and Figure 34).

The fracture toughness of the low Fe-B_4C composites in Figure 60 was seen to increase at 1910°C and decrease at 2000°C with increasing Fe content. The decrease at 2000°C occurred as the amount of FeB present increased. As shown in Figure 29, the FeB phase is prone to cracking a pulling away from the B_4C due to the thermal expansion differences. As a result, as the amount of this phase increased, it offered little to no resistance to crack propagation, and had an embrittling effect rather than acting as a secondary toughening mechanism. The opposite appears to be the case at 1910°C; however, considering the error in the composites, the increase is negligible. The error in the composites was observed to be greater than that at 2000°C and was a result of the increased porosity effects in observing the cracks produced with the Vickers indentation. Moshtaghiou et al.[57] observed the highest fracture toughness for the least dense sample (90.3 %) and suggested pores act as crack arrestors in B_4C. This may influence the relatively high fracture toughness attained as any pulled-out phase would leave porosity,[157] which, acting as a crack arrestor would result in higher fracture toughness. Improved densification with increasing sintering temperature was observed for each of the samples in Figure 60, with the 1 % Fe-B_4C attaining a fracture toughness of 5.3 $MPa.m^{0.5}$.

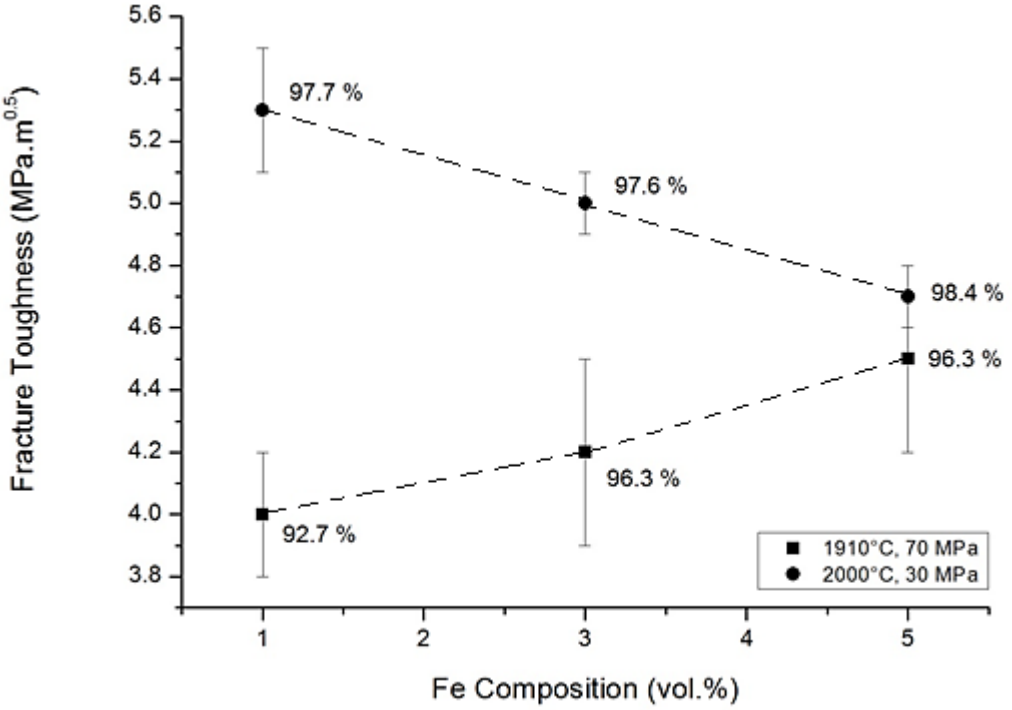


Figure 60: Fracture toughness with 1 – 5 vol. % Fe additions to B_4C sintered at 1910°C and 2000°C.

The fracture toughness in Figure 60 was compared to literature using Table 1 (chapter 2.3.1). Fracture toughness values were reported in the range of 1.88 to 4.9 MPa.m$^{0.5}$, showing the fracture toughness of the materials investigated in Figure 60 were comparable to the upper range.

Observing the effects of Ti additions to the system in Table 9, the fracture toughness of the (0.8Fe+0.2Ti)-B_4C materials showed significant improvements compared to the relative Fe-B_4C composites when sintering at 1910°C where the highest fracture toughness was 5.6 MPa.m$^{0.5}$ for 3 % (0.8Fe+0.2Ti)-B_4C. At 2000°C, the values of the iron only composites and the Fe-Ti combination were practically identical. The Ti-B_4C composites showed fracture toughness comparable to those of the Fe-B_4C materials at 1910°C. Only the 5 % was comparable to the Fe and Fe-Ti combination when sintering at 2000°C, while the 1 and 3 % did not show any changes from 1910°C. The improved fracture toughness in the Fe-Ti system at 1910°C was a result of the formation of the TiB_2 phase, which has been shown by Sigl et al. to be effective as a secondary toughening phase with B_4C.[58]

5.3. Transverse Rupture Strength

5.3.1. Weibull modulus and Characteristic Strength

The initial estimation of the Weibull modulus was determined by plotting ln(ln(1/s)) vs ln(σ) and fitting a straight line through linear regression to the data set. The linear regression estimated parameter was used as the initial m value in determining the modulus through the maximum likelihood estimate (MLE) method, using a 90% confidence interval as laid out in BS EN 843-5.[123] The m value determined is subject to bias which was corrected for in accordance with the standard for a 10 sample dataset.[123, 122] The fitted line determined through the MLE method was plotted through the failure probability versus strength data using a modified axis to compare the m values as seen in Figure 61 a) and Figure 62 a) for high and low vol. % additions to B_4C respectively.

A larger Weibull modulus is obtained for data where the sample had less variation in strengths obtained and as a result has increased reliability.[122] Figure 61 a) and b) shows the Weibull modulus of 12.1 for 78 % Fe-B_4C as the highest and the 6.9 for 80.9 % Fe-B_4C as the lowest.

Table 10 (chapter 4.4) shows the characteristic strength of the as measured data estimated from the unbiased m and also the strength when accounting for the effective volume of the sample, as the size of the test specimen influences the strength measurements, due to differences in the total volume of flaws.[122] The effective volume of the samples was calculated using the applet discussed in the experimental procedure (chapter 3.2.5), and taken into account in accordance with BS EN 843-5.[123] The strength data, accounting for the effective volumes, seen in Table 10, are shown in Figure 61 b) and Figure 62 b).

When comparing the data in Figure 61 a) and b), accounting for effective volume caused a shift of the strength data, resulting in a smaller effective characteristic strength being observed. The shift in strength was relatively uniform for each of the materials.

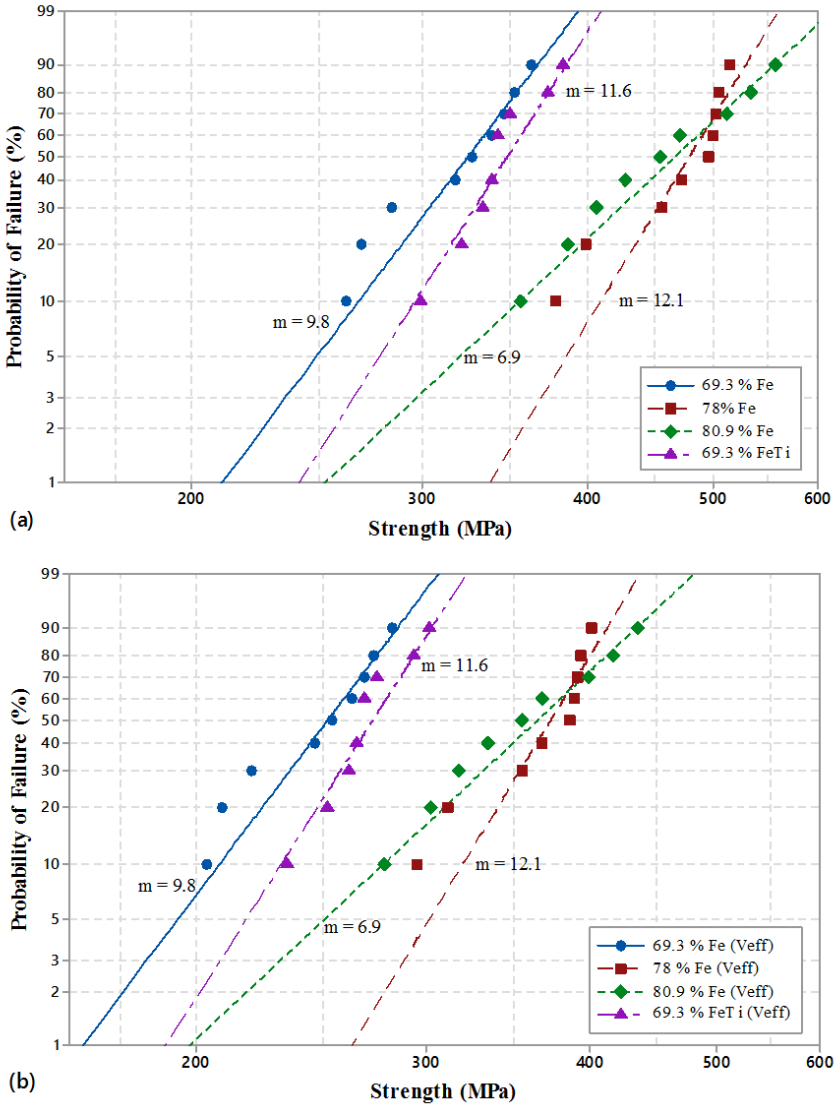


Figure 61: Probability of failure with Weibull modulus for additions ≥ 69.3 % to B_4C with a) as measured strength data and b) data considering effective volume of the test piece as per Table 10.

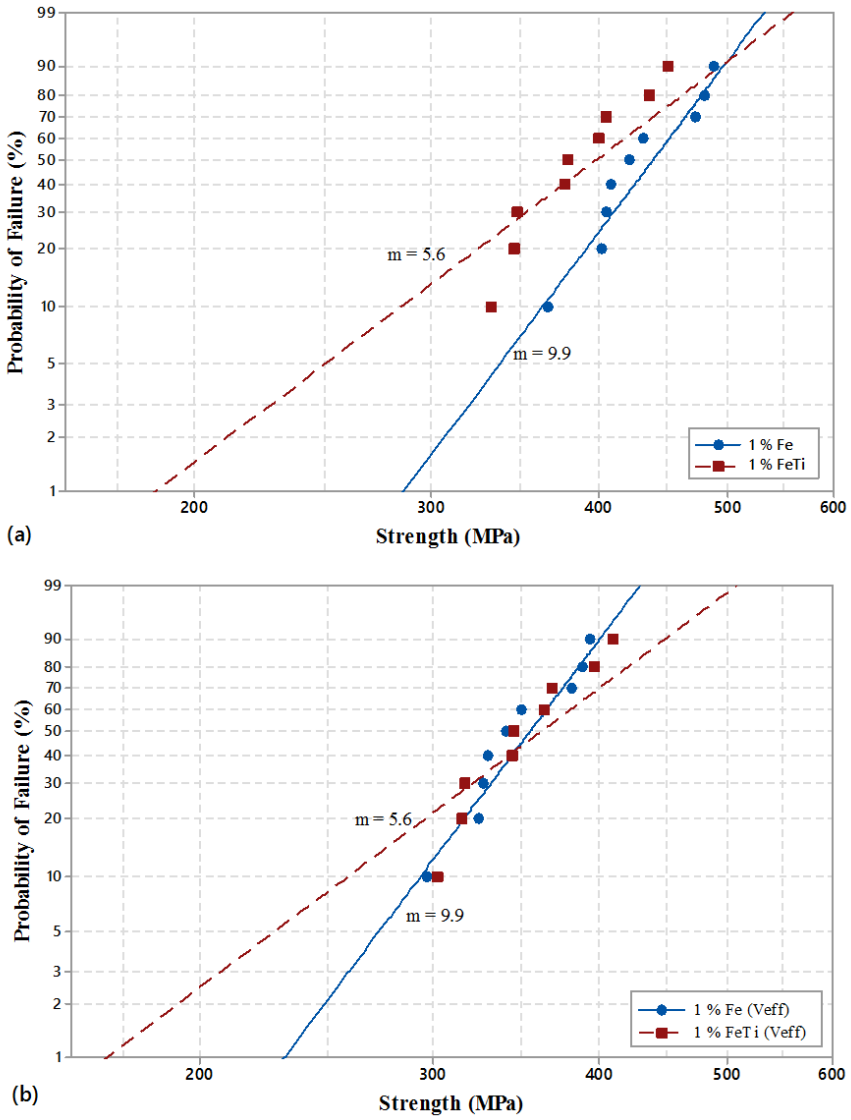


Figure 62: Determination of Weibull modulus and characteristic strength from a) B3B test data for 1 % Fe and FeTi additions to B_4C and b) accounting for the effective volume of the composites as shown in Table 10.

The modulus of 5.6 for the 1% (0.8Fe+0.2Ti)-B_4C was significantly lower than the 9.9 observed for the 1 % Fe-B_4C with no Ti incorporated as seen in Figure 62 a) and b). Considering the effective volumes of the materials, the data from the Fe only and Fe-Ti composite were almost overlapping in Figure 62 b). The shift is a result of difference in effective volume shown in Table 10 as 0.120 for 1 % Fe-B_4C and 0.586 for 1% (0.8Fe+0.2Ti)-B_4C. The difference was a result of variations in the thickness of the sample sets where; 1 % Fe-B_4C was 1.8±0.02 mm and 1%

(0.8Fe+0.2Ti)-B_4C was 1.9±0.02, combined with the low modulus achieved for 1% (0.8Fe+0.2Ti)-B_4C. The difference was the effective characteristic strength was higher than the Fe only composition. Accounting for the effective volume in Figure 62 b), it is evident that the measured data was fairly similar with the difference in characteristic strength a result of the modulus differences.

5.3.2. Relating strength to fracture toughness

Table 10 shows the transverse rupture strengths ranged from 263.4 - 392.1 MPa for the compositions investigated using the ball on three ball technique.[126,127] The characteristic strength, taking into account the effective volume of the composites ($\sigma_{0,V_{eff}}$), was related to the fracture toughness of the respective composite in Figure 63.

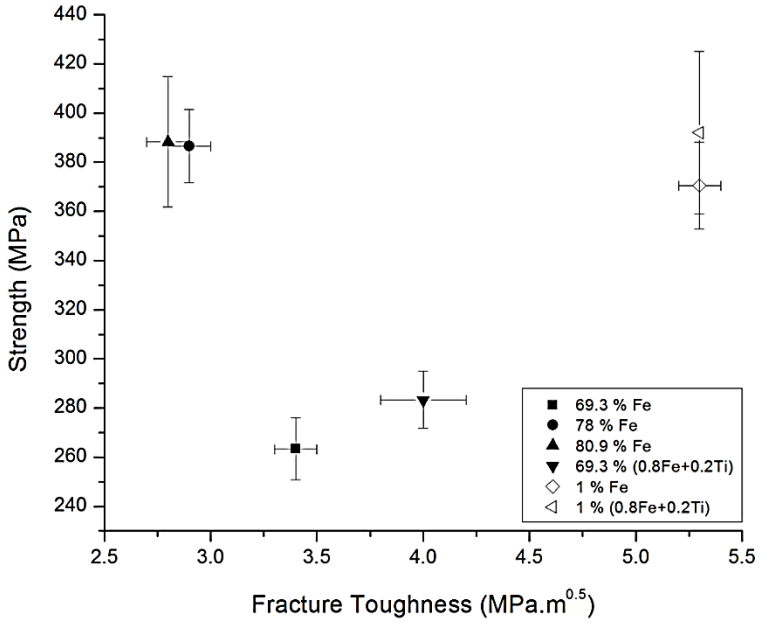


Figure 63: Comparison of fracture toughness with characteristic strength of select Fe-B-C composites.

Observing the 1% Fe and Fe-Ti additions to B_4C in Figure 63 shows the $\sigma_{0,V_{eff}}$ of the materials differed slightly but fell within the confidence intervals of each other (370.5 [353.3, 388.5] and

392.1 [360.4, 426.5] respectively). While the strength of the materials is comparable to some B_4C composites in literature, TRS values for pure B_4C in this grain size range, for fully dense materials, are reported between 450 and 500MPa; with small amounts of porosity shown to be detrimental to the strength.[2, 5, 59] The fracture toughness of the composites in Figure 63 was practically identical, with the difference in strength related to the composition differences of the material. SEM analysis of the fractured surface in Figure 37 a) shows transgranular fracture through B_4C with evidence of FeB pull-out in the 1% Fe-B_4C microstructure. Figure 37 b) shows the difference with the addition of Ti in the 1% (0.8Fe+0.2Ti)-B_4C, while transgranular fracture through the B_4C phase was again visible, areas of intergranular fracture around the TiB_2 containing phase may have offered the slight improvement in strength. Residual stresses at the interface and free carbon, further weakening the interface also reduced the strength of the materials.[157, 164]

The strengths observed for the 69.3 % Fe and the 69.3 % Fe-Ti composites (263.4 and 283.3 MPa respectively) were within each other's confidence intervals, and those observed for the 78 and 80.9 % Fe (386.5 and 388.3 MPa) composites were comparable. The fracture toughness of 78 and 80.9 % Fe-B_4C in Figure 63 is in the same range. The microstructures of the two samples displayed in Figure 36 (B2 and C2) show fracture surfaces with similar appearances, both with signs of intergranular and transgranular fracture with porosity at the grain boundaries which would have lowered the TRS.[165] Observing the microstructure of the fracture surfaces in Figure 36 (A2 and D2) showed evidence of transgranular fracture in both composites, with intergranular fracture in 69.3 % Fe-B_4C but no evidence of such in the 69.3 % (0.8Fe+0.2Ti)-B_4C. The carbon rich areas observed in the microstructures of the composites in Figure 23 and Figure 27 were visible, with a sponge-like appearance.

The fracture toughness of the 69.3 % additions to B_4C in Figure 63 show the composite with Ti added to have a higher fracture toughness than that without, both 69.3 % compositions had fracture toughness' higher the 78 and 80.9 % Fe-B_4C though the strengths of these materials were lower. The lower strengths were a result of the large amounts of free carbon present within the materials. The carbon in the samples along with the porosity associated with the 69.3 %

additions was detrimental to the strength of the materials with values more than 100 MPa lower than the other composites investigated (Figure 63).[5, 165]

5.4. Wear

The wear rates of the composites investigated varied significantly as observed in Table 11, ranging from 1.77×10^{-6} mm^3/Nm for 69.3 % Fe-B_4C to 36.92×10^{-6} mm^3/Nm for 1 % Fe-B_4C when using silicon nitride balls. The wear observed was within the range of 10^{-6} to 10^{-2} mm^3/Nm and was considered severe.[130]

5.4.1. Friction co-efficient and wear track analysis

Figure 64 shows the wear rates, observed in Table 11, for the sample and the corresponding ball relative to the coefficient of friction that was measured. The width of the wear tracks Figure 38 (a, b and c) and Figure 44 (b and c) of the high vol % Fe-B_4C composites increased with increasing iron content indicating higher wear rates.[143] Figure 64 (a and b) show this to be the case and also indicates the increased coefficient of friction with increased Fe content and wear. Thus, increasing the amount of $Fe_3(B,C)$ relative to Fe_2B (Table 16) results in an increased wear rate, with wear rates of the materials form literature suggesting lower wear rates for Fe_2B compared to the Fe_3C type phase[166, 167] Also, the high amounts of free carbon present in 69.3 % Fe-B_4C may act as a lubricant during wear.[168]

Using Si_3N_4 balls showed evidence of SiO_2 in the wear track of the high Fe-B_4C samples (Figure 45). This had a lubricating effect on the interface between the ball and the sample during testing resulting in the lower friction coefficients and the subsequent lower sample wear rates (Figure 64 a) than those subjected to steel balls (Figure 64 b) even though the Si_3N_4 balls are much harder.[169] Oxidation was observed using the steel balls as well, with iron oxide debris identified in the wear scars of each composite where the steel balls had been used (chapter 4.5.1.1). Adhesion during wear was more likely with the steel balls than Si_3N_4 due to the Fe content in the

samples combined with the high temperatures that arise at the contact interface during sliding.[128]

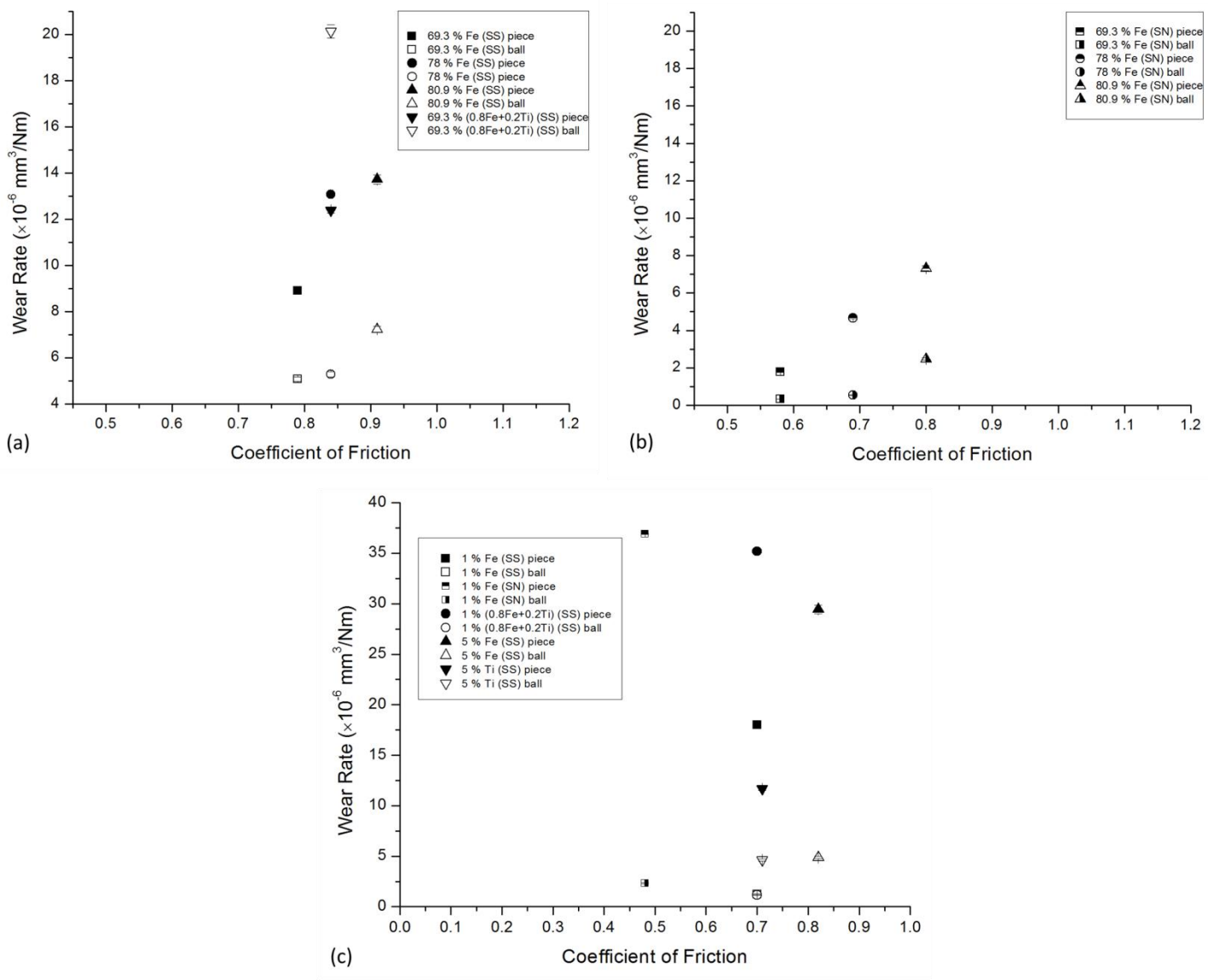


Figure 64: Relationship between sample and ball wear rate and friction coefficient for a) ≥ 69.3 % additions to B_4C with stainless steel balls, b) ≥ 69.3 % additions to B_4C with Si_3N_4 balls and c) additions ≤ 5 vol. %.

The addition of Ti in the 69.3 % (0.8Fe+0.2Ti)-B_4C resulted in higher wear rates with a corresponding increase in friction coefficient relative to 69.3 % Fe-B_4C. It is clear from Figure 64 that, for the majority of the samples, wear of the ball was lower than that of the sample. The

exception to this was the 69.3 % (0.8Fe+0.2Ti)-B_4C with a wear rate of 12.39×10^{-6} mm^3/Nm in the presence of a steel ball, with a corresponding wear rate of 20.14×10^{-6} mm^3/Nm shown in Figure 64 a), suggesting increased interaction with ball and the harder TiC phase.[163]

Wear of polycrystalline ceramics, is typically characterized by an initial mild, deformation controlled wear regime, followed by a transition to a severe fracture controlled wear.[170] The cracks observed in each of the microstructures and demonstrated in Figure 41 and Figure 46, are indicators of severe wear showing abrasive fracture of the surface and its subsequent removal. Along with the cracks and oxide phases, examination of the wear tracks showed fragmentation with fine dispersions of sample particles contributing to the debris, grooving, pull-out of grains and delamination (chapter 4.5.1).[132] Delamination, similar to that observed by Aatthisugan et al. where Mg alloys were reinforced with B_4C, was seen in each of the high additions to B_4C and was most prominent when using the Si_3N_4 balls, as seen Figure 46, it was not identified in composites with low additions.[168]

Observing the wear in Figure 64 c) with additions to $B_4C \leq 5$ %, the lower coefficient of friction resulted in with the maximum observed wear rate for 1 % Fe-B_4C corresponding to the lowest friction coefficient of 0.48, differing from the trends observed with the high vol. % additions to B_4C. The wear on the Si_3N_4 ball of 1.24 mm^3/Nm used with 1 % Fe-B_4C in Figure 64 c) was not the highest, but was more than 3 times that observed for Si_3N_4 ball used on the 69.3 % Fe-B_4C in Figure 64 a).

The friction coefficient is a measure of the resistance to motion when two sliding surfaces are in contact and typically consists of three components; abrasion, adhesion and deformation on interlocking asperities.[129, 131] Thus, the lower coefficient of friction with a higher wear rate experienced for the 1 % Fe-B_4C using for the Si_3N_4 ball compared to the Fe ball, was an indication that the resistance of the sample to abrasion was lower for the harder Si_3N_4 ball than the steel ball. This was evident observing from the wear tracks of 1 % Fe-B_4C in Figure 42 (a) and Figure 44 (a) where iron oxide debris was present when using steel balls; however no oxide debris was evident when using Si_3N_4. The 1% (0.8Fe+0.2Ti)-B_4C sample showed nearly double the amount of wear than the 1% Fe only composition with steel ball counterbodies. The hard

TiB_2 phases were expected to have acted as third body between the ball and the sample, gouging the material severely as was further evidenced in the appearance of the cross-sections of the tracks, depicted in Figure 65 showing the average of the four measurements across the track.[58, 132] The harder Si_3N_4 ball produced a deeper and smoother wear track in line with the high wear and little interaction between the sample and the ball. The high wear rates are evident and the low resistance to wear arises due to the poor FeB-B_4C interface.[69]

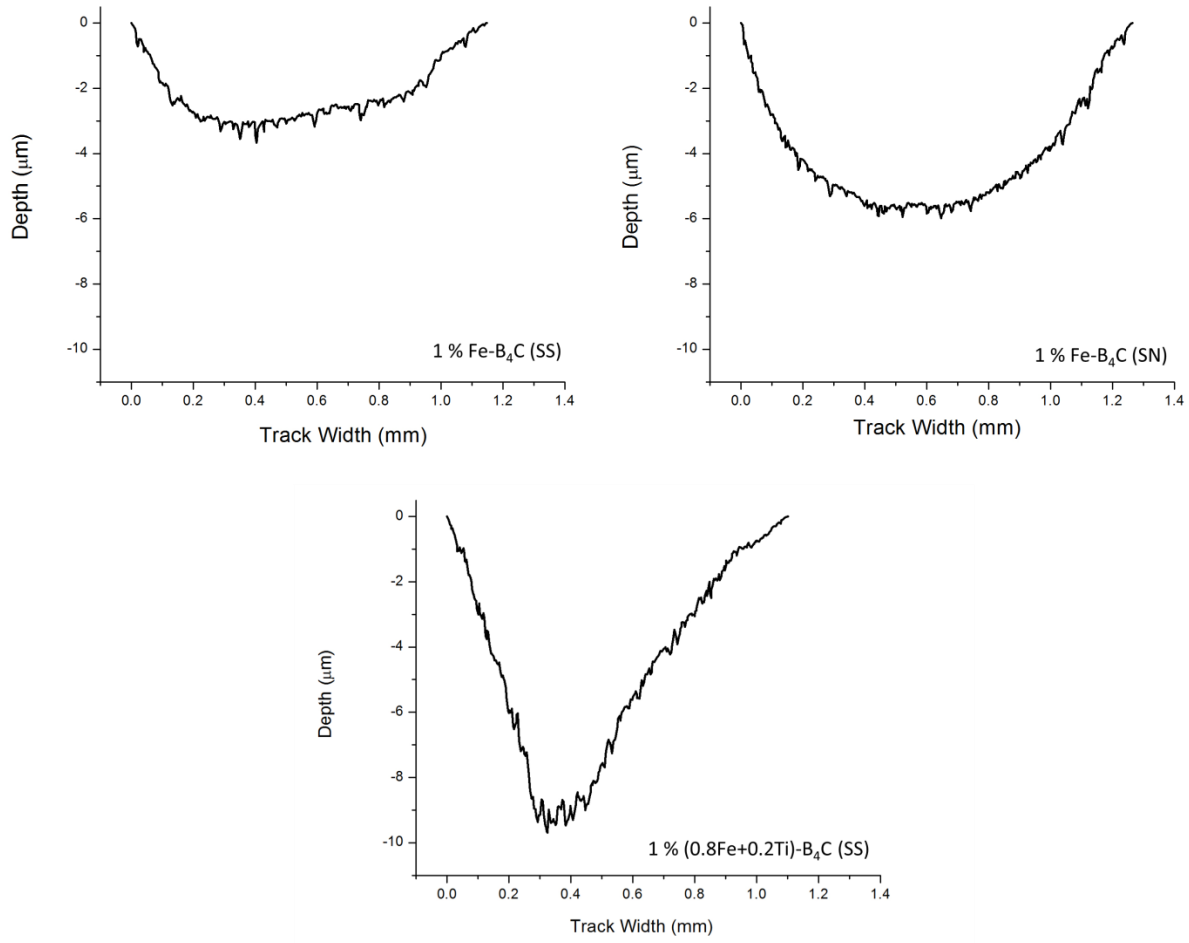


Figure 65: Comparison of average cross-sectional area of wear tracks for 1% additions to B_4C.

5.4.2. Effect of mechanical properties on wear

Figure 66 a) and b) showed the wear rate of the samples relative to their hardness fracture toughness respectively. Observing the wear of the high additions of Fe to B_4C, where hardness was < 15 GPa and fracture toughness ≤ 4 MPa.$m^{0.5}$, it was evident that the wear rates of the samples decreased with increasing hardness and likewise with increasing fracture toughness. Comparing the use of steel a Si_3N_4 balls on the wear rates, in this range, it was seen that wear rate decreased as hardness and fracture toughness increased.

Higher hardness and fracture toughness have been shown to improve the abrasive wear resistance of materials.[128] During the sliding wear process, the samples are indented and ploughed by the ball, the improved hardness of the materials allows for greater resistance to deformation improving the wear rate.[130] During sliding in ceramics the wear particle forms as a result of the formation and the propagation of cracks in the material.[171, 130] Thus, improved fracture toughness improves the resistance to formation and propagation of these cracks, consequently improving the wear properties. The hardness and fracture toughness of the high additions to B_4C were related to the phases present (chapter 5.2.3), with higher Fe_2B compositions being harder and, providing improved wear rates as discussed in the previous chapter (5.4.1).[166, 167]

Although the hardness and fracture toughness could provide an indication of a materials wear resistance, wear is sensitive to a number of factors including mass, shape environment and the materials properties.[130] This is evident in Figure 66 a) and b) when observing composites with additions of 1 – 5 % to B_4C, where hardness was > 25 GPa and fracture toughness was > 4.5 MPa.$m^{0.5}$, yet the wear rate was significantly higher than those observed with additions ≥ 69.3 % additions to B_4C. Also, when comparing 69.3% Fe-B_4C to 69.3 (0.8Fe+0.2Ti)-B_4C and 1 % Fe-B_4C to 1 % (0.8Fe+0.2Ti)-B_4C it was clear that although the hardness and fracture toughness of the composites was improved with the addition of Ti, the wear rate increased. Although the wear of the 1-5% addition to B_4C was higher, the values obtained were comparable to literature, showing some improvements on hot pressed and pressureless sintered (93 % dense) B_4C materials[172]; however, wear rates were 3 orders of magnitude higher when compared to fully dense B_4C with a hardness of 36.3 GPa using an alumina and SiC ball.[173] Comparing the high

Fe compositions to literature show the depths of the wear tracks to be similar to those shown by Bagliuk et al. when investigating small B_4C additions to Fe.[9]

The higher wear in the 1-5 % Fe-B_4C composites was due to the FeB-B_4C interactions; with the additional stresses experienced during wear resulting in the breakaway of FeB from the matrix and its subsequent removal. The resultant porous B_4C microstructures were susceptible to severe wear as resistance to abrasive ploughing diminished with porosity acting as a stress raiser.[128]

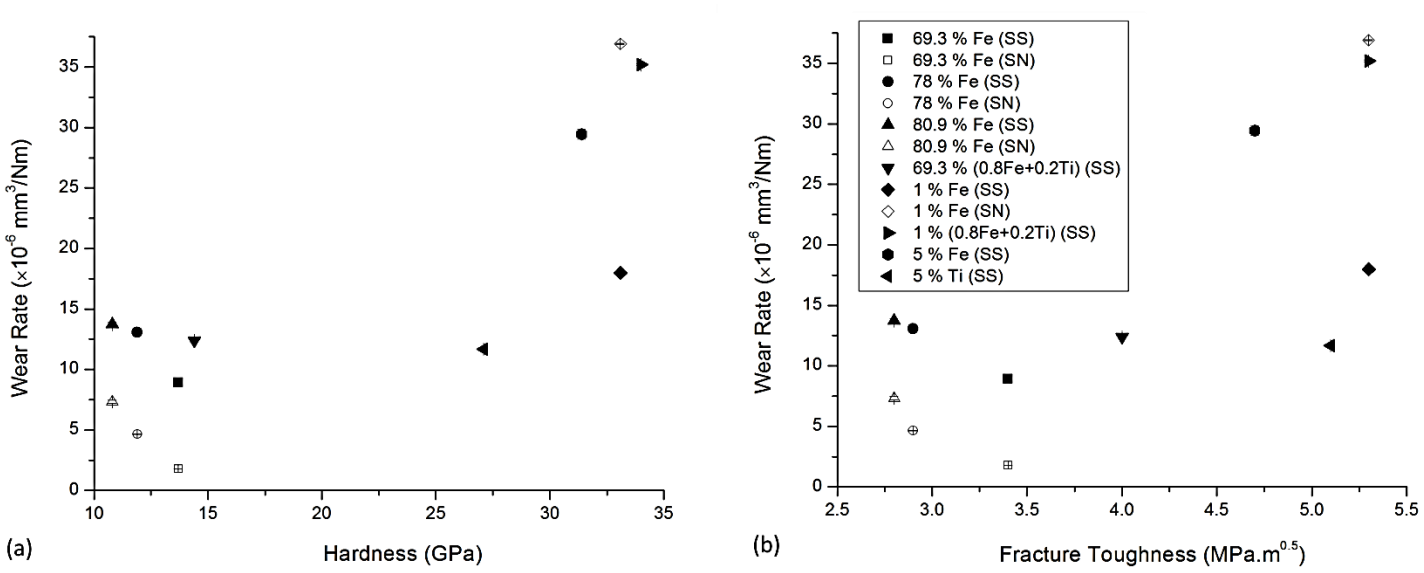


Figure 66: Relationship between sample wear rate and a) hardness and b) fracture toughness of sliding wear tested composites.

6. Conclusions and future work

- Fe-B-C composites were produced, from boron carbide and iron powders, using spark plasma sintering. This provided information on the effects of rapid sintering on densification, composition and the microstructure of the materials produced. The composition range included a selection high Fe contents (69.3, 78 and 80.9 vol. % Fe-B_4C) and high B_4C concentrations (1, 3, 5 vol. % Fe-B_4C).

- It was possible to mix and disperse Fe powder with B_4C, although contamination from the milling media plays a significant role in the composition where small additions to B_4C are investigated.

- Composites with Fe additions ≥ 69.3 % to B_4C were spark plasma sintered at 900, 1000 and 1100°C; where each composition achieved above 97 % relative density at a sintering temperature of 1100°C and 60 MPa. Reaction sintering occurs producing Fe_2B and metastable $Fe_3(B,C)$ as the major phases. Carbon, $Fe_{23}(B,C)_6$, FeB and iron were observed as additional products, however iron was only observed through XRD analysis and was not clearly distinguishable in the microstructure.

- Amounts of the main phases produced, Fe_2B and $Fe_3(B,C)$, were compared to those expected at equilibrium and were seen to deviate significantly. The phase deviations with temperature and composition, showed the non-equilibrium nature of producing the composites using SPS. Reactions between Fe and B_4C were very rapid and even with fast heating and cooling rates, the B_4C phase completely reacted with the Fe, resulting in only brittle phases being produced.

- Hardness and fracture toughness values up to 13.7 GPa and 3.5 $MPa.m^{0.5}$ respectively were attained for the high Fe additions to B_4C. Although densification improved throughout the sintering range, growth of pores and grains at 1100°C negatively affect the hardness and fracture toughness; with densification and growth competing in determining the hardness and fracture toughness of the materials.

- The microstructure of the composites evolved with changing sintering temperature, producing a refined multiphase precipitate structure at 1000°C. The refined structure was associated with the highest hardness values of 13.2 and 10.9 GPa observed in the 78 and 80.9 vol. % Fe-B_4C composites respectively.

- The precipitation of two main phases, Fe_2B and $Fe_3(B,C)$, allowed for some secondary phase toughening. Composites showed evidence of intergranular crack propagation where sufficient quantities of both phases were present. In the 80.9 % Fe-B_4C composites where less Fe_2B was present relative to the $Fe_3(B,C)$, cracks were mostly observed to propagate in a transgranular fashion resulting in a lower fracture toughness.

- Substituting 20 vol. % of the Fe in the composites with Ti resulted in comparable hardness values for the 69.3 and 78 % (0.8Fe+0.2Ti)-B_4C when sintering at 1100 °C and 60 MPa, the 69.3 % tending to be slightly higher, with a hardness of 14.4 GPa. Fracture toughness' up to 5.9 $MPa.m^{0.5}$ were obtained and were higher than the pure Fe additions.

- Starting compositions of 1-5 vol. % Fe-B_4C were sintered to relative densities > 97 % at 2000°C with a pressure of 30 MPa. Onset of densification was promoted by the formation of a transient FeB liquid phase, which played a significant role up to ≈ 1820°C. Above 1880°C B_4C-B_4C interactions were played a role in densification, allowing for fully dense materials to be produced. Sintering temperature was limited to 2000°C as higher temperatures and pressures promoted the loss of the liquid phase. Additions of Ti allowed for the formation of a TiB_2 phase within the system, but did not show improvements in densification.

- FeB is prone to cracking and pulling away from the B_4C matrix, introducing porosity and resulting in significant pull out of the phase during grinding and polishing. This was caused by carbon at the grain boundary weakening the FeB-B_4C interface, along with residual stresses arising through differences in the thermal expansion coefficients.

- The hardness and fracture toughness of the low Fe-B_4C composites was greatest for the 1 % Fe-B_4C, reaching 33.1 GPa and 5.3 $MPa.m^{0.5}$ when sintering at 2000°C and 30 MPa.

Densification was crucial to the hardness observed with lower temperature and densification at 1910°C seeing differences in hardness > 10 GPa.

- Hardness decreased with increasing Fe content, as expected with the presence of an increasing amount of the softer FeB phase with B_4C. The nature of the FeB phase, with its susceptibility to cracking, resulted in its presence embrittling the materials, where increased FeB resulted in a deterioration of fracture toughness.

- The low Fe-Ti combinations improved fracture toughness of the materials at 1910°C, with a fracture toughness of 5.6 MPa observed for 3 % (0.8Fe+0.2Ti)-B_4C. At 2000°C. However, fracture toughness was comparable to the Fe only composites. Ti-B_4C showed no improvements in properties compared to the Fe-B_4C materials.

- The Weibull modulus was determined for TRS composites, with the highest of 12.1 associated with the 78 % Fe-B_4C and the lowest of 5.6 with 1 % (0.8Fe+0.2Ti)-B_4C. The effective volume of the composites was taken into account as per BS EN 834-5.[123] Investigations of the transverse rupture strength showed 78 % and 80.9 % Fe-B_4C composites to have strengths in the same range as the 1% Fe and 1 % Fe-Ti additions to B_4C. The 1 % Fe-Ti composite had the highest strength, 392.1 [360.4, 426.5] with the other compositions mentioned falling within the 90 % confidence interval. Free carbon and porosity in the 69.3 % additions to B_4C was detrimental to their strength.

- The wear rates of composites with high Fe additions to B_4C decreased as their respective hardness and fracture toughness increased. The wear rate was lower in the presence of a Si_3N_4 counterbody than those observed with steel. The SiO_2 dispersed through the wear track acted as a lubricant during testing with Si_3N_4 lowering the friction coefficient and subsequent wear, while interactions between the steel ball allowed for higher wear rates. Composites with more Fe_2B phase present performed better

- Stresses at the FeB-B_4C interface were detrimental to the wear of composites with low additions to B_4C. FeB was removed from the matrix leaving behind a porous surface that offered little resistance to wear as the wear body ploughed through the material. Wear

rates were lower for steel balls with the presence of Fe_2O_3 debris in the wear track. The harder Si_3N_4 ball with the 1 % Fe-B_4C produced the highest wear rate of all the composites of 36.92×10^{-6} mm^3/Nm. The combination of Fe and Ti resulted in increased wear as additional TiB_2 in the wear debris enhanced wear.

- Properties of the materials were compared to Fe-B-C materials, from literature, that commonly find use in wear applications. The high Fe-B_4C materials showed potential for use in wear applications with where properties were comparable to Fe-B-C of composites already used. The porosity may be an issue and would have to be remedied. The density of the composites is a drawback for use in armor where the lightweight properties of ceramics are exploited.

- The B_4C rich Fe-B-C compounds had densities that would make them suitable for armor applications, although the strengths were low compared to many fully dense B_4C materials. Although Fe could facilitate densification at lower temperatures and the hardness and fracture toughness of the materials was good, the poor relationship between FeB and B_4C was detrimental to wear compared with B_4C ceramics. Thus, its potential for use in these applications is poor.

Future work

Preventing/limiting the reaction of Fe with B_4C will allow for materials with the beneficial properties of B_4C (high hardness and wear resistance) while benefitting from the superior fracture toughness of iron. Limiting the temperature would be essential to slowing the rate of reaction. To densify the materials at lower temperatures, the pressure of the system would have to be increased significantly. For SPS this would require the use of specialized die sets that would allow for pressures in excess of 200 MPa to be investigated. The B_4C particle size could also be varied to observe the effects this has on maintaining B_4C and Fe.

The porosity in the high Fe materials needs to be removed, to allow for improved properties of the materials. Pre-reacted Fe-B_4C powders could be sintered to produce the materials. The effect of pre-reacted powders on grain size, porosity and phases produced with the corresponding properties could be investigated. The evolution and control of the Fe-B-C phases during sintering by varying starting compositions, temperature, heating rate, cooling rate and sintering hold times could be investigated to better predict phase compositions and subsequent properties in the system under various non-equilibrium conditions.

7. References

1. Imanaka Y. (ed.) The Ceramic Society of Japan, Advanced Ceramic Technologies & Products. Springer, Japan (2012).

2. Thevenot, F. Boron Carbide - A comprehensive review. Journal of the European Ceramic Society. Vol 6 (4) (1990) pp. 205-225.

3. Hayun S, Dariel M, Frage N and Zaretzky E. The high-strain-rate dynamic response of boron carbide-based composites: The effect of microstructure. Acta Materiala, Vol. 58 (2010) pp. 1721-1731.

4. Antadze M, Chedia R, Tsagareishvili O, Mikeladze A, Gacheciladze A, Margiev B, Gabunia D, Tsuladze T, Khantadze D. Metal-ceramics based on nanostructured boron carbide. Solid State Sciences, Vol. 14 (2012) pp. 1725-1728.

5. Telle R, Sigl L, Takagi K. Boride-based hard materials. Handbook of Ceramic Hard Materials, Vol. 2, Riedel R (Ed.), Wiley-VCH, Germany. (2000) pp. 802-945.

6. Lee H, Speyer R. Pressureless sintering of boron carbide. Journal of the American Ceramic Society, 86 (2003) pp. 1468-1473.

7. Liu Z, Li Y, Chen X and Hu K. Microstructure and mechanical properties of high boron white cast iron. Materials Science and Engineering A, 485 (2008) pp. 112-116.

8. Fu H, Xiao Q, Kuang J, Jiang Z and Xing J. Effect of rare earth and titanium on the microstructure and properties of low carbon Fe-B cast steel. Materials Science and Engineering A, Vol.466 (2007) pp.160-165.

9. Bagliuk G. Properties and Structure of Sintered Boron Containing Carbon Steels. Sintering - Methods and Products, Dr. V. Shatokha (Ed.), Intech (2012) ISBN: 978-953-51-0371-4.

10. Spiridonova I.Structure and Properties of iron-boron-carbon alloys. Metal Science and Heat Treatment, No. 2 (1984) pp. 58-61.

11. Challenges and Opportunities for Spark Plasma Sintering: A Key Technology for a New Generation of Materials, Sintering Applications, Ertug B (Ed.), InTech, Croatia. (2013) ISBN: 978-953-51-0974-7. Suárez M, Fernández A, Menéndez J, Torrecillas R, Kessel H, Hennicke J, Kirchner R, Kessel T.

12. Vasconcelos C. New Challenges in the Sintering of HA/ZrO2 Composites. Sintering of Ceramics - New emerging techniques, Lakshmanan A. (ed.). Intech, Croatia. (2012).

13. De Jonghe L, Rahaman M. Sintering of Ceramics. Handbook of Advanced Ceramics, Somiya S (Ed.), Elsevier (2003).

14. Carter C, Norton M. Ceramic Materials - Science and Engineering. Springer Science+Business Media, LLC. New York (2007).

15. Barsoum M. Fundamentals of Ceramics. Institute of Physics Publishing, Bristol and Philadelphia (2003).

16. Higgins R. Properties of Engineering Materials, Second edition. Edward Arnold, London, U.K. (1994).

17. Mazumdar S. Composites Manufacturing: Materials, Product, and Process Engineering. CRC Press LLC. (2002).

18. Callister W, Rethwisch D. Fundamentals of Materials Science and Engineering: An integrated approach, 3rd edition. John Wiley and Sons, Inc., USA (2008).

19. Rahaman M. Ceramic Processing and Sintering, second edition. Marcel Dekker, Inc. (2003).

20. Askeland D. The Science and Engineering of Materials, Third S.I edition. Nelson Thomes Ltd., Cheltenham, U.K. (1998).

21. Kang S. Sintering, Densification, Grain Growth and Microstructure. Elsevier Butterworth-Heinemann, Massachusetts, USA (2005).

22. Rybakov K, Olevsky E, Krikun E. Microwave sintering: fundamentals and modeling. Journal of the American Ceramic Society, Vol. 96 (2013) pp. 1003-1020.

23. Raj R, Cologna M, Francis J. Influence of externally imposed and internally generated electrical fields on grain growth, diffusional creep, sintering and related phenomena in ceramics. Journal of the American Ceramic Society, Vol. 94 (2011) pp. 1941-1965.

24. Katz J. Microwave Sintering of Ceramics. Annual Review of Materials Science, Vol 22 (1992) pp. 153-170.

25. Menezes R, Souto P, Kiminami R. Microwave Fast Sintering of Ceramic Materials. Sintering of Ceramics - New Emerging Techniques, Dr. A. Lakshmanan (Ed.), Intech (2012) ISBN: 978-953-51-0017-1.

26. Thostenson E, Chou T. Microwave processing: fundamentals and applications. Composites Part A, Vol. 30 (1999) pp. 1055–1071.

27. Presenda Á, Salvador M, Peñaranda-Foix F, Moreno R, Borrell A.Effect of microwave sintering on microstructure and mechanical properties in Y-TZP materials used for dental applications. Ceramics International, Vol. 41 (5)(B) (2015) pp. 7125–7132.

28. Huang Z, Gotoh M, Hirose Y. Improving sinterability of ceramics using hybrid microwave heating. Journal of Materials Processing Technology, Vol. 209 (2009) pp. 2446–2452.

29. Menezes R, Souto P, Kiminami R. Microwave hybrid fast sintering of porcelain bodies. Journal of Materials Processing Technology, Vol. 190 (2007) pp. 223–229.

30. Qian B, Shen Z. Laser sintering of ceramics. Journal of Asian Ceramic Societies, Vol. 1 (2013) pp. 315–321.

31. Shellabear M, Nyrhilä O. DMLS- Development history and state of the art. Presented at LANE conference, Erlangen (2004).

32. Gahler A, Heinrich J, Günster J. Direct Laser Sintering of Al2O3–SiO2 Dental Ceramic Components by Layer-Wise Slurry Deposition. Journal of the American Ceramic Society, Vol. 89 (10) (2006) pp. 3076-3080.

33. Suárez M, Fernández A, Torrecillas R, Menéndez J. Sintering to Transparency of Polycrystalline Ceramic Materials. Sintering of ceramics - New emerging techniques, Lakshmanan A. (ed.). Intech, Croatia. (2012).

34. Sokol M, Kalabukhov S, Dariel M, Frage N. High-pressure spark plasma sintering (SPS) of transparent polycrystalline magnesium aluminate spinel (PMAS). Journal of the European Ceramic Society, Vol. 34 (16) (2014) pp. 4305-4310.

35. Grasso S, Kim B, Hu C, Maizza G, Sakka Y. Highly transparent pure alumina fabricated by high-pressure spark plasma sintering. Journal of the American Ceramic Society, Vol. 93 (2010) pp. 2460–2462.

36. Grasso S, Yoshida H, Porwal H, Sakka Y, Reece M. Highly transparent α-alumina obtained by low cost high pressure SPS. Ceramics International, Vol. 39 (2013) pp. 3243–3248.

37. Zhang F, Burkel E. Novel titanium manganese alloys and their macroporous foams for biomedical applications prepared by field assisted sintering. In: Biomedical Engineering, Trends, Researches and Technologies, Laskovski A (Ed.), InTech, Croatia. ISBN 978-.

38. Yanagisawa O, Hatayama T, Matsugi K. Recent Research on Spark Sintering. Materia Japan, Vol. 33 (12) (1994) pp. 1489-1496.

39. Xie G. Spark Plasma Sintering: A Useful Technique to Develop Large-Sized Bulk Metallic Glasses. Journal of Powder Metallurgy and Mining, Vol. 2 (2) (2013) e109.

40. Groza J, Anderson K, Fendorf M, Echer C. Surface oxide debonding in field assisted powder sintering. Materials Science and Engineering A, Vol. 270 (2) (1999) pp. 278-282.

41. Tiwari D, Basu B, Biswas K. Simulation of thermal and electrical field evolution during spark plasma sintering. Ceramics International, Vol. 35 (2) (2009) pp. 699-708.

42. Zhang J, Zavaliangos A, Groza J. The effect of specimen conductivity on current and temperature distribution in field activated sintering. International Conference on Powder Metallurgy & Particulate Materials, Las Vegas (2003).

43. Räthel J, Herrmann M, Beckert W. Temperature distribution for electrically conductive and non-conductive materials during Field Assisted Sintering (FAST). Journal of the European Ceramic Society, Vol. 29 (2009) pp. 1419–1425 .

44. Bouchacourt M, Thevenot F. The properties and structure of the boron carbide phase. Journal of Less Common Metals, Vol. 82 (1981) pp. 227-235.

45. Norimatsu W, Hirata K, Yamamoto Y, Arai S, Kusunoki M. Epitaxial growth of boron-doped graphene by thermal decomposition of B4C. Journal of Physics: Condensed Matter, 24 (2012) 314207 (5pp.).

46. Schwetz K, Karduck P. Investigations of the boron-carbon system with the aid of electron probe microanalysis. Journal of the Less Common Metals, 175 (1991) pp. 1-100.

47. Alizadeh A, Taheri-Nassaj E, Ehsani N. Synthesis of boron carbide powder by a carbothermic reduction method. Journal of the European Ceramic Society, Vol.24 (2004) pp. 3227-3234.

48. Jung C, Lee M, Kim C. Preparation of carbon-free B_4C powder from B2O3 oxide by carbothermal reduction process. Materials Letters, Vol. 58 (2004) pp. 609-614.

49. Campos-Silva I, Ortiz-Dominguez M, Keddam M, Lopez-Perrusquia N, Carmona-Vargas A, Elias-Espinosa M. Kinetics of the formation of Fe_2B layers in gray cast iron: Effects of boron concentration and boride incubation time. Applied Surface Science, Vol. 225 (2009) pp. 9290-9295.

50. Sarikaya O, Anik S, Celik E, Cem Okumus S, Aslanlar S. Wear behaviour of plasma-sprayed AlSi/B_4C composite coatings. Materials and Design, Vol. 28 (7) (2007) pp. 2177-2183.

51. Gui M, Suk Bong Kang S. Aluminum hybrid composite coatings containing SiC and graphite particles by plasma spraying. Materials Letters, Vol. 51, (5) (2001) pp. 396-401.

52. Oliveira J, Conde O. Deposition of boron carbide by laser CVD: a comparison with thermodynamic predictions. Thin Solid Films, Vol. 307 (1997) pp. 29-37.

53. Klotz B, Cho K and Dowding R. Sintering aids in the consolidation of boron carbide (B_4C) by the plasma pressure compaction (P2C) method. Materials and Manufacturing Processes, 19 (2004) pp. 631-639.

54. Ghosh D,Subhash G, Sudarshan T, Radhakrishnan R and Gao X. Dynamic indentation response of fine grained boron carbide. Journal of the American Ceramic Society, 90(6) (2007) pp. 1850-1857.

55. Hayun S,Paris V, Dariel M, Frage N and Zaretzky E. Static and dynamic mechanical properties of boron carbide processed by spark plasma sintering. Journal of the European Ceramic Society 29 (2009) pp. 3395-3400.

56. Hayun S, Kalabukhov S, Ezersky V, Dariel M, Frage N. Microstructural characterization of spark plasma sintered boron carbide ceramics. Ceramics International, Vol 36 (2010) pp. 451-457.

57. Moshtaghioun B, Hernandez F, Garcia D, Martin S, Rodriguez A,Monshi A and Abassi M. Effect of spark plasma sintering parameters on on microstructure and room-temperature hardness and toughness of fine-grained boron carbide. Journal of the European Ceramic Society, 33 (2013) pp. 361-369.

58. Sigl L. Processing and mechanical properties of boron carbide sintered with TiC. Journal of the European Ceramic Society, Vol 18 (11) (1998) pp.1521-1529.

59. Suri A, Subramanian C, Sonber J, Murthy T. Synthesis and consolidation of boron carbide: a review. International Materials Reviews, Vol. 55 (1) (2010).

60. Shaw N. Densification and Coarsening During Solid State Sintering of Ceramics: A review of the models, I. Densificaton. Powder metallurgy International, Vol. 21, (3) (1989) pp. 16-31.

61. Dole S, Svante Prochazka S, Doremus R. Microstructural Coarsening During Sintering of Boron Carbide. Journal of the American Ceramic Society, Vol. 72 (6) (1989) pp. 958–966.

62. Telle R, Petzow G. Mechanisms in the liquid-phase sintering of boron carbide with silicon based melts. Materials Science Monographs, Vol. 38A (1987) pp. 961-973.

63. Champagne B, Angers R. Mechanical Properties of Hot-Pressed B-B4C Materials. Journal of the American Ceramic Society, Vol. 62 (3-4) (1979) pp. 149–153.

64. Larker H, Hermansson L, Adlerborn J. Hot isostatic pressing and its applicability to silicon carbide and boron carbide. Materials Science Monographs, Vol. 38A (1987) pp. 795-803.

65. Larsson P, Axen N, Hogmark S. Improvements of the microstructure and erosion resistance of boron carbide with additives. Journal of Materials Science, Vol. 35 (2000) pp. 3433–3440.

66. Schwetz K, Grellner W, Lipp A. Mechanical properties of HIP treated sintered boron carbide. Institute of Physics Conference Series, Vol. 75 (1986) pp. 413–426.

67. Schwetz K, Sigl L, Pfau L. Mechanical properties of injection molded B4C-C ceramics. Journal of Solid State Chemistry, Vol. 133 (1997) pp. 68–76.

68. Nadaraia L, Jalabadze N, Khundadze L. Spark plasma sintering of nanopowder and bulk samples of boron carbide. 2012 12th IEEE International Conference on Nanotechnology (IEEE-NANO), Birmingham. (2012) pp. 1-4.

69. Frage N, Hayun S, Kalabukhov S and Dariel M. The effect of Fe addition on the densification of B_4C powder sintered by spark plasma sintering. Powder Metallurgy and Metal Ceramics, Vol. 46, 11-12 (2007) pp. 533-538.

70. Aizenshtein M, Froumin N, Frage N, Dariel M. Interface interaction and wetting behaviour in B4C/(Me–Ti) systems (Me = Cu, Ag, Sn and Au). Materials Science and Engineering A 395 (2005) pp.180–185.

71. Mogilevsky P, Gutmanas E, Gotman I, Telle R. Reactive Formation of Coatings at Boron Carbide Interface with Ti and Cr Powders. Journal of the European Ceramic Society, Vol.15 (1995) pp. 527-53.

72. Telle R, Brook R, Petzow G. Ion beam modification, reaction sintering, precursor pyrolysis, clean room processing and mechanical testing - Challenges in the processing of ceramic hard materials. Journal of Hard Materials, Vol. 2 (1-2) (1991) pp. 79-114.

73. Fendler E, Babushkin O, Lindback T, Telle R, Petzow G. Modification of thermal mismatch in B4C-Diboride ceramics. Journal of Hard Materials, Vol.4 (3) (1993) pp.137-148.

74. Sigl L, Kleebe H. Microcracking in B_4C-TiB_2 Composites. Journal of the American Ceramic Society, Vol. 78 (9) (1995) pp. 2374-2380.

75. Makarenko G. Borides of the IVb Group. Boron and Refractory Borides, Matkovich V (Ed.), Springer Verlag, Berlin, Germany (1977) pp 310-330.

76. Chen X, Li Y. Effect of heat treatment on microstructure and mechanical properties of high boron white cast iron. Materials Science and Engineering A, 528 (2010) pp. 770-775.

77. Zeytin H, Yildirim H, Berme B, Duduoglu S, Kazdal G and Deniz A. Effect of boron and heat treatment on mechanical properties of white cast iron for mining application. Journal of Iron and Steel Research International, 18(11) (2011) pp.31-39.

78. Huang Z, Xing J, Lv L. Effect of tungsten addition on the toughness and hardness of Fe_2B in wear-resistant Fe–B–C cast alloy. Materials Characterization, 75 (2013) pp. 63–68.

79. Turov Y, Khusid B, Voroshnin L, Khina B, Kozlovskii I. Structure formation in sintering iron-boron carbide powder composite. Soviet Powder Metallurgy and Metal Ceramics, Vol. 30 (6) (1991) pp. 465-470.

80. Turov Y, Khusid B, Voroshnin L, Khina B, Kozlovskii I. Gas transport processes in sintering of an iron-boron carbide powder composite. Soviet Powder Metallurgy and Metal Ceramics, Vol. 28 (8) (1989) pp. 618-622.

81. Hasebe M, Nishizawa T. Thermodynamic Analysis of the Ternary Fe-C-B System. Journal of the Japan Institute of Metals and Materials, Vol. 38 (1) (1974) pp. 46-54.

82. Tkachenko V, Kogan Y. Structural characteristics and mechanical properties of sintered Fe-B4C materials. Soviet Powder Metallurgy and Metal Ceramics, Vol. 17 (5) (1978) pp. 384-388.

83. Campos I, Ramírez G, VillaVelázquez C, Figueroa U, Rodríguez G. Study of microcracks morphology produced by Vickers indentation on AISI 1045 borided steels. Materials Science and Engineering: A, Vol. 475 (1–2) (2008) pp. 285–292.

84. Ozdemir O, Usta M, Bindal C, Ucisik A. Hard iron boride (Fe_2B) on 99.97 wt% pure iron. Vacuum, Vol. 80 (2006) pp. 1391–1395.

85. Campos-Silva I, Hernández-Sánchez E, Rodríguez-Castro G, Cimenoglu H, Nava-Sánchez J, Meneses-Amador A, Carrera-Espinoza R. A study of indentation for mechanical characterization of the Fe2B layer. Surface & Coatings Technology, Vol. (232) (2013). pp. 173-181.

86. Rodríguez-Castro G, I. Campos-Silva I, Chávez-Gutiérrez E, Martínez-Trinidad J, Hernández-Sánchez E, Torres-Hernández A. Mechanical properties of FeB and Fe_2B layers estimated by Berkovich nanoindentation on tool borided steel. Surface & Coatings. Technology, Vol. (215) (2013) pp. 291–299.

87. Kunitskii Y, Marek E. Some Physical Properties of Iron Borides. Institute of Materials Science, Academy of Sciences of the USSR. Translated from Poroshkovaya Metallurgiya, No. 3 (99) (1971) pp. 56-59.

88. Topuz P, Gündoğdu E, Yılmaz E, Gümüş E. The Fracture Toughness of Fe_2B Formed on Boronized AISI 304. Materials Testing, Vol. 56 (9) (2014) pp. 690-693.

89. Coronado J, Rodriguez S. Cementite Characterization with Chromium and Vanadium Contents Using Indentation Technique. Journal of Iron and Steel Research, International, Vol. 22 (4) (2015) pp. 366-370.

90. ASM Alloy Phase Diagram Database. URL: http://www1.asminternational.org/asmenterprise/APD.aspx. As accessed November 2013.

91. Aizenshtein M, Mizrahi I, Froumin N, Hayun S, Dariel M, Frage N. Interface interaction in the B_4C/(Fe-B-C) system. Materials Science and Engineering A 495 (2008) pp. 70-74.

92. Mizrahi I, Raviv A, Dilman H, Aizenshtein M, Dariel M, Frage N. The effect of Fe addition on processing and mechanical properties of reaction infiltrated boron carbide-based composites. Journal of Materials Science, Vol. 42(16) (2007) pp. 6923–6928.

93. Bejar M, Moreno E. Abrasive wear resistance of boronized carbon and low-alloy steels. Journal of Materials Processing Technology, Vol. 173 (2006) pp. 352–358.

94. Chiou W, Carter E. Structure and stability of Fe_3C-cementite surfaces from first principles. Surface Science, Vol.530 (2003) pp. 87–100.

95. Subrahmanyam J. Wear studies on boronized mild steel. Wear, Vol. 95 (1984) pp. 287-292.

96. Ozkan O, Metin U, Cuma B, Ucisik A. Hard iron boride (Fe_2B) on 99.97 wt.% pure iron. Vacuum, Vol. 80 (2006) pp. 1391-1395.

97. Chicot D, Tricoteaux A. Mechanical Properties of Ceramics by Indentation: Principle and Applications. Ceramic Materials, Wunderlich W (Ed.), Sciyo, Croatia (2010).

98. Sherman D, Brandon D. Mechanical properties and their relation to microstructure. Handbook of ceramic hard materials, Vol. 2, Riedel R (Ed.), Wiley-VCH, Germany. (2000).

99. Krell A. A new look at grain size and load effects in the hardness of ceramics. Materials Science and Engineering, A245 (1998) pp. 277-284.

100. Xia S, Li G, Li C. Application of indentation technique in determining fracture toughness ofceramics. Engineering Fracture Mechanics, Vol. 31 (2) (1988) pp. 309-313.

101. Averback R, Hofler H, Tao R. Processing of nano-grained materials. Materials Science and Engineering, A166 (1993) pp. 169-177.

102. Schuh C, Nieh T. Hardness and Abrasion Resistance of Nanocrystalline Nickel Alloys Near the Hall-Petch Breakdown Regime. Materials Research Society, Symposium Proceeding, 740 (2003).

103. Qi Z, Sun P, Zhu F, Peng D, Wu C. The inverse Hall–Petch effect in nanocrystalline ZrN coatings. Surface and Coating Technology, Vol. 205 (2011) pp. 3692-3697.

104. Paneto F, Pereira J, Lima J, Jesus E, Silva L, E. Sousa Lima E, Cabral R, Santos C. Effect of porosity on hardness of Al_2O_3–$Y_3Al_5O_{12}$ ceramic composite. International Journal of Refractory Metals and Hard Materials. Vol. 48 (2015) pp. 365–368.

105. Balak Z, Zakeri M, Rahimipur M, Salahi E, Nasiri H. Effect of open porosity on flexural strength and hardness of ZrB_2-based composites. Ceramics International, Vol. 41 (7) (2015) pp. 8312-8319.

106. Nose T, and Fujii T. Evaluation of Fracture Toughness for Ceramic Materials by a Single-Edge-Precracked-Beam Method. Journal of the American Ceramic Society, Vol. 71 (5) (1998) pp. 328–333.

107. García-Prieto A, Baudín C. Influence of experimental variables on fracture toughness determined on SEVNB in three points bending: Mullite a case study. Journal of the European Ceramic Society, Vol. 32 (16) (2012) pp. 4241–4248.

108. ASTM C 1421-09: Standard Test Method for Fracture Toughness of Advanced Ceramics at Ambient Temperatures. Annual Book of ASTM Standards, American Society for Testing Materials, Pennsylvania (2009).

109. Kübler J. Fracture toughness of Ceramics using the SEVNB Method. Round Robin, VAMAS Report No. 37 (1999).

110. Anstis G, Chantikul P, Lawn B, Marshall D. A critical evaluation of indentation techniques for measuring fracture toughness: I Direct crack measurements. Journal of the American Ceramic Society, Vol.64 (1981) pp. 533-538.

111. Evans A, Charles E. Fracture toughness determination by indentation. Journal of the American Ceramic Society, Vol. 59 (1976) pp. 371-372.

112. Shetty D, Wright I, Mincer P and Clauer A. Indentation fracture of WC-Co cermets. Journal of Materials Science, Vol. 20 (1985) pp. 1873-1882.

113. Niihara K. A fracture mechanics analysis of indentation-induced Palmqvist crack in ceramics. Journal of Materials Science Letters, Vol. 2 (1983) pp. 221-223.

114. Lawn B, Evans A, Marshall B. Elastic/plastic indentation damage in ceramics: the median/radial crack system. Journal of the American Ceramic Society, Vol. 63 (1980) pp. 574–581.

115. Fischer H, Marx R. Fracture toughness of dental ceramics: comparison of bending and indentation method. Dental Materials, Vol. 18 (2002) pp. 12-19.

116. Quinn G, Bradt R. On the Vickers Indentation Fracture Toughness Test. Journal of the American Ceramic Society, Vol. 90 (3) (2007) pp. 673–680.

117. Smallman R, Bishop R. Modern Physical Metallurgy and Materials Engineering: Science, Process, Applications. 6th ed. Butterworth-Heinemann (1999) pp. 197-405.

118. Sadighpour L, Geramipanah F, Raeesi B. In vitro mechanical tests for modern dental ceramics. Journal of Dentistry of Tehran University of Medical Sciences, Vol. 3 (3) (2006) pp. 1-10.

119. Nygren M, Shen Z. On the preparation of bio-, nano- and structural ceramics and composites by spark plasma sintering. Solid State Sciences, Vol 5 (l) (2002) pp. 125-131.

120. Lu C, Danzer R, Fishcer D. Fracture statistics of brittle materials: Weibull or normal distribution. Physical Review E, Vol. 65 (6) (2002) pp. 067102.

121. Becker T, Cannon R, Ritchie R. Statistical fracture modeling: crack path and fracture criteria with application to homogeneous and functionally graded materials. Engineering Fracture Mechanics, Vol 69 (2002) pp. 1521–1555.

122. Wachtman B, Cannon W, and Matthewson M. Mechanical Properties of Ceramics, Second Edition. John Wiley & Sons, Inc., United States of America. (2009).

123. BS EN 843-5. Advanced technical ceramics–Mechanical properties of monolithic ceramics at room temperature. Part5: Statistical analysis. London, UK: British Standard Institute. (2006).

124. Gurland J. The Fracture Strength of Sintered Tungsten Carbide–Cobalt Alloys in Relation to Composition and Particle Spacing. Transactions of the Metallurgical Society, 227 (1963) pp. 1146–1150.

125. Morrell R, McCormick N, Bevan J, Lodeiro M, Margetson J. Biaxial disc flexure-modulus and strength testing. British Ceramic Transactions, Vol. 98 (5) (1999) pp. 234–240.

126. Börger A, Supancic P, Danzer R. The Ball on Three Balls Test for Strength Testing of Brittle Discs -Stress Distribution in the Disc. Journal of the European Ceramic Society, Vol. 22 (2002) pp. 1425-1436.

127. Börger A, Supancic P, Danzer R. The Ball on Three Balls Test for Strength Testing of Brittle Discs - Part II: Analysis of Possible Errors in the Strength Determination. Journal of the European Ceramic Society, Vol. 24 (2004) pp. 2917–2928.

128. Basu B, Kalin M. Tribology of Ceramics and Composites: A Material Science Perspective, John Wiley & Sons, Inc., New Jersey, USA (2011).

129. Bhushan B. Tribology: Friction, Wear, and Lubrication. The Engineering Handbook. Dorf C (Ed.) CRC Press LLC, Boca Raton (2000).

130. Kato K, Adachi K. Wear Mechanisms. Modern Tribology Handbook. Bhushan B (Ed.), CRC Press LLC, Boca Raton (2001).

131. Evans A, Marshall D. , Wear mechanism in ceramics. Fundamentals of Friction and Wear of Materials. Rigney D. (Ed.), ASM, 439 (1981).

132. Bhushan B. Principles and Applications of Tribology. John Wiley and Sons, New York, USA (1999).

133. Gates J. Two-Body and Three-Body abrasion: A critical discussion. Wear, Vol. 214 (1) (1998) pp. 139-146.

134. Sasada T. The role of adhesion in wear of materials, Journal of Japan Society of Lubrication Engineering, Vol. 24 (11) (1979) pp. 700-705.

135. Vingsbo O, Hogmark S. Wear of steels. Fundamentals of Friction and Wear of Materials. Rigney D. (Ed.), ASM, 373 (1980).

136. Chen L, Rigney D. Transfer during unlubricated sliding wear of selected metal systems. Wear, Vol. 105 (1985) pp. 47-61.

137. ASTM C373-88 2006 (American Society for Testing and Materials) as obtained from http://www.astm.org/Standards/C373.htm on 06-12-2011.

138. ImageJ. https://imagej.net/Welcome. As accessed 20 June 2015.

139. Harrer W, Danzer R, Morrell R. Influence of surface defects on the biaxial strength of a silicon nitride ceramic – Increase of strength by crack healing. Journal of the European Ceramic Society, Vol. 32 (2012) pp. 27–35.

140. Spiegler R, Schmauder S and Sigl L. Fracture toughness evaluation of WC-Co alloys by indentation testing. Journal of Hard Materials, Vol.1 (3) (1990) pp. 147-158.

141. Montanuniversität Leoben, Institute of Structural and Functional Ceramics. http://www.isfk.at/de/960/. As accessed 13 August 2014.

142. Jones M, Hirao K, Hyuga H, Yamauchi Y, Kanzaki S. Wear Properties of Y-αβ Composite Sialon Ceramics. Journal of the European Ceramic Society, Vol. 23 (2003) pp. 1743-1750.

143. G133-95 2002 (American Society for Testing and Materials); Standard Test Method for Linearly Reciprocating Ball-on-Flat Sliding Wear.

144. Kumar B, Kim W, Hong S, Bae H, Lim D. Effect of grain size on wear behavior in Y-TZP ceramics. Materials Science and Engineering A, Vol. 527 (2010) pp. 474–479.

145. ISO 13320-1, Particle Size Analysis, Laser Diffraction Methods, (1999).

146. Pang H, Ridgway K.Mechanism of sieving: Effect of particle size and shape. Powtech '83 Particle Technology, Event No. 280 of the EFCE (1983) pp. 163–169.

147. Zhang Z, Shen P, Jiang Q. Differential thermal analysis (DTA) on the reaction mechanism in Fe–Ti–B4C system. Journal of Alloys and Compounds, Vol. 463 (2008) pp. 498–502.

148. Laszkiewicz-Łukasik J, Jaworska L, Putyra P, Klimczyk P, Garzeł G. The influence of SPS heating rates on the synthesis reaction of tantalum diboride. Boletín de la Sociedad Española de Cerámica y Vidrio, Vol. 55 (4) (2016) pp. 159–168.

149. Rogl P. Boron–Carbon–Iron. Iron System - Part 1, Landolt-Börnstein series, Group IV: Physical Chemistry, Effenburg G. (ed.), Vol. 11D1, Springer, Berlin (2008) pp. 349-378.

150. Sigma Aldrich, Safety data sheet (iron). http://www.sigmaaldrich.com/MSDS/MSDS/DisplayMSDSPage.do?country=ZA&language=en&productNumber=44890&brand=ALDRICH&PageToGoToURL=http%3A%2F%2Fwww.sigmaaldrich.com%2Fcatalog%2Fproduct%2Faldrich%2F44890%3Flang%3Den. As accessed January 2017.

151. Springer Materials, α-Ti (Ti rt) Crystal Structure. http://materials.springer.com/isp/crystallographic/docs/sd_0308501. As accessed January 2017.

152. West D. Ternary Equilibrium Diagrams (2nd edition), Chapman and Hall, London (1982).

153. Ohtani H, Hasebe M, Ishida K, Nishizawa T. Transactions of the Iron and Steel Institute of Japan, Vol. 28(12) (1988) pp. 1043-1050.

154. Hougardy H. Transformation of Steels during cooling. Theory and Technology of Quenching, A Handbook. Lissic B, Tensi H, Luty W. (eds.), Springer Science and Business Media, New York (1992) pp. 1-18.

155. Lomovsky O, Golubkova G, Bulina N, Yadroitsev I, Smurov I. Laser-induced reactions in layers of B_4C + Fe and B + C + Fe mixtures on a steel substrate. Inorganic Materials, Vol. 49(6), (2013) pp. 564–567.

156. Terry B, Chinyamakobvu O. Assessment of B4C reaction with liquid iron alloys. Journal of Material Science, Vol. 29 (1994) pp. 464-467.

157. Munhollon T, Rafaniello W. Processing of Boron Rich Boron Carbide. Advances in Ceramic Armor XI, LaSalvia J. (ed.), The American Ceramic Society, John Wiley & Sons, Inc., New Jersey, USA (2016) pp. 99-110.

158. German R. Chapter Nine – Sintering With a Liquid Phase, Sintering: from Empirical Observations to Scientific Principles. Butterworth-Heinemann, Boston, USA (2014) pp. 247–303.

159. Zhang X, Gao H, Zhang Z, Wen R, Wang G, Mu J, Chec H, Zhang X. Effects of pressure on densification behaviour, microstructures and mechanical properties of boron carbide ceramics fabricated by hot pressing. Ceramics International, Vol. 43 (8) (2017) pp. 6345–6352. : s.n.

160. Brandis H, Haberling E, Weigard H. Metallurgical Aspects of Carbides in High Speed Steels. Processing and Properties of High Speed Tool Steels. Wells M and Lherbier L (Eds.),TMS-AIME, Pensylvania, USA (1980) pp. 1–18.

161. Chuenarrom C, Benjakul P, Daosodsai P. Effect of indentation load and time on knoop and vickers microhardness tests for enamel and dentin. Materials Research, Vol.12 (4) São Carlos (2009) pp. 473-476.

162. Herrmann M, Klemm H, Schuber C. Silicon Nitride Based Hard Materials. Handbook of ceramic hard materials, Vol. 2, Riedel R (Ed.), Wiley-VCH, Germany. (2000) pp. 749-801.

163. Cheng L, Xie Z, Liu G, Liu W, Xue W. Densification and mechanical properties of TiC by SPS-effects of holding time, sintering temperature and pressure condition. Journal of the European Ceramic Society, Vol. 32 (12) (2012) pp. 3399–3406.

164. Zhang F, Lin K, Chang J, Lu J, Ning C. Spark Plasma Sintering of Macroporous Calcium Phosphate Scaffolds from Nanocrystalline Powders. Journal of the European Ceramic Society, Vol. 28 (2008) pp. 539-545.

165. Fang Z, Koopman M, Wang H. Cemented Tungsten Carbide Hardmetal - An Introduction. Comprehensive hard materials, Vol. 1: Hardmetals, Sain V (ed.), Elsevier Ltd., Oxford, UK. (2014) pp. 123-138.

166. Martini C, Palombarini G, Poli G, Prandstraller D. Sliding and abrasive wear behaviour of boride coatings. Wear, Vol. (256) (2004) pp. 608–613.

167. Wu J, Wang B, Zhang Y, Liu R, Xia Y, Li G, Xue W. Enhanced wear and corrosion resistance of plasma electrolytic carburized layer on T8 carbon steel. Materials Chemistry and Physics, Vol. 171 (2016) pp. 50–56.

168. Aatthisugan I, Rose A, Jebadurai D. Mechanical and wear behaviour of AZ91D magnesium matrix hybrid composite reinforced with boron carbide and graphite. Journal of Magnesium and Alloys, In Press, doi: 10.1016/j.jma.2016.12.004 (2017) pp. 1-6.

169. Kato K. Wear in relation to friction — a review. Wear, Vol. 241 (2000) pp. 151–157.

170. Candelario V, Borrero-López O, Guiberteau F, Moreno R, Ortiz A. Sliding-wear resistance of liquid-phase-sintered SiC containing graphite nanodispersoids. Journal of the European Ceramic Society, Vol. 34 (10) (2014) pp. 2597–2602.

171. Fischer T, Anderson M, Jahanmir S. Influence of fracture toughness on the wear resistance of yttria-doped zirconium oxide. Journal of the American Ceramic Society, Vol. 72 (2) (1989) pp. 252-257.

172. Turatti A, Pereira A. Wear resistant boron carbide compacts produced by pressureless sintering Ceramics International, Article in press, http://dx.doi.org/10.1016/j.ceramint.2017.03.064, (2017) pp. 1-8.

173. Shipway P, Hogg J. Wear of bulk ceramics in micro-scale abrasion—The role of abrasive shape and hardness and its relevance to testing of ceramic coatings. Wear, Vol. 263 (2007) pp. 887–895.